Blow-off in Gas Turbine Combustors

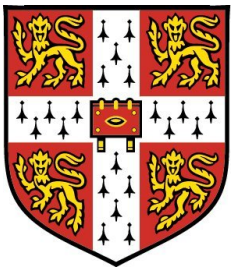

Davide Egidio Cavaliere

Hughes Hall

University of Cambridge

A thesis submitted for the degree of

Doctor of Philosophy

June 2013

To my grandmothers
Anna and Maria.

There are no favourable winds for the sailor
who doesn't know where to go.
Seneca

Acknowledgements

I would like to give my thanks to my supervisor **Prof. Epaminondas Mastorakos**. I am extremely grateful for his continuous support and guidance. He has always had a M.A.P. for my PhD. **M**otivation to share every day, **A**dvice to discover something new and **P**atience throughout my learning process.

I would also like to thank my advisor Dr. James Dawson for his valuable suggestions and help, particularly regarding the laser diagnostics. I want to acknowledge the financial assistance of the Rolls-Royce Group and the European Commission through project TECC-AE (ACP7-GA-2008-211843). I want to thank my friend and colleague Dr. James Kariuki for his great help and for our interesting chats, I learned so much with and from him. Special thanks also go to Dr. Camille Letty for her much appreciated contributions and valuable input relating to the spray measurements and Jenni Sidey for her help during the emissions measurements. I am grateful to Dave Farrow for the spectra analysis code.

I am indebted to my colleagues from the Hopkinson Laboratory: Alex, Andrea Pastore, Cheng, Giulio, Andrea Maffioli, Michael, Artur, Thibault, Rob, Teresa, Jenni, Frank, Simon, Ivan. Their help and our breaks together contributed to an amazing time in the department. I would like to express my gratitude to the gentlemen of the workshop: Michael Underwood, Ken Griggs, Robert Leroy and John Harvey. Without them this thesis could not exist. I also wish to thank Mr. Peter Benie for his help with the computing facilities, and Mrs. Kate Graham for her assistance and useful suggestions.

I am grateful to Prof. Andrea D'Anna and Dr. Teresa Marchione who encouraged me to embrace the challenges of a PhD, and who have always been very supportive of my work. My sincere thanks go to my college, Hughes Hall, for providing a stimulating and friendly environment where I could meet wonderful friends such as Stefano Salvatore, Katie, Lara, Nuno, Marek, Alex, Richard and Stefano Gogioso.

The 42,000 words of this thesis are not enough to express my gratitude to my parents Prof. Antonio Cavaliere and Dr. Anna Ciajolo, my brother Iosepho and my sister Marilou who support and inspire me every single day.

Last, but certainly not least, I thank **Chiara**, for her love, her patience, her advice and invaluable support during this long and marvellous journey. She is the flame inside me that can never blow-off.

Publications and Conferences

In chronological order, the work that is the subject of this thesis and results from the experiments have been presented, awarded and have appeared for publication in:

- A. Tyliszczak, D.E. Cavaliere, E. Mastorakos, (2013), *LES/CMC of blow-off in a liquid fueled swirl burner*, Flow Turbulence and Combustion, ISSN 1386-6184.
- D.E. Cavaliere, J. Kariuki, E. Mastorakos, (2013), *A comparison of the blow-off behaviour of swirl-stablized premixed, non-premixed and spray flames*, Flow Turbulence and Combustion, 91, pp. 347-372..
- J. Kariuki, D.E. Cavaliere, C. Letty, E. Mastorakos, (2012), *A comparison of the blow-off behaviour of swirl-stabilized premixed and spray flames*, 50^{th} AIAA Aerospace Sciences Meeting, AIAA paper no. 2012-505.
- D.E. Cavaliere, J. Kariuki, E. Mastorakos, *Blow-off in gas turbine combustors*, 10^{th} Osborne Reynolds Colloquium and Research Student Award by ERCOFTAC, Finalist, Southampton University, U.K., 2012.
- D.E. Cavaliere, J. Kariuki, C. Letty, E. Mastorakos, *Blow-off of turbulent swirling spray flames*, Awarded in the poster session, Fluid mechanics- Energy and Turbomachinery Expo, Cambridge, U.K., 2011.
- D.E. Cavaliere, C. Letty, E. Mastorakos, *Blow-off of turbulent swirling spray flames*, Poster, 7^{th} Mediterranean Combustion Symposium, Italy, 2011.

- D.E. Cavaliere, J. Kariuki, E. Mastorakos, *Visualization of a blow-off event*, Awarded to the 3^{rd} place at Carl Zeiss Video Engineering Competition, University of Cambridge, U.K., 2011.

Webpage link for videos

http://www.dspace.cam.ac.uk/handle/1810/243895

Declaration

This dissertation is submitted to the University of Cambridge in fulfillment for the degree of Doctor of Philosophy. It is an account of the research I have undertaken in the Department of Engineering at the University of Cambridge, under the supervision of Prof. E. Mastorakos. The work described is original and a result of my own work and includes nothing which is the outcome of work done in collaboration except where specifically indicated in the text. This dissertation contains approximately 42,000 words, 85 figures and 7 tables, and no part of it has already been, or is currently being, submitted for any other degree, diploma, or other qualification, at any other University.

Hopkinson Laboratory, Cambridge
10^{th} June 2013
Davide Egidio Cavaliere

Abstract

This thesis describes an experimental investigation of the flame structure close to the extinction and the blow-off events of non-premixed and spray flames stabilized on an axisymmetric bluff body in a confined swirl configuration. The comparison of flames of different canonical types in the same basic aerodynamic field allows insights on the relative blow-off behaviour.

The first part of the thesis describes several velocity measurements in non-reacting and reacting flows. The main usefulness of this data is to provide the aerodynamic flow pattern and some discussion on the velocity field and the related recirculation zones. The velocity and turbulence information obtained are particularly useful for providing data, which is crucial for validation of computational models.

The second part describes an experimental investigation of non-premixed stable flames very close to the blow-off condition. The measurements included visualisation of the blow-off transient with 5 kHz OH* chemiluminescence, which allowed a quantification of the average duration of the blow-off transient. OH-PLIF images at 5 kHz for flames far from and close to extinction showed that the non-premixed flame intermittently lifts-off the bluff body, with increasing probability as the fuel velocity increases. The flame sheet shows evidence of localised extinctions, which are more pronounced as approaching blow-off. The measurements include blow-off limits and their attempted correlation. It was found that a correlation based on a Damköhler number does a reasonable job at collapsing the dataset.

The final part examines the blow-off behaviour of swirling spray flames for two different fuels: n-heptane and n-decane. The measurements

include blow-off limits and their attempted correlation, visualisation of the blow-off transient with 5 kHz OH* chemiluminescence, and the quantification of the average duration of the blow-off transient. It was found that the average duration of the blow-off event is in order of the tens of ms for both spray flames (10-16 ms). The blow-off event is therefore a relatively slow process for the spray flames using n-heptane and decane fuels. This suggests that control measures, such as fast fuel injection, coupled with appropriate detection, such as with chemiluminescence monitoring, may have a reasonable chance of success in keeping the flame alight very close to the blow-off limit.

These results, together with those obtained for the non-premixed gaseous case form a wide body of experimental data available for the validation of turbulent flame models. The quantification of some properties during the blow-off transient can assist studies of extinction based on large-eddy simulation that have a promise of capturing combustion transients.

Contents

Publications and Conferences iv

Contents ix

List of Figures xii

1 Introduction 1

1.1 Motivation . . . 1
1.2 Blow-off Background . . . 6
1.2.1 Turbulent premixed flames . . . 6
1.2.2 Turbulent non-premixed flames . . . 10
1.2.3 Turbulent spray flames . . . 15
1.3 Scope of the thesis . . . 27
1.4 Structure of the thesis . . . 28
1.5 Figures for Chapter 1 . . . 29

2 Experimental methods 33

2.1 Burners . . . 33
2.1.1 Non-premixed flame apparatus . . . 34
2.1.2 Spray flame apparatus . . . 35
2.2 Flow measurement methodology . . . 36
2.2.1 Flow-rate measurements . . . 36
2.2.2 Determination of the blow-off point . . . 37
2.2.3 Laser Doppler Velocimetry . . . 38
2.3 Chemiluminescence measurements . . . 40

2.4 Planar Laser Induced Fluorescence measurements 42
2.5 Mie scattering 45
2.6 Direct photography 45
2.7 Pollutants measurements 45
2.8 Duration of the blow-off event 47
2.9 Figures for chapter 2 48

3 Velocity Field **58**
3.1 Isothermal conditions 58
3.1.1 Mean and RMS velocity 59
3.1.2 Probability density functions 62
3.2 Reacting cases 63
3.2.1 Non-premixed gaseous flames 63
3.2.2 Spray flames 66
3.3 Conclusions 72
3.4 Figures for chapter 3 75

4 Non-premixed flame blow-off **99**
4.1 Introduction 99
4.2 Motivation 99
4.3 Experiment methodology 100
4.4 Data analysis 100
4.5 Results and Discussion 101
4.5.1 Stability limits 101
4.5.2 Flame shape 101
4.5.3 Flame behaviour approaching blow-off 102
4.5.4 Lift-off height statistics 103
4.5.5 Blow-off transient and its duration 104
4.5.6 Blow-off correlation 106
4.5.7 Emission measurements 107
4.6 Conclusions 109
4.7 Figures for chapter 4 111

5 Spray flame blow-off **124**
5.1 Introduction . . . 124
5.2 Motivation . . . 124
5.3 Methodology . . . 125
5.4 Results and Discussion for n-heptane flames . . . 126
5.4.1 Stability limits . . . 126
5.4.2 Flame shape . . . 126
5.4.3 Flame behaviour approaching blow-off . . . 127
5.4.4 Lift-off height statistics . . . 128
5.4.5 Blow-off transient and its duration . . . 129
5.4.6 Blow-off correlation . . . 130
5.4.7 Emission measurements . . . 135
5.5 Results and Discussion for n-decane flames . . . 136
5.5.1 Stability limits . . . 137
5.5.2 Flame shape . . . 137
5.5.3 Blow-off transient and its duration . . . 137
5.5.4 Blow-off correlation . . . 139
5.6 Conclusions . . . 139
5.7 Figures for chapter 5 . . . 141

6 Conclusions and suggestions for further research **164**
6.1 Conclusions from this work . . . 165
6.1.1 Velocity fields . . . 165
6.1.2 Non-premixed flames . . . 166
6.1.3 Spray flames . . . 166
6.2 Suggestions for further research . . . 167

References **169**

List of Figures

1.1 Combustion stability limits [19]. 29
1.2 Schematic of the formation of a recirculation zone by swirl [103]. . 29
1.3 Schematic of (a) the pressure swirl atomizer, (b) the air-assist atomizer and (c) the air blast atomizer. Figure adapted from [60]. . 30
1.4 Schematic of the temperature profile across a laminar freely propagating premixed spray flame with a large Sauter Mean Diameter. The post evaporation zone exists in a rich case only [97]. 30
1.5 (a) Characteristic time correlation (negligible fuel-penetration effects); (b) Complete characteristic time correlation [86]. 31
1.6 Burner schematic illustrating the effect of fuel penetration on flame structure, on the top when the penetration effects is negligible and below when the penetration effects is not negligible [86]. 32

2.1 Schematic of the non-premixed configuration. All dimensions in mm. 48
2.2 Image showing (a) a photograph of the combustor, (b) a photograph of the quartz enclosure and (c) a photograph of the bluff body without the swirler. All dimensions in mm. 49
2.3 Image showing (a) photograph of the bluff body and the swirler (b) photograph from the top of the swirler and (c) a photograph of the swirler from a side view. 49
2.4 Experimental set up of the non-premixed configuration. 50

2.5 Image showing (a) a photograph of the pressure swirl atomizer used in the present work, (b) sketch of the pressure swirl atomizer with helical inlets provided by a conical insert and (c) sketch of the pressure swirl atomizer and the spray associated. Images (b) and (c) are from Lechler Company Nozzle Catalogue [1]. 51
2.6 Experimental set up of the spray configuration. 52
2.7 (a) Schematic of the spray burner and (b) detail of the bluff body. All dimensions in mm. 53
2.8 Schematic of the laser layout used for LDA measurements of the non-reacting case. 54
2.9 Photograph of the LDA setup. 55
2.10 Photograph of the four beams and the collecting probe of the 2D-LDA setup during a spray reacting case measurement. 55
2.11 Schematic of the laser layout used for OH-PLIF imaging. 56
2.12 Schematic of the setup for emissions measurements. 56
2.13 A photograph (a) and a dimensioned sketch (b) of the sampling probe used to collect the emissions. 57

3.1 Mean axial velocity profiles normalized with the bulk velocity for flow condition CSWH1 (a-b) and condition CSWH3 (c-d). 75
3.2 R.m.s of the axial velocity at flow condition CSWH1 (a-b) and at condition CSWH3 (c-d). 76
3.3 Mean radial velocity profiles for condition (a) CSWH1 and (b) CSWH3. R.m.s radial profiles for the condition (c) CSWH1 and (d) CSWH3. 77
3.4 Mean swirl velocity profiles for condition (a) CSWH1 and (b) CSWH3. R.m.s swirl profiles for condition (c) CSWH1 and (d) CSWH3. 78
3.5 Comparison of (a) the mean axial velocity profiles, (b) the mean radial velocity profiles and the (c) the mean swirl velocity profiles for two flow conditions: CSWH1 and CSWH3. 79

3.6 Schematic of the flow pattern and the recirculation zones. The stars denote the locations where the spectra of the instantaneous velocity have been determined. 80
3.7 Radial distribution of the typical characteristic turbulent velocity q and q' at the condition CSWH1 (a) and at the condition CSWH3 (b). 81
3.8 Radial distribution of the typical characteristic turbulent velocity, q, at CSWH1 (a) and CSWH3 (b) for three axial stations. 82
3.9 Probability density functions of the axial velocity at different radial position at z=8mm for CSWH1 flow condition (a, c, e) and CSWH3 condition (b, d, f). 83
3.10 Probability density functions of the axial velocity at different radial position at z=33mm for CSWH1 flow condition (a, c, e) and CSWH3 condition (b, d, f). 84
3.11 Probability density functions of the radial velocity at different radial position at z=8mm for CSWH1 flow condition (a, c, e) and CSWH3 condition (b, d, f). 85
3.12 Probability density functions of the swirl velocity at different radial position at z=8 mm for CSWH1 flow condition (a, c, e) and CSWH3 condition (b, d, f). 86
3.13 Probability density functions of the swirl velocity at different radial position at z=33mm for CSWH1 flow condition (a, c, e) and CSWH3 condition (b, d, f). 87
3.14 Probability density functions of the axial velocity at different radial position at z=8 mm (a-d) and 33 mm (e-h). CSWH1 flow condition. 88
3.15 Probability density functions of the axial velocity at different radial position at z=8 mm (a-d) and 33 mm (e-h). CSWH3 flow condition. 89
3.16 Mean axial velocity profiles (a), mean swirl velocity profiles (b), r.m.s of the axial velocity (c), r.m.s. of the swirl velocity (d). All profiles are normalized with the bulk velocity (U_b). The flow condition is F3A2 (non-premixed gaseous reacting case). 90

3.17 Profiles of Power Spectral Density of the axial velocity (upper) and swirl velocity (lower) for a downstream location z=15 mm and r/d=0. The dashed straight line represents the equation $y = x^{-5/3}$. The flow condition is F3A2 (non-premixed gaseous reacting case). 91
3.18 Profiles of Power Spectral Density of the axial velocity (upper) and swirl velocity (lower) for a downstream location z=15 mm and r/d=0.72. The dashed straight line represents the equation $y = x^{-5/3}$. The flow condition is F3A2 (non-premixed gaseous reacting case). 92
3.19 Profiles of Power Spectral Density of the axial velocity (upper) and swirl velocity (lower) for a downstream location z=110 mm and r/d=0. The dashed straight line represents the equation $y = x^{-5/3}$. The flow condition is F3A2 (non-premixed gaseous reacting case). 93
3.20 Mean axial velocity of the droplets (a), mean swirl velocity of the droplets (b), r.m.s of the axial droplet velocity (c), r.m.s. of the swirl droplet velocity (d). All profiles are normalized with the bulk velocity (U_b) and the radius by d. The flow condition is SWH1. . 94
3.21 Mean axial velocity profiles (a), mean swirl velocity profiles (b), r.m.s of the axial velocity (c), r.m.s. of the swirl velocity (d). All profiles are normalized with the bulk velocity (U_b). The flow condition is SWH1 (spray reacting case). 95
3.22 Mean axial velocity profiles of the droplets only and of the air with the seeding at z=10 mm (a), mean swirl velocity profiles of the droplets only and of the air with the seeding at z=10 mm. All profiles are normalized with the bulk velocity (U_b). The flow condition is SWH1 (spray reacting case). 96
3.23 Profiles of Power Spectral Density of the axial velocity (upper) and swirl velocity (lower) for a downstream location z=10 mm and r/d=0.8. The flow condition is SWH1 (spray reacting case). . 97
3.24 Profiles of Power Spectral Density of the axial velocity (upper) and swirl velocity (lower) for a downstream location z=20 mm and r/d=1.12. The flow condition is SWH1 (spray reacting case). 98

4.1 Air velocity at blow-off as a function of the fuel jet velocity for the non-premixed flame. The stars denote the stable flow conditions F3A1 and F3A2. The circle denotes the blow-off conditions and F3A3_E is also indicated. 111
4.2 (a, c) Photographs of non-premixed flames F3A1 and F3A2. Corresponding Abel-transformed time-averaged OH* chemiluminescence images (b, d). 112
4.3 Images of the normalized mean (top row) and RMS (bottom row) of OH-PLIF for flames F3A1 (a, b) and F3A2 (c, d). 113
4.4 Sequence of instantaneous OH-PLIF images (corrected for laser sheet inhomogeneities) showing the temporal evolution of the flame at conditions far from blow-off, F3A1. Image size 50 × 95 mm. Colour scale varies from blue to red with increasing OH concentration. 114
4.5 Independent OH-PLIF snapshots for non-premixed flames (image size 50 × 95 mm); from top to bottom: F3A1, F3A1, F3A2. The three instantaneous images are separated by a time delay. 115
4.6 Upper: Air velocity at blow-off as a function of the fuel jet velocity for the non-premixed flame. The stars denote flames far from blow-off. The number denotes the mean lift-off height in mm. Lower: Probability density function of the lift-off height for the flow conditions: F3A1 (square), F3A2 (circle). The numbers indicated show the average lift-off height in mm. 116
4.7 Spectra of OH obtained from the OH-PLIF timeseries for flames F3A1 (a) and F3A2 (b).The spectra were calculated at a distance of 2 mm from the bluff body along the shear layer in the right (r/d=1.45) and left part(r/d=-1.45) of the combustor. 117
4.8 OH* chemiluminescence sequence of two independent blow-off events for the non-premixed flame $F3A3\_E$. Side view, flow comes from below, axis of the burner at the centre of the x range. Image size 90 × 90 mm.The sequence on the top has an extinction time of 29 ms. The sequence on the bottom has an extinction time of 71 ms. 118

4.9 Sequence of instantaneous OH-PLIF images (corrected for laser sheet inhomogeneities) showing the temporal evolution of the structure of the flame during a blow-off event, $F3A3\_E$. Image size 50×95 mm. Colour scale varies from blue to red with increasing OH emission. 119
4.10 Average of area-integrated OH* time series (thick line), and area-integrated OH* from ten individual blow-off events (thin lines), each shifted to match the instant of extinction and normalized by its pre-extinction value. The definition of the average duration of the blow-off event, τ_{ext}, is indicated. 119
4.11 Evaluation of 1/Da $\left(\left[\left(\frac{U_b}{d}\right)\left(\frac{\nu}{S_L^2}\right)\right]^{1/2}\right)$ based on the extinction correlation proposed by Radhakrishnan et al. [89], as a function of the fuel velocity. 120
4.12 Dry NO_x mole fraction (a) and dry CO mole fraction (b) for F3A1 and F3A2 flow condition at 140 mm from the bluff-body. 121
4.13 Dry O_2 mole fraction (a) and dry CO_2 mole fraction (b) for F3A1 and F3A2 flow condition at 140 mm from the bluff-body. The values are corrected to a 15 % level of O_2 in the dry product stream. 122
4.14 Wet UHC mole fraction for F3A1 and F3A2 flow condition at 140 mm from the bluff-body. 123

5.1 Air velocity at blow-off as a function of the fuel flow rate for the spray heptane flame. The triangles denote the stable flow conditions SWH0, SWH1, SWH2 and the blow-off condition SWH3. . . 141
5.2 Photographs of heptane spray flames: (a) SWH0 (b) SWH1, (c) SWH2. Exposure time: 30 ms. 142
5.3 Abel-transformed time-averaged OH* chemiluminescence images for heptane spray flames at different stable flow conditions: (a) SWH0, (b) SWH1, (c) SWH2. 143

5.4 Time-averaged images over 5000 frames (equivalent to a data acquisition time of 1 s). First row: average images. Second row: RMS. Flow conditions SWH0 (a-b), SWH1 (c-d) and SWH2 (e-f). Side view, flow comes from below, axis of the burner at the centre of the x range. 144
5.5 Time-averaged images over 5000 frames of heptane spray Mie scattering (top row) and OH-PLIF images superimposed on the same Mie scattering images (bottom row) of spray flames: (a, c) SWH1 and (b, d) SWH2. 145
5.6 Time-averaged images over 5000 frames of spray Mie scattering at stable flow conditions: (a) SWH0, (b) SWH1, (c) SWH2. First row: average images. Second row: RMS. 146
5.7 Sequence of instantaneous OH-PLIF images showing the temporal evolution of the structure of the flame at stable conditions: (a) SWH0, (b) SWH1, (c) SWH2. 147
5.8 Independent OH-PLIF snapshots for spray heptane flames (image size 30×95 mm); from top to bottom: SWH1, SWH1, SWH2. The three instantaneous images are separated by a time delay. 148
5.9 Upper: Air velocity at blow-off as a function of the fuel flow rate. Same data as Fig. 5.1, replotted here for clarity. The stars denote flames far from blow-off. The number denotes the mean lift-off height in mm. The first number denotes the mean lift-off height in mm and the second the percentage of time the flame is lifted. Lower: Probability density function of the lift-off height, SWH1 (square) and SWH2 (circle). The numbers indicated show the average lift-off height in mm. 149
5.10 OH* chemiluminescence sequence of a blow-off event for a spray flame at condition SWH3. Side view, flow comes from below, axis of the burner at the centre of the x range. Image size 90 mm $\times$ 90 mm. 150
5.11 OH* chemiluminescence sequence of a blow-off event for a spray flame at SWH3 condition. Top view, burner axis at the centre of the image. Image size 90 mm $\times$ 90 mm. 151

5.12 OH-PLIF sequence of a blow-off event for a spray flame at SWH3 condition.Burner axis at the centre of the image. Image size 50 mm × 95 mm. 152
5.13 Average of area-integrated OH* time series (thick line), and area-integrated OH* from individual blow-off events (thin lines), each shifted to match the instant of extinction and normalized by its pre-extinction value. The definition of the duration of the blow-off event, τ_{ext}, is indicated. 152
5.14 Comparison of measured and predicted values of extinction limits with different correlations. (a) Equation 5.1. (b) Equation 5.2. (c) Equation 5.3. 153
5.15 Comparison of measured and predicted values of extinction limits with equation 5.2 and three different D_{32}. Triangles represent the values calculated with D_{32}= 20 μm, circles with D_{32}= 40 μm, stars with D_{32}= 80 μm. 154
5.16 Complete characteristic time correlation for blow-off limit based on the correlation of Plee and Mellor [86], Eq. (5.6). 154
5.17 Evaluation of 1/Da $\left(\left[\left(\frac{U_b}{d}\right)\left(\frac{\nu}{S_L^2}\right)\right]^{1/2}\right)$ based on the extinction correlation proposed by Radhakrishnan et al. [89], as a function of the fuel flow rate, for the heptane spray flames. 155
5.18 Evaluation of Da $\left(\left[\left(\frac{U_b}{d}\right)\left(\frac{\nu}{S_L^2}\right)\right]^{1/2}\right)$ based on the extinction correlation proposed by Radhakrishnan et al. [89], as a function of the fuel air ratio for different combustion regimes. The premixed data are from Kariuki et al. [52]. 156
5.19 Dry O_2 mole fraction (a) and dry CO_2 mole fraction (b) for SWH1 and SWH2 flow condition. The values are corrected to a 15 % level of O_2 in the dry product stream. 157
5.20 Dry NO_x mole fraction (a) and dry CO mole fraction (b) for SWH1 and SWH2 flow condition. 158
5.21 Wet UHC emissions for SWH1 and SWH2 flow condition. 159
5.22 Air velocity at blow-off as a function of the fuel flow rate for the spray decane flame. 159

5.23 Photograph of the decane spray flames. Flow condition SWD1. Exposure time: 30 ms. 160
5.24 Time-averaged OH-PLIF images over 3000 frames for the spray decane flame. Flow condition SWD1. Side view, flow comes from below, axis of the burner at the centre of the x range. 160
5.25 OH* chemiluminescence sequence of a blow-off event for a spray decane flame at SWD3 condition. Front view, burner axis at the centre of the image. Image size 90 mm × 90 mm. 161
5.26 OH-PLIF sequence of a blow-off event for a spray decane flame at SWD3 condition. Burner axis at the centre of the image. Image size 50 mm × 95 mm. 161
5.27 Average of area-integrated OH* time series (thick line), and area-integrated OH* from individual blow-off events (thin lines) for decane spray flames, each shifted to match the instant of extinction and normalized by its pre-extinction value. The definition of the duration of the blow-off event, τ_{ext}, is indicated. 162
5.28 Evaluation of 1/Da $\left(\left[\left(\frac{U_b}{d}\right)\left(\frac{\nu}{S_L^2}\right)\right]^{1/2}\right)$ based on the extinction correlation proposed by Radhakrishnan et al. [89], as a function of the fuel flow rate for the decane spray flame. 163

Nomenclature

Roman letters

A	area, $[m^2]$
B	fuel mass transfer number
B_g	blockage ratio
c	progress variable
d	diameter of the bluff body, [m]
Da	Damköhler number
D_{hub}	swirler hub diameter, [m]
D_{sw}	swirler diameter, [m]
h	lift-off height, [m]
L_t	integral lengthscale, [m]
P	pressure, [atm]
Q	flow rate, [L/min]
Re	Reynolds number
r	radial coordinate, [m]
S_L	laminar flame speed, [m/s]
S_N	swirl number
T	temperature, [K]
T_{ad}	adiabatic flame temperature, [K]
T_{inlet}	inlet temperature, [K]
U	mean axial velocity, [m/s]
U'	root mean square of the axial velocity, [m/s]
U_b	bulk velocity, [m/s]
U_{BO}	blow-off velocity, [m/s]
V	mean radial velocity, [m/s]
V'	root mean square of the radial velocity, [m/s]

V_c	volume of the combustor, [m^3]
V_{pz}	volume of the combustion primary zone, [m^3]
W	mean swirl velocity, [m/s]
W'	root mean square of the swirl velocity

Greek letters

χ	scalar dissipation rate, [1/s]
μ	dynamic viscosity, [kg/m/s]
ν	kinematic viscosity, [m^2/s]
ρ	density, [kg/m^3]
τ	characteristic time, [s]
τ_{eb}	evaporation time, [s]
τ_{ext}	extinction time, [s]
τ_{hc}	ignition delay time, [s]
τ_{fi}	atomization time, [s]
τ_{sl}	mixing time, [s]
ϕ	equivalence ratio
ϕ_{BO}	overall equivalence ratio at blow-off
ξ	mixture fraction
ξ_{st}	stoichiometric mixture fraction

Other symbols

CFD	Computational Fluid Dynamics
CMC	Conditional Moment Closure
CRZ	Central Recirculation Zone
LCV	Lower Calorific Value, [MJ/kg]
LDA	Laser Doppler Anemometry
LES	Large Eddy Simulation
MFC	Mass Flow Controller
$PLIF$	Planar Laser Induced Fluorescence
$RANS$	Reynolds-Averaged Navier-Stokes
SMD	Sauter Mean Diameter
SRZ	Side Recirculation Zone

Chapter 1

Introduction

1.1 Motivation

Combustion since its discovery has kept a main role in the human life. Myths and stories were inspired from this powerful phenomenon. *"If they only had fire"*, said Prometheus to himself, *"they could at least warm themselves and cook their food; and after a while they could learn to make tools and build themselves houses. Without fire, they are worse off than the beasts"* [11].

The topic of this thesis is the quantification of the conditions under which combustion proceeds stably and the investigation of the extinction event of turbulent flames. In combustion processes fuel and oxidizer are mixed and burned. To achieve this, different methods can be followed. Either mixing occurs first and then burning (premixed combustion) or mixing and burning occur at the same time (non-premixed combustion). In the latter combustion mode oxidizer and fuel are injected through different streams and the flame front will be located along the stoichiometric mixture fraction. Both processes can further be subdivided in laminar or turbulent flow conditions. For most industrial applications turbulent combustion is applied. Turbulent premixed flame examples are spark ignited internal combustion and stationary gas turbine engines while turbulent non-premixed combustion can be found in diesel and jet engines. When the fuel is in liquid form, it is delivered in the form of a spray and spray flames can have characteristics of both premixed and non-premixed combustion.

One of the most undesirable sides of combustion is the formation of pollutants, including nitrogen oxides (NO_x), carbon monoxide and dioxide (CO and CO_2), and unburned hydrocarbons (UHC). The specific demand for lean combustion (very low fuel/oxidizer ratio) is due to the need to reduce emissions, in particular NO_x. In fact operating lean, the combustion temperatures at which substantial NO formation occurs can be avoided. Thus, the challenges to push the combustion to very lean conditions are associated with achieving low emissions while maintainng stability and avoiding local extinctions and the complete loss of the flame [33]. Currently, lean combustion is considered as a promising strategy to achieve the ambitious pollutants emission reduction targets set by Europe (ACARE). The targets consist of reducing 80% of NO_x emissions and 50% of CO_2 emissions by 2020 without enhancing CO and soot emissions compared to the values for the year 2000 [22].

One of the most important applications of the research related to turbulent combustion is a type of internal combustion engine, the gas turbine. A gas turbine transforms thermal energy to mechanical energy. It is essentially composed by a compressor, a combustion chamber and an axial turbine. The combustor is the source of heat addition to drive the turbine and so allowing work to be performed. Following the compression, which may take place in a different number of stages depending upon the desired pressure ratio, the air enters the combustor, where the fuel is injected and the chemical energy contained in the fuel is converted to thermal energy which is then extracted from the gases in the turbine section [33]. Gas turbines have mainly two applications: power production and aircraft propulsion where the exaust is sent through a nozzle which produces thrust. In power generation, in the past decade, 30-120 GW worth of gas turbines have been ordered each year worldwide [33]. Alternative and renewable technologies compete with gas turbines in certain size classes, but at power generation levels above 5 MW, gas turbines still offer the most attractive option due to their relatively low cost, operating, and maintenance cost [33].

A gas turbine combustor for power production, which is designed for low NO_x emissions, demands very tight control of the fuel/air ratio over the entire load range. Operating near the lean flammability limit, the point at which the fuel/air ratio is too lean to support combustion, has the risk that undesired phenomena

can occur. One of these is the main focus of this thesis: the **blow-off**. The complete loss of the flame is a **blow-off** event. Potential sources of blow-off are [27]:

- Combustor tuned to a fuel/air ratio that is out of the flammability limits.
- Instumentation failure or shift in calibration.
- Continuous emissions monitoring system out of calibration.

For aircraft propulsion, the gas turbine represents the principal source of thrust for military and commercial applications. Aviation engines require great care relatively to safety, so emissions issues are secondary. Nonetheless, emissions reduction has been pursued due to increasing concerns for air quality in the last two decades [33]. The challenges associated with combustion in an aircraft engine very close to the blow-off are illustrated in Fig. 1.1 in the context of a typical combustor stability loop. For a given pressure and temperature, the fuel/air ratio can be increased or decreased to a point where the combustor can no longer sustain the reaction. Limits in fuel/air ratio can be found on both rich and lean sides. In the present study the attention is on the lean side. An extinction in a gas turbine combustor for aircraft propulsion is most likely to occur in flight during a glide or dive with the engine idling, when there is a high air flow and only a low fuel flow, i.e. very weak mixture strength [19].

The stabilisation of a flame at high velocity is based on ensuring that at least some part of the flame is stably anchored to the burner. Several methods are employed to hold and stabilize flames [104]:

- Low-velocity bypass ports;
- Refractory burner tiles;
- Bluff body flame holders;
- Swirl or jet-induced recirculating flows.

This study mainly examines the flame stabilization schemes in applications primarily involving bluff body and swirl stabilization, so creating a recirculation

zone (RZ) where recirculating hot burned gases act as a source of continous ignition of unburned reactants [38].

Swirl is the predominant flow mechanism occurring in premixed and non-premixed combustion systems because it provides an effective means to control flame stability as well as the combustion intensity [41]. The addition of swirl has the effect of improving the flame stabilization by increasing the residence time, as observed by De Zilwa et al. [30]. Another benefit of using swirling flows for flame stabilization is the generation of a compact flame with higher level of mass recirculation than in a non-swirling configuration. The mechanism by which swirling flow creates a RZ is reported in Fig. 1.2. The tangential (swirl) velocity profile produces a radial pressure gradient that results in a sub-ambient pressure near the centreline. When there is a change in the cross-sectional area, such as when the flow enters the combustion chamber, the flow expansion results in a decrease of the radial pressure gradient, leading to an increase in the pressure along the centreline as we go downstream. This causes flow reversal and hence recirculation. The confinement can alter this process as it affects the decay of the tangential velocity and hence the fluid mechanical field in burners is affected by the chamber in which they are placed [65; 103]. All practical systems utilize high swirl in which the swirling motion is sufficiently intense to generate a large and stable central internal recirculation zone (RZ) that is also known as the toroidal vortex core.

The length and width of the RZ depends on different parameteres such as the Reynolds number (Re), the bluff body shape, the presence or not of an enclosure and the degree of swirl. An expression for evaluating the degree of swirl is the swirl number (S_N) derived by Beer and Chigier [14]. For an annular swirler with constant vane angle θ :

$$S_N = \frac{2}{3}\frac{1-(D_{hub}/D_{sw})^3}{1-(D_{hub}/D_{sw})^2}\tan\theta \tag{1.1}$$

where D_{hub} and D_{sw} represent the swirler hub diameter and the swirler diameter respectively. For $S_N > 0.6$, a swirl induced central recirculation zone is generally formed [3]. Beer and Chigier [14] use the swirl number to divide swirl flows into flows with weak and strong swirl. Weak swirl flows have a swirl number less than

0.4 and strong swirl flows with swirl number greater than 0.4 generate a central recirculation zone. Most of swirlers of practical interest operate under conditions of strong swirl (S_N>0.6), and this is the condition studied in this work.

In non-premixed combustion, changing the amount and nature of fuel injected allows to control the temperature and the gas composition into the reverse flow zone while variations of the swirl number allows an aerodynamic control for mixing and reaction [41].

The bluff-body stabilizes the flame with complex recirculation zones and it provides a controlled medium where the interaction between chemistry and turbulence may be investigated. The addition of a swirler has the effect of strengthening the recirculation region behind it and, as observed by De Zilwa et al. [30], improving the flame stabilization.

The ratio between the residence time scale, τ_{res} and a chemical time, τ_{chem}, is an important non-dimensional number to describe reacting flows and is called Damköhler number:

$$Da = \frac{\tau_{res}}{\tau_{chem}} \tag{1.2}$$

where $\tau_{res} = L/U$ with U and L corresponding to turbulence scales, e.g. the characteristic magnitude of the velocity and its lengthscale. In a swirl flow, the mean residence time is an indicator of how fast the heat and mass of the recirculation zone are transferred to the shear layer; it was found to be inversely proportional to the flow velocity [32].

Recently, the mechanism of flame blow-off (complete extinction) is receiving a great deal of attention due to the requirement to operate combustion systems under very fuel lean conditions and, therefore, close to their extinction limits. With the advent of fast diagnostics and the development of LES methods that can model transients, the unsteady features of flames have become a focal point from both an experimental and computational point of view.

These general comments may be thought to apply for all flame types stabilized by swirl (e.g. fully premixed, non-premixed, spray). As the following review will demonstrate, our present state of knowledge of blow-off has reached different levels of maturity for the various flames. The present work in particu-

lar aims to investigate and to compare the blow-off behaviour in non-premixed gaseous flames and spray flames, analyzing the behavior of extinction events, the combustion efficiency and the pollutant emissions characteristics of practical combustion devices.

1.2 Blow-off Background

In literature the term blow-out refers to extinguished flame from lifted-starting conditions, while the blow-off term refers to extinguished flame from attached-starting conditions [67]. In the present work, the term blow-off will be used, defining it as the complete extinction of a flame independently from where it occurs. In this section a review of the blow-off studies in different combustion regimes is reported, focusing in particular on the non-premixed case with gaseous and liquid fuels.

Over the years significant effort has been directed at estabilishing relationships between the geometry, the operating conditions and the global extinction. As a result, some mathematical correlations have been developed which can give insight into how changes in operating conditions or geometry can affect the stability of a flame [33]. In this section several correlations for different geometries and different combustion regimes are reported.

1.2.1 Turbulent premixed flames

Consider first a premixed configuration, where fuel and air have been completely mixed before reaching the combustion chamber. In the laminar case of this combustion regime, the extinction occurs when the local flow speed exceeds the laminar flame speed which depends on the fuel, the equivalence ratio and the temperature of the fuel-air mixture [33]. In turbulent flows the speed of flame propagation is enhanced by turbulent diffusion and the effective flame speeds are higher. Thus, the stability range would be wider as reported by Korusoy and Whitelaw [57].

For premixed combustion using swirl or bluff body stabilization, the role of the recirculation zone is to retain a significant supply of hot combustion products

to continuously ignite the fresh reactants [33]. Kanury [51] defined the blow-off as the phenomenon arising when the time allowed by the flow is not long enough for the reactions to proceed to ignition or deflagration. For premixed flames, several theories for blow-off have been proposed [64; 77; 90; 99; 114] and an extensive literature is available that quantifies blow-off limits as a function of approach flow velocity, fuel type, stoichiometry, dilution, pressure, temperature, blockage ratio, and bluff body shape [31; 89; 96; 110; 115]. Longwell [64] suggested that blow-off occurs when it is not possible to balance the rate of entrainment of reactants into the recirculation zone, viewed as a well stirred reactor, and the rate of burning of these gases. Since entrainment rates scale as the ratio of the characteristic length and the bulk velocity it then follows that this criterion reduces to a Damköhler number blow-off criterion, using a chemical time derived from the well stirred reactor. A similar idea relates to an energy balance between the heat supplied by the hot recirculating flow to the fresh gases and that released by reaction [58; 109; 111]. In this view, blow-off occurs when the heat required by the combustible stream exceeds that received from the recirculation zone. This leads to the same entrainment-based, fluid mechanical time scaling as above, and the resultant similar Damköhler number blow-off criterion. Zukoski and Marble [115] suggested that the flame blows off when the time during which the fresh gas associates with the hot recirculation zone is too short for ignition to be accomplished. According to Spalding [99], the blow-off velocity should be proportional to the dimension of the flame-holder, the pressure, and the square of the laminar flame speed of the mixture.

Yamaguchi et al. [114] investigated the blow-off in a premixed propane-air flame stabilzed by cylindrical rod bluff-bodies. They concluded that a local extinction of the excessively stretched weak eddy-flames at the end of the recirculation zone triggers the blow-off of the flame. De Zubay [31] correlated the fuel/air ratio at the blow-off with the velocity, the pressure and the diameter of the bluff body. Zukoski and Marble [115] presented a criterion based on a characteristic chemical and a residence time being equal, using as characteristic length the length of the recirculation zone.

Muraganandam and Seitzamn [77] examined the evolution of the blow-off in a swirl combustor by chemiluminescence sensors and high speed imaging. Different

stages were observed as the equivalence ratio was decreased: detachment of the flame from the inlet, partial extinction events, new flame shape stabilized by the hot side walls of the combustor and loss of the flame.

Recently, Chaudhuri and Cetegen [23] studied the flame blow-off for lean premixed conical flames of a propane-air mixture, analyzing the CH* chemiluminescence signal from the base of the flame to determine the precursor condition that could be utilized to detect a probable blow-off. Nair and Lieuwen [78; 79] studied the transient dynamics of premixed flames near blow-off, defining two different stages: the emergence of localized extinction regions and then the violent flapping of the flame front. More recently, the change of flame shape as extinction is approached and the duration of the blow-off transient itself have been measured for non-swirling bluff-body flames by fast imaging (5 kHz) of OH* chemiluminescence and OH-PLIF [29; 53]. However, similar measurements do not exist yet for premixed swirled enclosed flames.

In the prediction of the extinction limit two commonly used empirical correlations for premixed flames are those of DeZubay [31] and King [55]. The basis for DeZubay's correlation was a series of rig experiments using disk shaped flame holders in a circular duct. Inlet velocity, pressure, and the diameter of the disk were varied. Based on the measure of the blow-off data, DeZubay derived a correlation parameter for predicting the extinction equivalence ratio (ϕ_{ext}). DeZubay's parameter is of the form:

$$\phi_{ext} \propto \frac{U_b}{P^{0.95}\ D^{0.85}} \tag{1.3}$$

U_b is the bulk velocity, P the pressure and D is the diameter of the disk.

King's empirical correlations were developed at elevated inlet temperature. The experiments spanned inlet velocities from 122 to 198 m/s, pressures from 0.35 to 0.85 atm, and inlet temperatures from 700 to 1,033 K. A single flame holder geometry was considered, so that no geometry information appears in the correlation. The correlation parameter is of the form: .

$$\phi_{ext} \propto P^{0.324}\ T^{1.07}\ (750 - U_b)^{0.252} \tag{1.4}$$

Ballal and Lefebvre [12] proposed a method for the prediction of the extinction

of premixed flame. It is based on the notion that flame extinction occurs when the amount of heat needed to ignite the fresh mixture being entrained into the wake region just exceeds the amount of heat liberated by combustion in that zone. The heat release has a main role in a swirl flame and its decrease, when the air flow rate is increased, affects the stabilization of the flame. Increasing the heat release (by changing the overall stoichiometry) results in benefits such as an increase in the recirculation, the turbulence kinetic energy levels, and flame stability [107].

The equation for the blow-off prediction of Ballal and Lefebvre is affected mainly by the inlet temperature (T_{inlet}), velocity (U), the characteristic dimension (D_c), the blockage ratio (B_g) and pressure (P):

$$\phi_{ext} = \left[\frac{U}{P^{0.25}\ T_{inlet}\ \exp(\mathrm{T_{inlet}}/150)\ \mathrm{D_c}\ (1-\mathrm{B_g})} \right]^{0.16} \tag{1.5}$$

It can be expressed more generally for the homogeneous case as:

$$\phi_{ext-1} \propto \left[\frac{m_{Air}}{P^{n}\ V\ \exp(\mathrm{T_{inlet}}/\mathrm{b})} \right]^{x} \tag{1.6}$$

where m_{Air} is the flow rate of air, n is the reaction order, V is the volume of the combustion zone and x is a constant determined experimentally. Ballal and Lefebvre [12] tested this correlation for their geometrical configuration, they used the following equation for calculating the equivalence ratio when extinction occurs:

$$\phi_{ext-1} = C \left[\frac{m_{Air}}{P^{1.25}\ V\ \exp(\mathrm{T_{inlet}}/150)} \right]^{0.16} \tag{1.7}$$

where C is an experimental coefficient equal to 1.2.

Radhakrishnan et al. [89] proposed a turbulent premixed flame extinction theory and a valuable correlation as follows. Assuming that combustion occurs in the small-scale structures of the turbulence, these authors postulated that extinction will occur when the time needed for the flame to propagate from one Kolmogorov-scale vortex to a neighbouring one exceeds the lifetime of the large eddies of the turbulence. Hence, extinction will occur when $\lambda/S_L > RL_t/u'$, where λ is the Taylor microscale, S_L the laminar burning velocity, L_t the integral

lengthscale, u' the characteristic large-scale turbulent velocity fluctuation, and R is some constant. If we assume that in a typical swirling recirculating flow the ratios $C_1 = u'/U_b$ and $C_2 = L_t/d$ do not depend on U_b (although they depend on the geometry and the swirl number), and considering the definition of the Taylor microscale for homogeneous isotropic turbulence ($\epsilon = 15\nu u'^2/\lambda^2$, $\epsilon = Au'^3/L_t$), then this extinction criterion postulates that extinction will occur when

$$\frac{1}{Da} = \left[\left(\frac{C_1}{C_2}\frac{15}{A}\right)\left(\frac{U_b}{d}\right)\left(\frac{\nu}{S_L^2}\right)\right]^{1/2} > R \tag{1.8}$$

where use has been made of the relationship $\lambda = (15/A)^{1/2} L_t (u' L_t/\nu)^{-1/2}$, with ν the kinematic viscosity. This correlation has not been used before for swirling non-premixed flames nor for sprays. In the original paper [89], its validation was based on extensive data sets with fully premixed flames in afterburner-type geometries without swirl. In this thesis, the correlation above will be tested for non-premixed and spray flames.

1.2.2 Turbulent non-premixed flames

In non-premixed combustion, fuel and oxidiser are initially separated. Non-premixed flames are encountered in a large number of industrial systems since they are simpler to design and build compared to the premixed flames. Moreover, non-premixed flames are safer to operate as flashback cannot occur [87]. The main difference with premixed flames described in the previous subsection is that while a premixed flame propagates in a direction normal to itself in order to consume the available reactant mixture, a non-premixed flame cannot propagate and instead it must remain attached to the stoichiometric surface between the fuel and oxidiser [20]. This peculiarity entails a possible different impact on quenching-based extinction mechanisms. In fact regions, where premixed flames propagate or diffusion flames are established, can occur in different fluid-dynamic conditions. In the premixed case charge can be formed very far from the region where the oxidation evolves. This in turns means that the reactant mixing processes are far from the combustion regions. In other words the presence of high quenching strain rate can be provided only in order to intensify the oxidation

process itself, but it is not intrinsic to the mixing process, for which turbulent is nearly a necessary requisite. In the second case mixing and combustion are simultaneous therefore the same strain rate intensification affects both processes. The turbulent mixing enhancement cannot be obtained without exposure the stoichiometric reacting region to quenching risk. This means that combustion processes and devices which have been developed in the practical systems have taken into account these different needs due to simultaneity or not-simultaneity of the mixing/combustion process with an implicit consequent impact on the extinction mechanism.

Chemical reactions occurs only because of diffusive molecular mixing of these components. If the chemistry is fast enough, a reaction layer forms at approximately stoichiometric conditions. In this layer, fuel and oxygen are consumed and reaction products are formed. Combustion is typically controlled by the rate of molecular mixing, although the chemistry becomes important if the chemical timescale compares with the timescale of the turbulence. In that case, local flame extinction might occur [84].

Having two inlets, one for the fuel and one for the oxidizer and defining the fuel stream (1) and the oxidizer stream (2), it is possible to keep track of the extent of the mixing between the conserved scalars emerging from each stream. The main term to describe the mixing is the mixture fraction ξ:

$$\xi = \frac{\beta - \beta_2}{\beta_1 - \beta_2} \tag{1.9}$$

At any point in the reacting mixture, the value of ξ gives the mass fraction of mixture that originated in the fuel feed. It will be equal to 1 in the fuel stream and 0 in the oxidizer stream [15]. Another parameter is the overall equivalence ratio, $\phi_{overall}$, defined as:

$$\phi_{overall} = \frac{m_{fuel}/m_{air}}{r_s} \tag{1.10}$$

The quantity r_s is the stoichiometric fuel-air ratio. For non-premixed flames the combustion chemistry does not occur at the overall equivalence ratio $\phi_{overall}$; instead, the flame tends to locate itself near the local stochiometric contour. Varying $\phi_{overall}$ has only an indirect effect on the chemistry; it can move the

location of the stoichiometric contour [32].

Another important quantity in non-premixed reacting flow is the scalar dissipation rate. It characterizes the local scalar gradients within the flowfield and is defined as $\chi = 2D(\nabla\xi \cdot \nabla\xi)$, where D is the molecular diffusivity and ξ is the mixture fraction. In laminar flames the relationship between the scalar dissipation rate and the global extinction has been studied [24; 40; 45; 54; 59]. It has been found experimentally that if the scalar dissipation rate is increased, extinction occurs, while simulations of unsteady flames have shown that the instantaneous scalar dissipation rate controls flame extinction [45; 59]. More recently, computational studies in turbulent flames have predicted that the scalar dissipation rate at the stoiciometric contour determines the local extinction [85; 100].

The study of extinction in flames stabilized in the stagnation flow formed by a pair of opposed jets has also provided valuable information into the mechanism of the extinction in turbulent flames [74; 91; 92]. The effect of strain rate on extinction time was quantified by imposing pressure oscillations. Results have shown that the extinction occurred at the end of a process of continous weakening of the flame through a series of cycles of local extinction and relight, and that large strain rates led to extinction.

Swirling motion is an efficient way to stabilize non-premixed flames; swirl extends the curved shear layer and produces extra turbulence generation and so enhances mixing and combustion intensity [46]. Moreover, it creates a recirculation zone transporting of hot combustion products at the root of the flame, where cold reactants are located. Feikema et al. [34] reported one of the first studies about the blow-off in non-premixed swirling flames. They measured the blow-off limit associated with an excessive air velocity and they observed that the flame at the maximum air velocity blows off suddenly without lifting off. Moreover, Feikema et al. [34] compared the blow-off limits with and without swirl, concluding that the swirl enhances the stability of lean flames since it creates a local region having a reduced velocity and a reduced local strain rate. A strain parameter, based on the ratio of air velocity to air tube diameter, was found, which collapes the blow-off curves for different conditions (burner size, swirl number) approximately to a single curve.

The local structure of swirling non-premixed gaseous-fuel flames has been

determined in the large body of work from the University of Sydney with the so-called "Sydney swirl flames" [28; 71]. These flames had strong enough swirl to create recirculation zones (RZ), and the fuel injection was in the main flow direction, usually at a velocity high enough that the fuel penetrated the RZ to create a jet-like flame, with a bulging base where finite-rate kinetic effects were observed due to the high mixing rates. One key conclusion, yielded by the point Raman and Rayleigh measurements, was that non-premixed flames show progressively more localised extinction as the global blow-off condition is approached, in agreement with piloted jet flames (e.g. Sandia series D-F [13]).

The spontaneous Raman scattering technique was used by Masri et al. [71] to perform measurements of mixture fraction, temperature, and the concentration of stable species in the recirculation zone of bluff-body stabilized flames. Two zones of almost homogeneous mixture were identified within the recirculation zone: a large outer region or vortex, which is fuel lean on average, but still within the lean reactive limit. An inner, smaller region that is close to the central fuel jet and has a stoichiometric mean mixture fraction. Masri et al. [71] observed that although chemical kinetic effects were still significant, they were not high enough in the recirculation zone to cause localized extinction, even in flames that were very close to blowoff,

In an extensive analysis of the structure of turbulent piloted flames of a range of fuels, Masri et al. [72] have generated diagrams that characterize the behavior of the flames respect to simple parameters like the stoichiometric mixture fraction (ξ_s) and the width of the reaction zone ($\Delta\xi_R$). The start of the localized extinction were correlated with respect to $\xi_s/\Delta\xi_R$. It was found that the localized extinctions decrease with increase of $\xi_s/\Delta\xi_R$. Dally et al. [28] investigated turbulent nonpremixed flames stabilized on an axisymmetric bluff-body burner with fuels ranging from simple H_2/CO to complex H_2/CH_4 and gaseous methanol. The fuel-jet velocity were varied to investigate the Damköhler number effects on gas emissions, localized extinction in the neck zone, and the structure of the recirculation zone dependency on the flow field. It was found that up to three mixing layers may exist in the recirculation zone, one on the air side of the outer vortex, one between the inner and the outer vortices, and one between the fuel jet and the inner vortex. The start of localized extiction as the flames approach

blow-off were consistent with results reported earlier for piloted flames by Masri et al. [72] .

Sutton and Driscoll [102] obtained simultaneous images of the instantaneous scalar dissipation rate field, the temperature field, and the fuel consumption rate field in a non-premixed turbulent flame. The fuel stream mainly consisted of carbon monoxide and it was surrounded by a coaxial pilot flame that contained lean premixed reactants acting as stabilization source for the flame. In particular, they showed that when a dissipation layer of sufficient strength overlaps with the stoichiometric contour, the fuel consumption rate decreases significantly and the temperature decreases indicating that local flame extinction occurs. They report experimental data demonstrating that the instantaneous scalar dissipation rate at the stoichiometric contour plays an important and direct role in local flame extinction in turbulent non-premixed flames. This was consistent with a direct numerical simulation study of non-premixed combustion by an investigation of local extinction and reignition in non-premixed turbulent flame, and by observing that the fluctuations of the scalar dissipation rate create extinguished regions on the stoichiometric surface [100]. Hult et al. [44] studied a turbulent jet diffusion flame by combining point OH-PLIF (33 kHz) with temperature or three-component velocity fields. They observed extinction events that could be correlated to local strain rate field and vortical structures. A modified Damköhler number was proposed by Driscoll and Rasmussen [32] to correlate the blow-off limits, measured in six previous studies of non-premixed flames, which were stabilized in high-speed airflows by bluff bodies or wall cavities. The analysis to identify the relevant Damköhler number was based on the assumption that the flame base exists in the shear layer and has a propagation speed that is matched to the local velocity. However, the most common description of non-premixed flame extinction is centered on the concept that high local scalar dissipation rates can cause localised extinctions, and this has been used to correlate extinction in a range of flames [74; 83].

Recently, fast OH-PLIF has been used to reveal the dynamics of the localised extinctions in the early regions of piloted jet flames [50; 101]. Similar work for swirling flames that are short (i.e. the fuel jet not penetrating the RZ), and hence closer to the type expected in gas turbines [34; 41], must be performed to

understand better the extinction processes in such practically-important flames. Such work will be presented in the following chapters.

The prediction of localised extinction in non-premixed jet flames (Sandia Flames D-F) has also been proven possible, with recent attempts based on LES providing very good results [37; 48]. However, validation of such LES methods also for other flames would be useful and this need additionally motivates the study of extinction of swirling non-premixed flames in this work.

1.2.3 Turbulent spray flames

The combustion of sprays of liquid fuels is of considerable technological importance for a diversity of applications including steam raising, furnaces, space heating, diesel engines, gas turbines and space rockets. Spray combustion was first used in the 1880s as a powerful method of burning relatively in-volatile liquid fuels. As matter of fact it remains the major way of burning heavy fuel oils today.

Since the physics behind two-phase combustion is much more complex than in gaseous combustion, its understanding is less advanced and hence still further investigation is needed. In addition to chemical reactions and molecular transport, which are present in pure gas phase phenomena, various processes inside the liquid phase and on surface between gaseous and liquid phases have to be considered: injection, atomization, coalescence, polydispersion, evaporation and turbulence.

The atomization of the liquid fuel produces a spray of small droplets in order to increase the surface area so that the rates of heat and mass transfer during combustion are greatly enhanced.

The atomization and dispersion processes have to be carefully coupled to achieve satisfactory distribution of fuel droplets in the airflow and appropriate sizes of the droplets. In fact, the droplets have to be small to allow for a rapid evaporation of the fuel and at the same time they should be large enough to avoid fuel trapping phenomena occurring at low Stokes number [21]. To create a uniform and fine spray with the proper dimension of droplets, several types of atomizers have been developed such as pressure atomizers, air-assist atomizers,

airblast atomizers. A sketch of these atomizers is reported in Fig. 1.3. In the present work the pressure atomizer was used for its good mechanical reliability and capability to sustain combustion at very weak mixture strength compared to the other types of atomizers [108].

In a pressure atomizer, the liquid is discharged through a small aperture under high applied pressure. An example is the pressure swirl atomizer (Fig.1.3a) where a circular outlet orifice is preceded by a swirl chamber into which liquid flows through a number of tangential holes. The liquid emerges from the discharge orifice as an anular sheet, which spreads radially outward to form a hollow conical spray. The main advantage of using a pressure swirl atomizer is the wide spray angle in the range 30 - 170° [60]. Thus, the atomization is affected by different parameters: type and size of the atomizer, physical properties of the liquid being atomized and the gaseous medium into which the droplets are discharged. For pressure swirl atomizer the critical dimension is the thickness of the liquid sheet as it leaves the atomizer.

Considering the general case of a liquid fuel and oxygen as gaseous oxidizer, the fuel evaporates from the liquid surface and diffuses to the flame front as the oxygen moves from the surroundings to the burning front. The evaporation rate depends on the pressure, temperature, the transport properties of the gas, the volatility, the diameter of the drops in the spray, and the velocity of the droplets relative to that of the surrounding gas [39].

As the liquid fuel leaves the nozzle, it becomes turbulent and the outer surface of the jet breaks up into droplets. The turbulent eddies formed in the shear layer will engulf the surrounding fluid in the jet, and mixing subsequently take place on the molecular level at the two-fluid interface. Moving away from the nozzle, the mass of air within the spray increases, the spray diverges, its width increases, and the velocity decreases [98]. After the formation of the spray, i.e. a disperse liquid phase in the gas phase, evaporation and mixing is leading to the formation of combustible mixture.

Thus, there are several important parameters involved in spray combustion including fuel composition, droplet size, gas composition, temperature and the relative velocity between the droplets and the air and the combustor pressure [25].

According to Williams [110] in spray combustion for the same overall equivalence ratio (cumulative mass of gaseous fuel and droplets), the flame speed and the flame structure are different when varying the droplet diameter and the vapour fraction (relative amount of fuel vapour). Depending on those parameters, the flame can propagate in the interdroplet spacing if there is sufficient fuel vapour there. Moreover, droplet diffusion flames can occur for sufficiently large droplets (typically when the droplet diameter is higher than 20 μm) if the interdroplet spacing is not rich.

The flames may be divided into several zones, as shown in Fig. 1.4. With analytical methods, Silverman et al. [97] distinguished five parts. The first three parts are respectively a primary evaporation zone with a length l, a heating zone, and a "homogeneous" reaction zone. The fuel evaporated in the first two zones reacts in the "homogeneous" reaction zone. Behind it, the surviving droplets keep evaporating at a high rate. If oxygen remains, the fuel burns as soon as it evaporates, in the so-called droplet burning zone. Finally, when there is no more oxidiser, droplets, if any, finish evaporating in a secondary evaporation zone.

In spray combustion, paraffinic fuels, such as n-heptane, are widely used; they operate at lower fuel/air ratios than aromatic fuels. They exhibit much higher values of weak-extinction AFR (Air-fuel ratio) than gas oil. These better lean blow-off values for fuels of low specific gravity are due partly to their lower fuel viscosity, which produces a finer spray, and partly to their higher volatility. The combined effect of finer atomization and higher volatility is an acceleration of the rate of fuel evaporation, allowing operations at leaner mixture strengths [60]. The relevance of the n-heptane in the spray flames is due to the fact that it is a primary reference fuel for octane rating in internal combustion engines. It has a cetane number of approximately 56, which is similar to the cetane number of conventional diesel fuels. The n-heptane is often chosen for its high volatility with a low boiling point (T_{eb}=371.58 K), because it improves the flame stability.

Until the early 1970s, the problem of blow-off for spray flames had not been examined extensively. Most studies have been done on gaseous fuels. In addition, some of these studies have been done with bluff-body stabilization and not swirl stabilization. Little work has been done for understanding the mechanisms behind the blow-off for swirl-stabilized combustion using liquid fuel.

Marinov et al. [69] investigated the weak extinction limit in a confined swirl-stabilized flame supplied with kerosene (spray combustion) or natural gas (non-premixed combustion). They observed similar flow fields for the stable kerosene and the stable methane combustion (similar recirculation zones), although differences between the flames were observed close to the blow-off. Recently, Burguburu et al. [18] conducted an experimental study for the analysis of aeronautical spray injection system in high temperature and pressure conditions, measuring the blow-off limits and evaluating the effects of hydrogen enrichment to increase the flame stability. However, detailed flame structure information was not available.

Spray flames have been studied only little from the point of view of localised extinction [70] and from the point of view of providing detailed data for LES studies [47]. Despite the fact that many global blow-off correlations have been proposed [5; 12; 62; 86; 113] for gas-turbine-like swirling flames, details on the flame structure as extinction is approached are not available.

Equation 1.7, reported for the premixed case by Ballal and Lefebvre [12], can be used to predict the blow-off limits of combustion chambers supplied with heterogeneous fuel/air mixtures, provided that the rate of fuel evaporation is sufficiently high to ensure that the system is fully pre-vaporized. If the fuel does not fully vaporize a more complex correlation was reported for gas turbine combustor [12]:

$$\phi_{ext-2} = C \left[\frac{m_{Air}}{P^{1.25}\ V\ \exp(\mathrm{T_{inlet}}/150)} \right]^{0.16} \left[\frac{\rho_f}{\rho_g\ V\ \log(1+\mathrm{B})} \right] \left[\frac{m_{Air}\ D_{32}^3\ A}{(I_u/100)\ \mu_g} \right]^{0.5} \tag{1.11}$$

where C is an experimental costant, V is the volume of the combustion zone, ρ_f is the density of the liquid fuel, ρ_g is the density of the air, B is the fuel mass transfer number, D_{32} is the sauter mean diameter, A is the area of the combustion, I_u is the percentage of turbulent intensity, and μ_g the dynamic viscosity.

Ballal and Lefebvre modified equation 1.11 for baffle-stabilized flames, here the role of turbulence is more complex because it affects not only the rate of fuel

evaporation, but also the rate of entrainment of air into the wake region. Thus, equation 1.11 becomes:

$$\phi_{ext-3} = \left[\frac{C\ \rho_f}{d\ \log(1+\mathrm{B})}\right]\left[\frac{U D_{32}^3(1+0.12T_u)}{\rho_g\ \mu_g\ (I_u/100)B_g(1-B_g}\right]^{0.5} \left[\frac{U\ (1+0.12T_u)}{P^{0.25}\ d\ (1-B_g)T_{inlet}\exp(\mathrm{T_{inlet}}/150)}\right]^{0.16} \tag{1.12}$$

where B_g is the blockage rato.

If the fuels does not fully vaporize, then the *effective* fuel/air ratio will be lower that the nominal value. For fuels with low volatility and large mean drop size, this additional time is often the main factor limiting the overall rate of heat release. If the fuel does not fully vaporize, then clearly the *effective* fuel/air ratio will be lower than the nominal value. However, if the fraction of fuel that is vaporized is known, or can be calculated, it can be combined with the previous equation to yield the fuel/air ratio at lean blow-off, i.e.:

$$\phi_{ext\ non-premix} = \frac{\phi_{ext\ premix}}{f_f} \tag{1.13}$$

where f_f is the fraction of fuel that is vaporized. It was suggested that:

$$f_f = \frac{8\ \rho_g\ V_c\ \lambda_{eff}}{f_{pz}\ m_{Air}\ D_0^2} \tag{1.14}$$

f_{pz} is the fraction of the total air flow rate, m_{Air} that enters in the combustion chamber, D_0 is the initial droplet diameter, V_c is the volume of the combustor and λ_{eff} is the effective evaporation constant. If the value of f_f exceed unity, this means that the time required for fuel evaporation is less than the time available so the fuel is fully vaporized within the recirculation zone [5; 12]. In this case:

$$\phi_{ext\ non-premix} = \phi_{ext\ premix} \tag{1.15}$$

If f_f is lower than 1, the general equation for the heterogeneous mixture

becomes:

$$\phi_{ext} \propto \left[\frac{f_{pz}}{V_{pz}^{(1+x)}}\right]\left[\frac{m_{Air}^{(1+x)}}{P^{(1+nx)}\ \exp(\mathrm{xT_{inlet}/b})}\right]\left[\frac{D_0^2}{\lambda_{eff}\ LCV}\right] \tag{1.16}$$

where LCV is the lower calorific value and V_{pz} is the volume of the combustion primary zone. The first term on the right-hand side of equation 1.16 is a function of combustor design. The second term represents the combustor operating condition, and the third terms embodies the relevant fuel-dependent properties. Not enough experimental data exist to accurately determine the exponents $(1 + x)$ and n. However, to simplify the expression, the order of V_{pz} and m_{Air} are taken to be the same with the order of the pressure term somewhat higher based on the reaction order n. The simplest form in which the equation can be expressed is:

$$\phi_{ext} \propto \left[\frac{A'' f_{pz}}{V_{pz}}\right]\left[\frac{m_{Air}}{P^{1.3}\ \exp(\mathrm{xT_{inlet}/300})}\right]\left[\frac{D_0^2}{\lambda_{eff}\ LCV}\right] \tag{1.17}$$

A'' is defined as a constant whose value depends on the geometry and mixing characteristics of the combustion zone and was arrived at experimentally. The main drawbacks, observed by Ateshkadi et al. [5], to this extinction model are:

1. Assigning appropriate values of V_{pz} to a given combustor configuration is challenging.

2. Values of f_{pz} are difficult to attain for various combustor geometries.

3. The model demands an accurate knowledge of mean drop size over the entire range of operating conditions .

4. No explicit relationship is provided between the blow-off limit and the details of the combustor geometry.

The level of agreement between the measured and predicted values is satisfactory for the Ballal and Lefebvre configuration.

More recently, Ateshkadi et al. [5] tested a non-premixed configuration with liquid fuel (Jet-A) and different swirl configurations. The blow-off was induced starting from a steady state operation in which the combustor components were

at a steady-state temperature. By gradually reducing the fuel loading until the reaction became extinct, the fuel/air ratio at that point was recorded. Images of the reaction near extinction were taken using a high-speed CCD camera. They tried to simplify the expression for the blow-off model as a function of the geometry starting from Ballal and Lefebvre considerations. They simplified the expression of Ballal and Lefebvre [12] by simply using the geometrical volume (V_c) instead of V_{pz} which was a reasonable assumption given the simplified geometry of the combustor that they utilized. The second assumption was to assign the value of unity to f_{pz} since no jets interact with the main dome flow. A representative Sauter Mean Diameter, calculated from a correlation by Lefebvre [61], was substituted for D_0 as the initial droplet drop diameter of the spray. They varied the value of A'' until the calculated values of ϕ_{ext} match the measure values. This coefficient is a function of mixing characteristics of the configurations. The lowest value of A'' are attributed to poorer mixer performance, which led to lower fuel/air ratios (increase instability). An additional modification was made on the temperature dependence term. They found this type of correlation between the extinction and the temperature:

$$\phi_{ext} \propto \frac{B''}{\exp(\mathrm{T_{inlet}}/600)} \tag{1.18}$$

where B'' is:

$$B'' = 7 \times 10^{-6} \times T^2 \; - \; 3.6 \times 10^{-3} \times T \; + \; 1.424 \tag{1.19}$$

The equation for B'' is a correlation to provide the best fit curve. The resulting expression for predicting the extinction limit then becomes:

$$\phi_{ext} \propto \left[\frac{A'' f_{pz}}{V_c}\right] \left[\frac{m_{Air}}{P^{1.3}\, \exp(\mathrm{xT_{inlet}}/600)}\right] \left[\frac{D_0^2}{\lambda_{eff}\; LCV}\right] \; B'' \tag{1.20}$$

These previous types of correlations are used by designers as a starting point, but cannot be expected to accurately predict all geometric configurations. More recently researchers have improved the physical description used to develop stability correlations with the hope of developing more accurate, general stability correlations. The stability is seen as being determined by competition between

a chemical and a flow (or residence) timescale. These blow-off correlations lead to the same form of correlation in terms of a Damköhler number, considering a fluid mechanics time and a chemical kinetic time.

As it has been previously described the fluid mechanic time scale is generally scaled as some mean residence time, L/U, where L is a characteristic dimension (bluff body diameter, annular inlet diameter, length of recirculation zone, shear layer thickness), and U is a characteristic velocity [96]. The success of the Damköhler number approach depends on how the timescales are defined and calculated. In several correlations the residence time is calculated from the inlet velocity and the characteristic dimension of the flame holder. This timescale is said to represent the residence time in the shear layer. The chemical time is described as the ignition delay time of the mixture.

Plee and Mellor [86] developed one of the most advanced timescale correlations for non-premixed-liquid-fuel flames. In addition to chemical and flow timescales, they included timescales to account for mixedness and fuel droplet penetration into the reaction zone. For well-mixed conditions with a fully vaporized fuel, this correlation simplifies to a form very similar to the premixed case, and the stability is determined based on competition between a flow and chemical timescale. Plee and Mellor use a global flow velocity and flame holder dimension to define the residence time [86]. Mellor separates the combustion process into heterogeneous, fluid mechanical, and chemical effects, each of which is characterised by an appropriate time scale and easily computed from combustor inlet conditions [76]. The key to the prediction's success is the identification of the important physical processes occurring in a particular region of the flow field through either detailed probing or examination of relevant literature.

At least four characteristic times are expected to be important in the stabilization of non-premixed flames with liquid fuel [76]:

Two fluid mechanics times:

1. **Mixing time or residence time or shear layer time** (τ_{sl}): the turbulent mixing process, occurring in the shear layer region between the fresh incoming air and the recirculation zone, is characterized by τ_{sl}. Tuttle et al. [105] quantified this mixing time in terms of a characteristic large-scale eddy lifetime. However, since turbulence parameters are not easily mea-

sured in practical systems, τ_{sl} is assumed directly proportional to geometric dimension and inversely proportional to a convective velocity. For blow-off, the turbulent mixing time is taken to be a ratio of the flame holder width (L) which is also a measure of the size of the recirculation zone, divided by the air velocity at the edge of the stabilizer (V_a). V_a is evaluated at the temperature in the shear layer, which must be higher that the inlet temperature because it is adjacent to a hot recirculation zone; this accounts for the acceleration of the air flow as a result of the increased temperature. For confirming that the characteristic residence time is given by the shear layer, Zukoski and Marble [116] found that the temperature in the RZ is uniform (approximately 90% the adiabatic flame temperature) and that the ratio of the wake temperature to the adiabatic flame temperature remains approximately constant as the air velocity increases toward the blow-off limit. They concluded that the time that a fluid particle spends in the recirculation zone is too long to be characteristic of blow-off; rather, it is the purpose of the recirculation zone to provide heat and free radicals to the shear layer [116]. Furthermore, because the residence time in the wake region exceeds the shear-layer residence time, the flame in recirculation zone should be extinguished after that in the shear layer. Since the recirculation zone represents only minor heat release relative to the main stream flame, this final blowout related to RZ is only of secondary interest.

2. **Atomization time or fuel injection time** (τ_{fi}): a second fluid-mechanical time is associated with the turbulent mixing of fuel and oxidizer in the region of the fuel injector, which is expected to be particularly important in combustors utilizing air-blast and air-assist nozzles. For swirl pressure atomizers τ_{fi} is only of limited importance since very little oxygen is available near the point of injection.

Two chemical/evaporation times:

1. **Evaporation time or fuel droplet life time**, τ_{eb}, incorporates heterogeneous effects associated with the fuel spray and vaporization rate. The lifetime is defined from the Godsave law [60]. As an approximation to the

overall evaporation rate, the initial droplet diameter is taken to be the initial Sauter mean diameter (SMD). The evaporation constant, λ, is [60]:

$$\lambda = \frac{8\ k_g}{\rho_{liquid}\ c_p\ \rho} \ln(1+\mathrm{B})\ (1\ +\ 0.276\ \mathrm{Re_d^{1/2}}\ \mathrm{Sc^{1/3}}) \tag{1.21}$$

where k_g is the gaseous thermal conductivity, c_p is the gaseous specific heat, ρ_{liquid} is the fuel density at boiling point temperature, B is the transfer number, Re_d the droplet Reynolds number and Sc the Schmidt number of the gas phase.

2. **Ignition delay time or homogeneous chemical reaction time**, τ_{hc} : this time represents the homogeneous chemical reaction of fuel and oxidizer. This process occurs after the fuel and oxidizer have been mixed on a molecular level and it is a function of local equivalence ratio, inlet temperature, and pressure. τ_{hc} describes an ignition delay time for flame stabilization that is an exponential function of the temperature. The ignition delay time is usually evaluated at the highest temperature in the system since regions characterized by this temperature are the last to be extinguished and thus it is assumed that it controls the flame stabilization process. Nevertheless, a better representation of the temperature is an average between the adiabatic flame temperature and the inlet temperature [86]. In fact the recirculation zone is not completely surrounded by a hot reacting shear layer and the outer shear layer at the edge of the disk is almost entirely free of fuel and should be relatively unreactive.

Plee and Mellor characterized also the times controlling the blow-off [86]. They observed two different behaviours: when the fuel-penetration effects are negligible and when they are not. When the fuel-penetration effects are negligible, the heterogeneous combustion include both fuel evaporation and fuel vapour ignition in the same time span. The droplets represent a perturbation on the flame-stabilization process that just narrows the stabilization limit and the characteristic times can be compared according to:

$$\tau_{sl} \sim \tau_{hc} + a\ \tau_{eb} \tag{1.22}$$

where τ_{eb} is computed from the d^2 law and evaluated under conditions in the shear layer. The parameter a is needed since these times are not 'absolute' and they are chosen empirically according to the best fit of the experimental data. The characteristic time correlation for one of the configurations tested by Plee and Mellor is shown in Fig. 1.5a. It can be seen that one approaches the blow-off limit by increasing the velocity (decreasing τ_{sl}), increasing the initial droplet size (increasing τ_{eb}) and decreasing the overall equivalence ratio (increasing τ_{hc}). The correlation also predicts that droplet effects will become important at high velocities (small τ_{sl}) since at this point τ_{hc} and τ_{eb} are the same order of magnitude. This has been verified experimentally by Plee and Mellor [86]. The characteristic time model includes variations in pressure, inlet temperature, reference velocity, flame-holder geometry, fuel type and injector size with a minimum amount of algebra. Knowledge of the flame-holder configuration inlet conditions and atomization determines τ_{sl} and τ_{eb}; τ_{hc} can easily be computed that is a function of the inlet conditions and the extinction equivalence ratio.

When the fuel-penetration effects are not negligible, as droplet evaporation times (τ_{eb}) increase, the flame structure is believed to change in the manner described in Fig. 1.6. Liquid fuel penetrates the existing shear layer and creates a free-stream flame where the fluid mechanics in this region are characterized by τ_{fi}, a fluid-mechanical mixing time associated with the fuel-injection process. Since more time is available for ignition ($\tau_{sl} + \tau_{fi}$) when fuel penetration effects are important, the overall equivalence ratio at blow-off is much lower resulting in wider flame-stabilization limits. Assuming that fuel penetration is important to the flame stabilization process, the mixing time (L/V_a) is modified as follows to include this effect:

$$\tau_{sl} = L/V_a \ + a \ \tau_{fi} \tag{1.23}$$

The fluid-mechanical mixing time τ_{fi}, associated with the fuel-injection process, is related to a fuel-penetration length scale (L_{fp}) divided by an appropriate velocity in the free stream (V_a). In synthesis Plee and Mellor correlated the characteristic

times model including fuel-penetration effects according to [86]:

$$\tau_{sl} + a\ \tau_{fi} \approx \tau_{hc}\ + 0.011\ \tau_{eb} \tag{1.24}$$

The inclusion of L_{fp} accounts for the lengthening of the shear layer region as a result of fuel penetration and evaporation. Plee and Mellor tested different configurations (diameter of the flame-holder) and different type of fuels (Jet A, JP 4, diesel, C_3H_8). All the flame stabilization data were plotted for different cases (Fig. 1.5b) of the evaluated times, where were correlated using the following general equation (Fig. 1.5b):

$$\tau_{sl}\ + 0.12\ \tau_{fi} = 2.12\ (\tau_{hc}\ +\ 0.011\ \tau_{eb})\ +\ 0.095 \tag{1.25}$$

where characteristic times are evaluated in the same manner as discussed previously. Evaporation time, τ_{eb}, is negligible for mixtures in which the fuel is completely vaporized before combustion inception. Fuel injection time, τ_{fi}, has to be taken into account when the fuel-penetration effects are present.

Knaus et al. [56] argued that the existing correlations are unsatisfactory for two reasons:

1. The physical justification for existing correlations is based on local processes, but the local processes are often estimated from global parameters. Calculating local parameters directly would increase accuracy and make the methodology more general.

2. The stability correlations are highly dependent on empirical data. The empirically derived parameters do not generally extrapolate well to new configurations, so that experimentation is required when applying an existing correlation to validate or modify an existing correlation. The lack of a concise description of the conditions for which the existing correlations were derived limits the ability to extrapolate these correlations to new conditions.

Knaus et al. [56] applied a different approach: low-order CFD calculation are used to determine the local velocity field in the wake of the flame holder. Reactor models are used to calculate chemical timescales for the flow. A Damköhler field

in the wake of the flame holder is calculated and used to determine stability; calculating $\tau_{res}= k/\epsilon$, the ratio of turbulent kinetic energy and dissipation to form the flow timescale, while τ_{chem} are calculated based on ignition delay time calculations in a perfectly stirred reactor model. This method works well for predicting the blow-off in their configuration.

In summary, although extensive work has been done on developing tools for predicting the blow-off, some inconsistencies have been observed which may or may not be dependent upon the type of geometry used or the type of fuel or the fuel composition. In particular, empirical coefficients have been used in the spray combustion regime to collapse the experimental data. A simple correlation is necessary, trying to avoid the use of empirical coefficients to collapse the measured values.

1.3 Scope of the thesis

Due to the stringent emission requirements, modern gas turbine combustors work under lean conditions, which lead to lower flame temperatures and therefore reduced NO_x emissions. The operation of a combustor close to the blow-off limit increases the risk of a complete flame extinction. It poses a significant safety hazard when occurring in aircraft engines and requires an expensive shutdown and restart procedure in land-based engines for power generation. So, a deep understanding of blow-off is necessary.

This work examines the dynamics of blow-off for non-premixed and spray flames involving swirl stabilization and focusing on short flames. The same burner has been used for different combustion regimes, which suggests that, to a large extent, the aerodynamics, mostly determined by the air flow, is similar among the three types of flame.

The objectives of this work are

- to visualize the alteration of the flame shape as blow-off conditions are approached;
- to create a larger database of experimental results of non-premixed gaseous flames and spray flames close to the extinction limit in laboratory scale

burners with similar aerodynamic pattern;

- to examine the blow-off transient behaviour by high-speed diagnostics;
- to measure the duration of the blow-off event;
- to examine if a single correlation, not based on empirical coefficients, is capable to predict the blow-off limits for different combustion regimes.

1.4 Structure of the thesis

Chapter 2 provides a description of the experimental apparatus and the diagnostics used to study the blow-off and the flame stabilization propagation in different combustion regimes. In Chapter 3, several results of the velocity field in the combustion chamber are presented.

In Chapter 4, experimental measurementes are reported to study the extinction and the flame shape of non-premixed gaseous case. The duration of the blow-off and the prediction by a Damköhler correlation are presented as well. In Chaper 5, the blow-off study has been extended to two-phase flows using two different liquid fuels: n-heptane and n-decane. Finally, in Chapter 6, the findings of the investigation are summarised and guidelines for future research are suggested.

1.5 Figures for Chapter 1

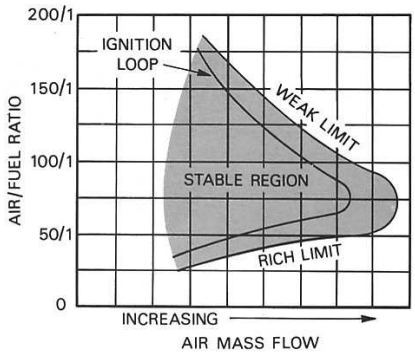

Figure 1.1: Combustion stability limits [19].

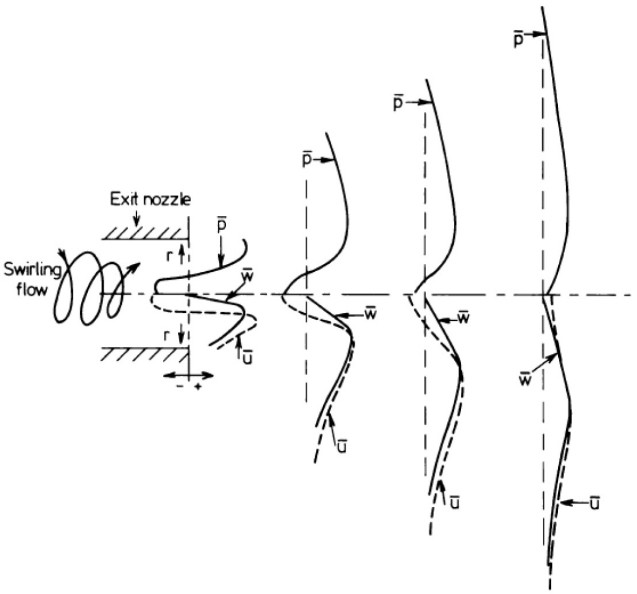

Figure 1.2: Schematic of the formation of a recirculation zone by swirl [103].

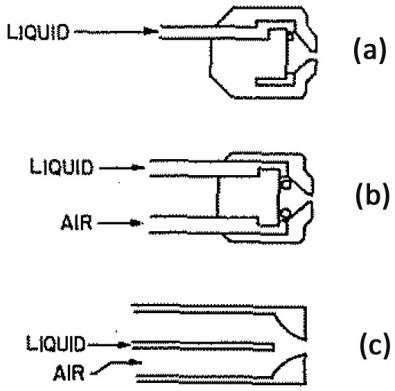

Figure 1.3: Schematic of (a) the pressure swirl atomizer, (b) the air-assist atomizer and (c) the air blast atomizer. Figure adapted from [60].

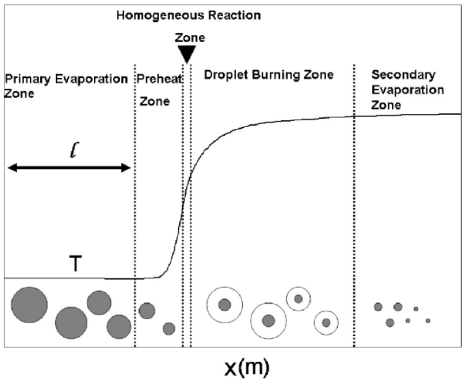

Figure 1.4: Schematic of the temperature profile across a laminar freely propagating premixed spray flame with a large Sauter Mean Diameter. The post evaporation zone exists in a rich case only [97].

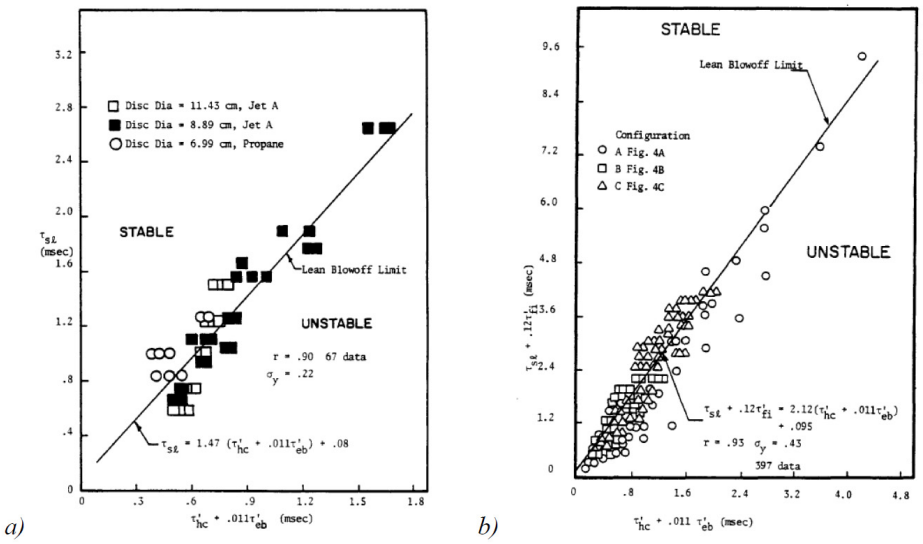

Figure 1.5: (a) Characteristic time correlation (negligible fuel-penetration effects); (b) Complete characteristic time correlation [86].

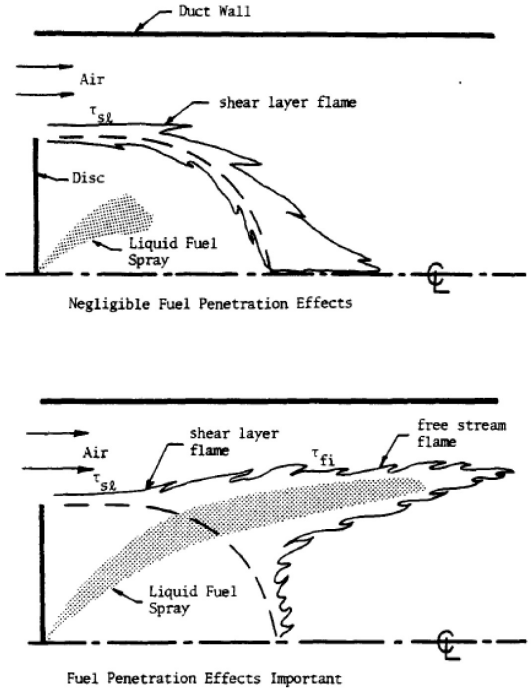

Figure 1.6: Burner schematic illustrating the effect of fuel penetration on flame structure, on the top when the penetration effects is negligible and below when the penetration effects is not negligible [86].

Chapter 2

Experimental methods

This chapter describes the experimental apparatus, along with the method of its operation. All experimental techniques will be stated, including the equipment used and their specifications.

The chapter begins with a detailed presentation of the burners (Section 2.1). Throughout the thesis a number of variables that were measured, such as the velocity field and the OH* chemiluminescence, will be used to describe the conditions in the combustion chamber. These variables are also defined in the current chapter. Planar Laser Induced Fluoresence (PLIF) imaging is described and explained in terms of the set up and accuracy. Furthermore, the high speed imaging technique is described with a clarification of the chemiluminescence measurements. The chapter ends with a presentation of the method used in measuring the extinction time.

2.1 Burners

In the present work, two burners were used: the non-premixed burner and the spray burner. The burner has been developed from previous studies concerning lean premixed flame response to forcing [9], non-premixed flame spark ignition [2], and spray flame spark ignition [68]. Some modifications have been done in the present work to design a non-premixed configuration as clarified in Section 2.1.1. However, both burners have the same dimensions in order to keep the aero-

dynamic pattern similar. These burners are fully described in the next sections.

2.1.1 Non-premixed flame apparatus

Figure 2.1 shows a schematic diagram of the rig designed for the turbulent non-premixed case. The burner geometry consisted of a 350 mm long circular duct of D=37 mm inner diameter, fitted with a conical bluff body of diameter d=25 mm giving a blockage ratio of 50% (Fig. 2.1). It was virtually identical to the bluff-body burner described in [63] which used a square glass enclosure (width of 95 mm and a length of 150 mm) made of synthetic optical-quality quartz which provided optical access for the imaging and also avoided overall equivalence ratio ($\phi_{overall}$) variations due to possible air entrainment from the surroundings (Fig. 2.2 b). The confinement would also be a deciding parameter due to the resulting blockage ratio of the bluff body; walls constrain the flow field and influence the recirculation zone. The whole burner was built with stainless steel. The outlet was open to the atmosphere. The air entered from the annulus between the outer duct wall and the bluff body at 298 K. Swirl was imparted by a static swirler which consisted of six vanes at 60° with respect to the flow axis located 41.6 mm upstream of the bluff body plane (Fig. 2.3 a). The direction of the air swirl was clockwise when looking at the nozzle from the combustion chamber (Fig. 2.3 b). An expression for calculating the swirl number (S_N) has been reported in the Introduction taken from Ref. [14]. For an annular swirler with constant vane angle θ (60°) :

$$S_N = \frac{2}{3}\frac{1-(D_{hub}/D_{sw})^3}{1-(D_{hub}/D_{sw})^2}\tan\theta \tag{2.1}$$

where D_{hub} and D_{sw} represent the swirler hub diameter (11 mm) and the swirler diameter (37 mm) respectively. The swirl number calculated for the present configuration is 1.23.

The bluff body had a central pipe of diameter 4 mm so as to feed the fuel. The fuel is methane, properties are reported in Table 2.1. Air and fuel flow rates were controlled using Alicat Mass flow controllers. The reported bulk velocity at the annular passage, U_b, is uncertain to ±3%. The final experimental set up of the non-premixed configuration is showed in Fig. 2.4.

Table 2.1: Properties of methane at 298.15 K and 1 atm [33].

Property	Methane
Density (kg/m^3)	0.651
Flammability limits (ϕ)	0.46 - 1.64
Autoignition temperature in air (K)	813
Adiabatic flame temperature (K)	2226
S_L at stoichiometry (m/s)	0.40
Stoichiometric fuel/air mass ratio	0.055
Lower heating value (MJ/kg)	50.0

2.1.2 Spray flame apparatus

A commercial pressure-swirl atomizer by Lechler has been used for the experiments involving sprays (Fig. 2.5a). The general mechanism of this type of atomizer involves the use of high pressure in the atomizer to accelerate the liquid into a central swirl chamber. The spiral grooves in the swirl inserts ensure an efficient whirling of the liquid. As a result, the contact surface of the atomized liquid is significantly increased within a remarkably narrow droplet spectrum. It provides a fine, uniform hollow cone spray; the supplier certifies a spray cone of around 60° [1]. The nozzle exit diameter was 0.15 mm and was housed inside the bluff body. A detailed sketch of the bluff body, where the atomizer was located, is reported in Fig. 2.7b. The fuel injection system was connected to a tank of liquid fuel pressurised by nitrogen (Fig. 2.6).

The atomization turned out to be one of the key and most delicate stages of the present experiment. The main issue during the present work was the processing of a very low liquid flow rate and the achievement at the same time of a good atomization quality. Once the fuel injection was open the spray coming out from the pressure swirl atomizer showed different temporary stages before becoming a well-defined hollow-cone spray. This stages have already been well described by Lefebvre [60].

Large alkanes such as n-decane and n-dodecane are commonly used as surrogates for diesel and jet fuel to represent the bulk straight-chain paraffin compo-

nents, whereas n-heptane and iso-octane have been adopted as primary reference fuels to represent gasoline. In this work two liquid fuels was used: n-heptane and n-decane. Their properties are reported in Table 2.2.

Table 2.2: Properties of n-heptane and n-decane fuels at 298.15 K and 1 atm [104].

Formula	Fuel	MW (kg/kmol)	Boiling pt. (°C)	T_{ad} (K)	ρ_{liq} (kg/m^3)
C_7H_{16}	n-Heptane	100.203	98.4	2,274	684
$C_{10}H_{22}$	n-Decane	142.284	174.1	2,277	730

N-heptane was chosen due to its quick evaporation that allows spray flames to be stabilised at a laboratory-scale burner without preheating the air [68]. Moreover, n-heptane has a cetane number of approximately 56, which is similar to the cetane number of conventional diesel [95]. N-heptane used in the present work is high-purity laboratory grade fuel (99+%). N-decane was chosen due to its lower volatily. Its chemical and physical properties are closer to the real jet fuels.

As shown in Figure 2.7 a, all the geometrical details of the burner except for the spray injection are identical to the non-premixed burner, which ensures an aerodynamic field as close as possible between the two flame types.

2.2 Flow measurement methodology

2.2.1 Flow-rate measurements

The air flow was supplied by the laboratory compressor after a two-stage preparation arrangement, consisting of a regulator/pre-filter combination and a coalescing filter (Fig. 2.4). The regulator was used along with a pressure gauge to adjust and mantain the back pressure at 5.0 bar. The first stage pre-filter acted as a high efficiency dryer and particulate purifier, removing water droplets, residual humidity and particles down to 25 μm according to manufacturer's specifications. The second stage filter contained an activated carbon element and acted as an oil droplet and vapour oil purifier. It was also used to remove any hydrocarbon

odour traces. Its rated maximum oil content and particle removal in the outlet was 0.003 ppm and 10 nm respectively. The air flow rate was then controlled with a Alicat Mass Flow Controller with a maximum flow rate of 1500 L/min at normal conditions. It had the following technical specifications: an accuracy of 0.8% of reading plus 0.2% full-scale (based on actual factory calibration), and a repeatability of 0.2% reading.

Methane in the non-premixed rig was supplied from commericial compressed cylinders at 99.999 % vol/vol purity and regulated cylinder gauge pressure of 2.0 bar. It passed through and controlled using an Alicat mass flow controller. It had a maximum flow rate of 100 L/min at normal conditions and the same specifications (and accuracy) as the AIR-MFC described before.

For the spray case the fuel flow rate for the liquid fuels was set by a mass flow controller (Bronkhorst, LIQUI-flow, L30, [0-2] g/s) with an uncertainty of ± 0.02 g/s and a feeding tank pressurised by nitrogen at 0.5 MPa gauge pressure. Nitrogen at 99.9995% vol/vol purity was supplied from a compressed cylinder regulated at 6.0 bar. N-heptane and n-decane were used and calibration of the Mass Flow Controller (MFC) was performed by measuring, at room conditions, the volume of the liquid and hand-held stopwatch as a function of the setting on the MFC.

2.2.2 Determination of the blow-off point

According to Lefebvre [61], the blow-off limit can be determined in two ways: either stable combustion is established at a fixed air mass flow rate, and the fuel flow is varied until extinction occurs; or, the fuel flow rate is kept constant, and the air mass rate flow is increased to the point of extinction. In the present work and for both flames, the second method was chosen. Once the flow was stable and the flame was stabilized, the air flow rate slowly increased in steps of 2% (0.258 m/s) every 20 seconds until blow-off occurred. A flow of air without any fuel flow in the combustor was used to bring the temperature of the burners top part back to ambient temperature between two measurements. Blow-off measurements were carried out for bulk velocitites (U_b) ranging from 14 to 30 m/s.

2.2.3 Laser Doppler Velocimetry

The development of continuous wave gas lasers has made it possible to use the Doppler effect in an optical non-intrusive method for measuring the velocity of gases, liquids and solids. The method is called Laser Doppler Velocimetry (or Anemometry) or LDV (LDA). In this technique a laser beam is split into two parallel beams. A lens focuses both beams and then it creates an overlap region called the measuring volume (MV). The technique is based on Doppler shift of the light reflected (and/or refracted) from a moving seeding particle within the MV.

The LDV technique is largely used in both research and industrial applications. Its main advantage over conventional measurement techniques (e.g. hot-wire anemometry, pressure probes) is that it is non-intrusive [4].

Three types of configuration are possible: the backscattering mode, the off-axis scattering mode, the forward scattering mode. The majority of light is scattered in a direction away from the transmitting laser, and in particular in the early days of LDA, forward scattering and the off-axis scattering were thus commonly used, meaning that the receiving optics was positioned opposite of the transmitting aperture for the forward scattering and in the case of off-axis scattering the receiver is looking at the measuring volume at an angle. The backscatter LDA has an advantage: the integration of transmitting and receiving optics in a common housing, saving the user a lot of time-consuming work aligning separate units. The forward scattering or the off-axis scattering are preferable, giving a higher data-rates comparing to the backscattering and they allow to collect a reasonable amount of data over a very short period of time.

In the present work a scattering angle of 25° was chosen for the case of non-reacting flow. Figure 2.8 shows a schematic of the laser layout for the dual-beam configuration.

Olive oil was chosen as particle of seed material for the non-reacting case (boiling temperature= 573.15 K, refractive index=1.4677) due to its good properties for LDA applications: good light scatterer, cheap, non-toxic, non-corrosive. An aerosol generator was used to seed the air with olive oil droplets that provided the LDA signal.

The measurements were carried out under two flow conditions,and the three velocity components (axial, radial and swirl) were measured separetely by one component Laser doppler anemometry (LDA). Figure 2.9 shows the collecting arrangement for the 1D-LDA for the non-reacting measurements.

The measurements in the reacting cases (non-premixed gaseous and spray) have been obtained using solid seeding (Titanium dioxide) by two component LDA in forward scattering mode. Figure 2.10 shows the collecting arrangement for the 2D-LDA during a spray reacting case measurements. Titanium dioxide (TiO_2) has a high melting temperature around 2116 K, and is readily available in small diameters (0.3 - 0.5 μm), which together with a high refractive index (2.5) is sufficiently large to scatter the incident laser light, but not too large to cause quenching effects on the flame.

For the spray case several measurements were also carried out without seeding the air, which therefore give the velocity of the droplets in the combustion chamber.

A Dantec Fibre Flow LDA system, with a Coherent innova series Ar-ion CW laser was used. The optical unit fitted with a single Bragg cell to give an optical frequency shift of 40 MHz, while the receiving optics comprised a 310 mm focal-length lens. The two laser beams were focused 8 mm above the inlet plane to avoid reflections from the base of the burner. The lowest data rates were about 2 kHz with the highest around 40 kHz. Variations in the data rate result directly from the nature of the flow field and the random arrival time of the seeding aerosol droplets [6]. Velocity measurements were made at several downstream positions. The transmitting and receiving optics were mounted onto a traverse system equipped with stepper motors that allowed the spatial translation in three directions with the accuracy of 0.1 mm. Radial traverses were taken in 2 mm increments from the centerline to as close to the wall as possible. About 200,000 samples were recorded at each measuring location. The measurements reported in this work showed single Doppler bursts and satisfied validation criteria (validation rate $> 80\%$). Table 2.3 shows the technical specifications of the LDV system used in the present work.

The BSA Flow Software was used for the data acquisition. The software is designed for use with Dantec Dynamics BSA F processors for Laser Doppler

Anemometry and BSA P processors for Particle Dynamics Analysis (PDA). It takes care of communication with hardware, acquisition of data or import of data and statistical processing of data. It controls the traverse and the set up for the traverse mesh.

In the present work, the complexity regarding these measurements were due to the confined flow by a square enclosure. It reflects and disperses the laser light in the near-wall regions and fouling of the windows by the flow seeding mandates regular cleaning of the glass, making the LDA measurements of an entire radial profile a slowly progressing work.

These measurements will be used to assist qualitative understanding of the blow-off data. Moreover, the flow velocity field measurements are desirable for two main reasons: (a) to characterize the velocity field for visualizing the possible recirculation zones and so to meaure them and (b) to facilitate any modelling efforts that will be undertaken, or have already been attempted of the blow-off phenomena.

2.3 Chemiluminescence measurements

Chemiluminescence in turbulent flames has been widely used in a variety of combustion applications due to its natural occurrence in the flame avoiding the use of external light sources. Moreover, it is an optical and therefore nonintrusive diagnostic [81]. In the present case an equivalence ratio close to the lean flammability limit can cause flame instabilities and flame blow-off. Chemiluminescence due to excited radicals (OH^*, CH^*, C_2^*, CO_2^* and others) can be related to some characteristics of the flame. OH* chemiluminescence gives reasonable information concerning the heat release rate and therefore, it can be used to determine the reaction front location [9].

Chemiluminescence measurements are much more convenient to apply since they do not require a costly laser pump source, but the main limit is that it cannot capture fine structures in flames, since the signal is integrated through the depth of the flame [88]. So the interpretation of chemiluminescence data can sometimes be ambiguous and that is why the extinction process is also examined on the burner axis by Planar Laser Induced Fluorescence (PLIF) [63].

Table 2.3: LDA operational parameters of the transmitting and the receiving optics.

Transmitting optics	
Wavelength (green)	514.5 nm
Wavelength (blue, only for 2D-LDA)	488 nm
Beam Diamter	2.2 mm
Power	0.7 W
Width of measurement volume	0.149 mm
Length of measurement volume	3.312 mm
Focal Length	310 mm
Beam Separation	44
Receiving optics	
Scattering angle (non-reacting case)	25°
Scattering angle (reacting case, forward mode)	0°
Focal Length	310 mm

The detection system was similar for both chemiluminescence and PLIF records. Similar diagnostic system was used in premixed flames close to blow-off by Kariuki et al. [53] and in two interacting premixed flames by Worth and Dawson [112]. It consisted of a LaVision IRO high-speed two-stage intensifier with a spectral range of 190 to 800 nm coupled to a Photron SA1.1 monochrome high speed CMOS camera with 1024 × 1024 pixel resolution up to 5.4 kHz, fitted with a UV bandpass filter (270-370 nm). The intensifier was gated at 190 μs at 5 kHz. The projected pixel resolution was $\approx$ 0.14 mm per pixel. The blow off dynamics were recorded by continuously triggering the imaging system and stopping the acquisition manually once the blow off has occurred [29].

As the chemiluminescence measurements are based on a line of sight integration technique, obtaining edge information of the flame brush is difficult. Due to the flame geometry of the present work, the OH* emission is an axisymmetric function which can be projected onto a plane using the forward Abel transform

to obtain the planar structure of the flame.

2.4 Planar Laser Induced Fluorescence measurements

Laser-based techniques are capable of remote, in-situ, spatially and temporally precise measurements of chemical parameters, but the main advantage is that they provide a non-intrusive measurement. The introduction of a physical probe will inevitably disturb the flow field, distorting the physiscs of the experiment.

Laser-induced fluorescence (LIF) is presumably the most well-known technique for radical species measurements. It has been in use considerably since the early 1980s because of its merits of providing high spatial resolution (typically 0.1 mm), high temporal resolution (typically less than 100 ns), and high sensitivity (typically concentrations in the ppm range) [26]. LIF is a sequence of molecules or atoms being excited to higher electronic energy states via laser absorption followed by spontaneous emission of fluorescence. It offers the possibility to investigate species of interest by selecting the appropriate wavelength. The planar laser-induced fluorescence (PLIF) is a derivative of the LIF technique, it involves illuminating the flow with a thin sheet of laser light tuned to excite electronic transitions in a chemical species in the flow. The fluorescence emitted by the laser excitation is focused onto an intensified charge-coupled device (ICCD) camera to produce an image of the fluorescence in that region. LIF-OH is a marker of the reaction zone so that a breakage in an otherwise continuous profile of OH is deemed to mark local extinction [26].

PLIF and LIF operate on essentially the same principles, with the difference being the way in which fluorescence signal is collected. In a LIF system, a photomultiplier can be used as a detector, whereas PLIF requires either a CCD or an intensified CCD (ICCD) camera or some other detector that provides two dimensional imaging [10].

PLIF is very sensitive to the particular species molecules being investigated, and their concentration, as the wavelengths and emission patterns, are highly specific for a particular species. Choosing the molecule to be investigated there-

fore depends on the ability of the specific molecule to give good insight into the objective of the experiment together with its spectroscopy, abundance and ease of excitation and detection of a fluorescence signal of a sufficient intensity[42]. The OH radical is commonly chosen in PLIF experiments for planar characterization of flames as it is a crucial species in most chemical models, is found in relatively high concentrations in flames, and has been well understood [42].

PLIF of OH was thus used in the present work to examine the flame structure of stable flames close to the blow-off limit and flames during the blow-off events. OH-PLIF was also used to observe the holes in the flame sheet and to estimate the lift-off of the non-premixed flames. A common problem with 2D imaging of events such the extinction is the ambiguity associated with motion into (or out of) the measurement plane. A local extinction event can be due to convective motion of an already extinct pocket into the measurement plane. So the interpretation of extinction events from 2D measurement technique has to be conducted with caution [44].

The quenching (or collisional quenching) rate is of primary importance to obtain an accurate LIF measurement. Quenching represents energy loss of the molecule by some pathways other than the fluorescence. The different possibilities include dissociation, collision with other molecules, ionization, chemical reaction, or transitions to unmonitored molecular energy states. To avoid errors introduced by unknown quenching rates generally saturated LIF is performed, which involves excitation with high intensity laser so that the quenching rate is small compared to absorption and stimulated emission rates. This also has the advantage of maximizing the fluorescence signal strength. A distinctive feature of planar LIF is that the imaging resolution is controlled not only by the camera and its associated collection optics but also by the laser beam optics. For instance, the thinner a laser beam is focused, the higher the resolution [8].

The OH-PLIF system consisted of a SIRAH Credo high speed dye laser, model 2400, pumped by a high-repetition rate diode solid state laser (532 nm), model JDSU Q201-HD, with a power of 14 W at 5 kHz and a pulse length of around 18 ns (Fig. 2.11). The tunable-dye laser produced a beam at 566 nm, which was then frequency doubled using a BBO crystal to produce a beam with an average power of 300 mW at 5 kHz (60 μJ/pulse). The frequency doubled output was

tuned near 283 nm to excite the $Q_1(6)$ line in the $A^1\Sigma$ - $X^2\Pi(1,0)$ band. The beam was then expanded into a sheet approximately 0.23 mm thick and of height 40 mm using various sheet optics. Imaging was performed using the same camera as for the OH* fitted with a Cerco 2178 UV lens (100F/2.8) and a UV bandpass filter (300-325 nm), with the intensifier gated at 400 ns at 5 kHz.The projected pixel resolution was $\approx$ 0.14 mm per pixel.

The OH-PLIF signal has been corrected in the following manner. During processing, each instantaneous image was initially filtered using a 2-D median non-linear filter for noise reduction (3 $\times$ 3 pixel filter size). The filtered images were then corrected for inhomogeneities in the laser sheet profile and the background was removed. The laser beam profile was Gaussian both before and after it passes through the sheet forming optics. Therefore to correct for the intensity variation, the recorded OH-PLIF intensity was integrated in the direction of the laser beam, producing a laser intensity distribution which varied with distance from the centreline. The closest Gaussian distribution was fitted to this profile in a least square sense. The fitted Gaussian intensity profile was then used to correct for laser sheet inhomogeneities.

The OH-PLIF was used to detect the flame front position in stable flames close to the blow-off limit and to image the extinction event. The repetition rate of OH-PLIF was sufficiently high (5 kHz) to capture the evolution of features that are relevant for this study such as extinction and re-ignition of reaction zones. The average images (1000) will be reported for each stable condions in Sections 4.5.3 and 5.4.3.

The turbulent flames considered in this work are three-dimensional in nature while the imaging is planar. This leads to two sources of uncertainties: (a) the potential of non-orthogonal slicing of the reaction zone which then yields artificially different OH profiles in the imaged plane, and (b) out-of-plane motion of structures which could then lead to erroneous interpretation of the OH images [50].

2.5 Mie scattering

To obtain insight into the flame a detailed investigation of the spray distribution is necessary from the practical and computational point of view. In the present work, a laser sheet is used to induce light scattering from the spray droplets. The laser-imaging system consisted of a high-repetition rate diode pumped solid state laser, model JDSU Q201-HD, with beam output at $\lambda = 532$ nm, focussed into a thin sheet of approximately 1 mm thick using sheet formation optics and used to light the seeded flow. Mie scattering of laser light from the droplets was collected using a Photron SA1.1 monochrome high speed CMOS camera with 1024×1024 pixel resolution up to 5.4 kHz.

Determination of the spray cone angle is performed by detecting the spray edges of the Mie scattered spray images (averaged of 1000 instantaneous shots).

2.6 Direct photography

Simple visualization of the turbulent flames before starting any detailed measurements (OH-PLIF, OH* chemiluminescence) have been conducted by direct photography and taking a film by a normal digital camera (30 Hz). They can provide a wealth of information and clearly much more that can be achieved by naked eye [20]. The change in the flame shape have been observed by taking several photographs with a digital SLR camera Nikon D3100. The camera has a lens AF-S NIKKOR 18-55mm f/3.5-5.6 and an image CMOS sensor with 14.2 million pixels. The exposure time (1/30 seconds) and the ISO sensitivity have been kept constant to compare the flames at different flow conditions.

2.7 Pollutants measurements

In several stable flames for the non-premixed and spray case close to the blow-off limit, emissions analysis has been performed. Simultaneous CO, NO_x, CO_2, O_2 and unburned hydrocarbons (UHCs) emissions have been measured.

The products exiting the burner are sampled through a water cooled probe. The sampling probe is placed at the combustor outlet to sample across the burner

at locations as indicated in Fig. 2.12. The probe was designed to aspirate the sample from the burner without disturbing the flow excessively by minimizing the probe's cross-sectional area. The sample is passed through a calcium chloride cartridge for water removal. The probe, illustrated in Fig. 2.13a, has been kept over 380 K to avoid water condensation, by using a heating cord wrapped around the probe. For each spatial location, the probe samples for two minutes to allow the readings to settle under steady state condition. Figure 2.13b shows a sectional view of the inside of the probe revealing the two internal tubes used to extract the sample and deliver H_2O to the head of the probe.

After the sample is aspirated through the probe, it travels through a 200 mm long heated stainless steel extraction tube maintained at a temperature of 380 K to ensure no condensation. This line leads to a Horiba EXSA-1500 automotive emission gas analyzer system. The analyser has been calibrated with 500 ppm CO, 204 ppm NO_2, 186 ppm NO, and 973 ppm propane. The measurable ranges and accuracy of the Horiba EXSA-1500 are given in Table 2.4. If the analyser calibration resulted in an offset from standard values for any of the flows, these offsets were accounted for in the resultant measurement.

Table 2.4: Horiba EXSA-1500 measurement ranges and accuracy. NDIR is the Non-Dispersive Infra-Red, a standard method of measuring the concentration of carbon oxides. The chemiluminescence (CLD) method measures the NO_x concentration, while the fast response FID measures the unburned hydrocarbons at the outlet.

Quantity	Measurement Technique	Range	Accuracy
CO	NDIR	0-5000 ppm	±1% FS
CO_2	NDIR	0-20 % vol	±1% FS
NO_x	CLD with NO_x converter	0-500 ppm	±1% FS
O_2	Magnetic single coil pressure type	0-25 % vol	±1% FS
UHC	FID heating type	0-10000	±1% FS

The primary particulate matter (PM) produced in non-premixed combustion is soot. Formation of soot can be considered an intrinsic property of most diffusion flames. The soot is formed in the rich regions of the flame, and wheter or not

soot is emitted from a flame depends upon competition between soot formation and soot oxidation processes [104]. There is no absolute standard method of PM measurement, and many different techniques are in general use. Two basic approaches are: (a) optical techniques, based on measurement of plume reflectance or of light transmission through the plume and (b) collection methods, which involve sampling and collection of smoke on a filter, with subsequent photmetric measuremnt of the degree of staining of the filter. To specify smoke concentrations the most common technique is to collect a large amount (more than 10 mg) of particulate matters on a filter, which is then weighed [61]. In the present work PM measurements have not been performed.

2.8 Duration of the blow-off event

The duration of the blow-off event was defined as the time the OH* chemiluminescence emission collected from the entire combustion zone decreased from 90% to 10% of the pre-extinction value during the decay to zero level. The method to reach the blow-off started from igniting a stable flame at condition far from blow-off. The fuel flow rate was then held constant, and the air flow rate was gradually increased in steps of approximately 2% (0.258 m/s) every 20 seconds until the blow-off occurred recording the blow-off velocity, U_{BO}, and the corresponding overall equivalence ratio, ϕ_{BO}. Reducing the step of the flow rate or increasing the time between two steps resulted in the same blow-off point within the experimental uncertainty.

2.9 Figures for chapter 2

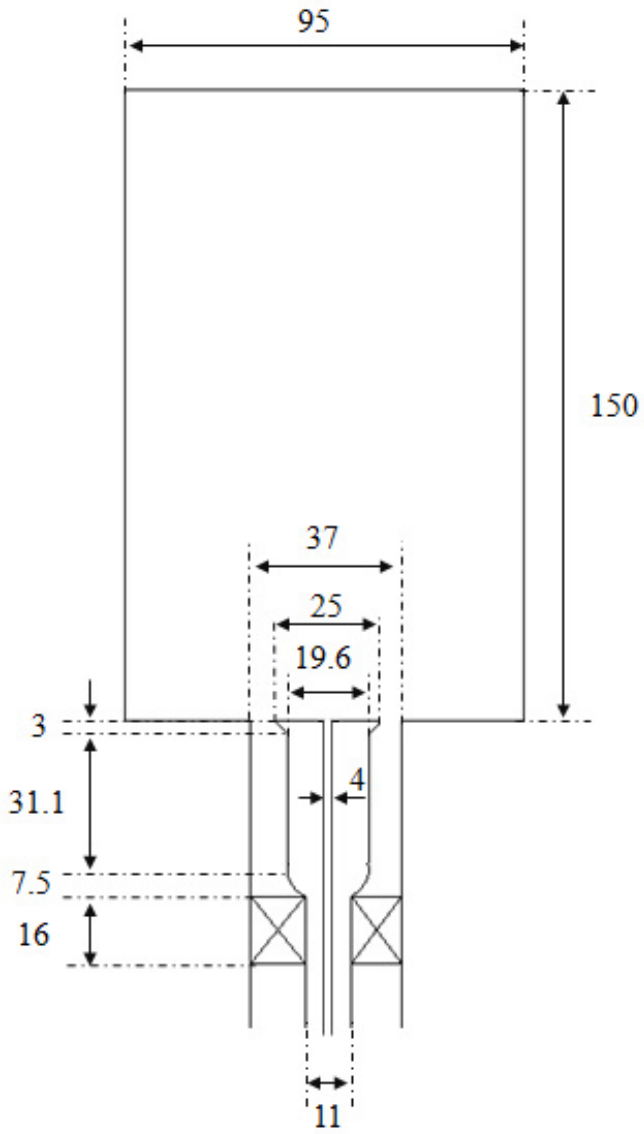

Figure 2.1: Schematic of the non-premixed configuration. All dimensions in mm.

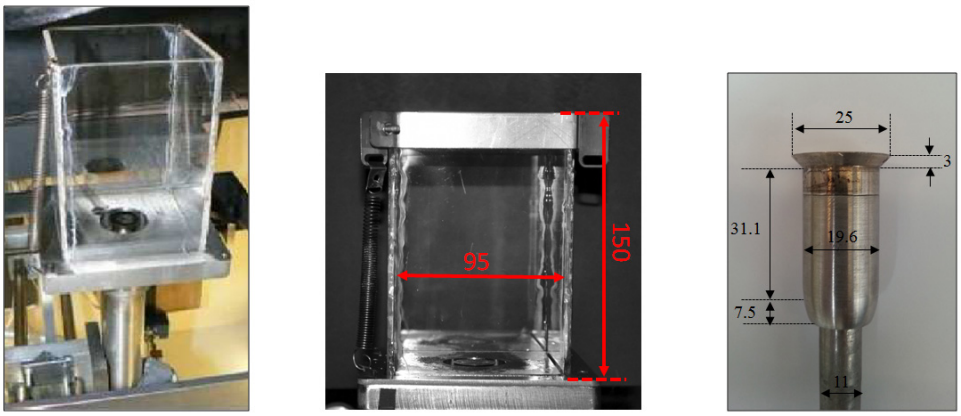

Figure 2.2: Image showing (a) a photograph of the combustor, (b) a photograph of the quartz enclosure and (c) a photograph of the bluff body without the swirler. All dimensions in mm.

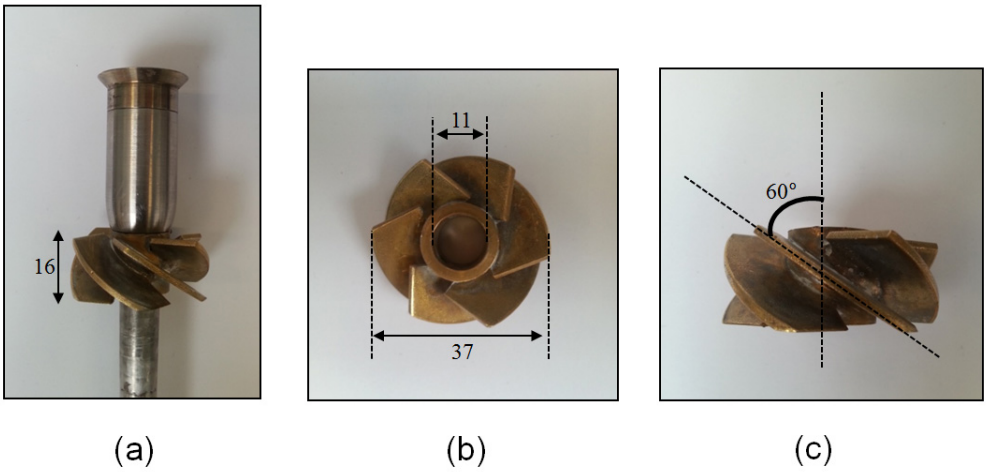

Figure 2.3: Image showing (a) photograph of the bluff body and the swirler (b) photograph from the top of the swirler and (c) a photograph of the swirler from a side view.

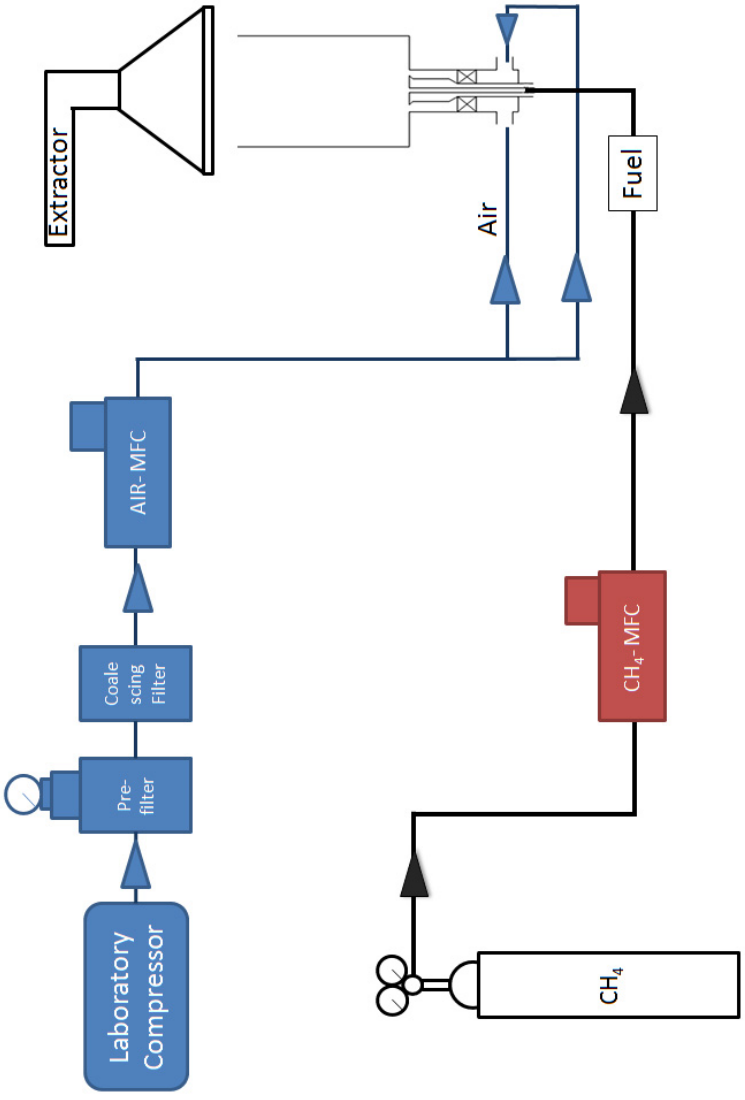

Figure 2.4: Experimental set up of the non-premixed configuration.

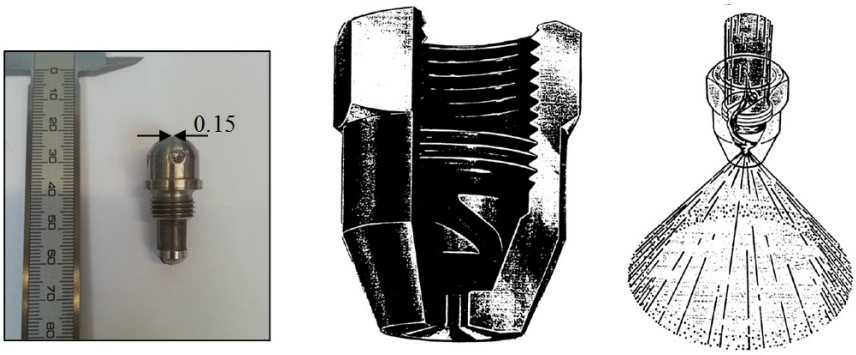

Figure 2.5: Image showing (a) a photograph of the pressure swirl atomizer used in the present work, (b) sketch of the pressure swirl atomizer with helical inlets provided by a conical insert and (c) sketch of the pressure swirl atomizer and the spray associated. Images (b) and (c) are from Lechler Company Nozzle Catalogue [1].

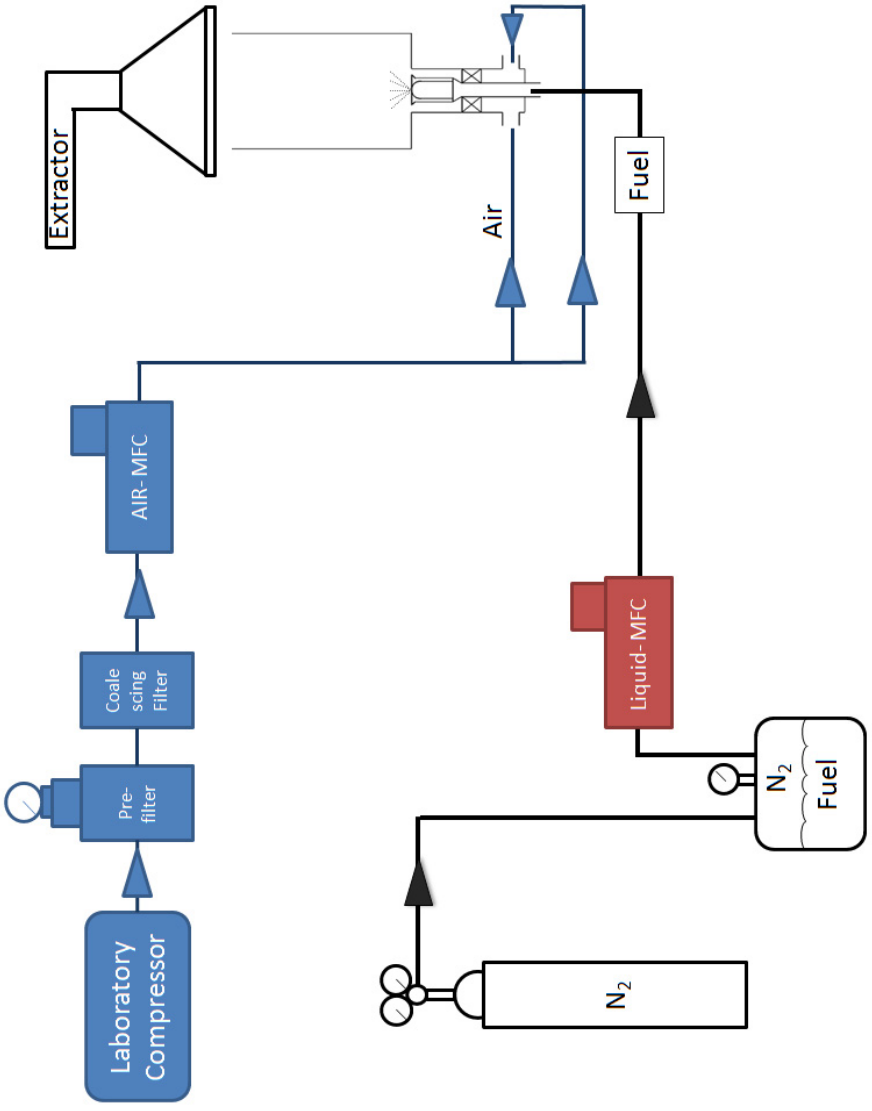

Figure 2.6: Experimental set up of the spray configuration.

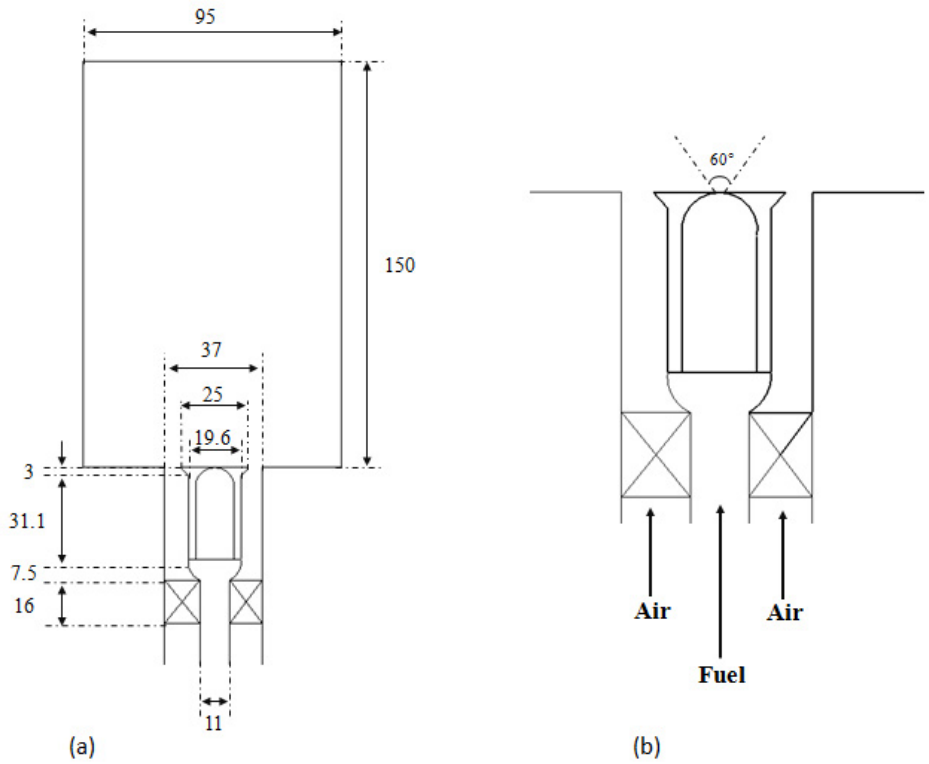

Figure 2.7: (a) Schematic of the spray burner and (b) detail of the bluff body. All dimensions in mm.

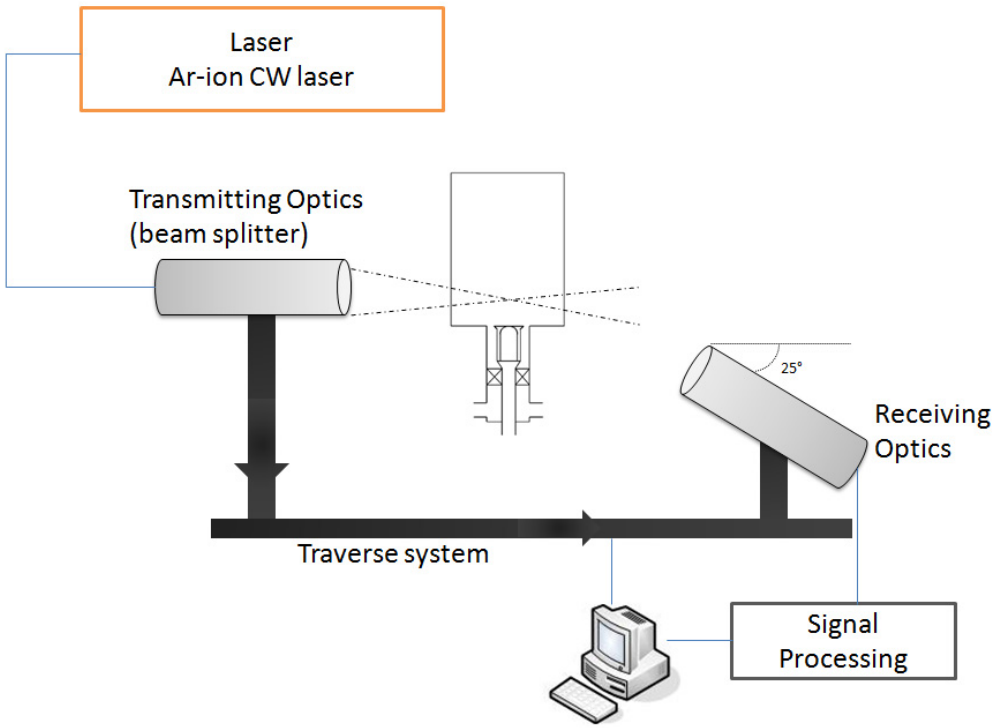

Figure 2.8: Schematic of the laser layout used for LDA measurements of the non-reacting case.

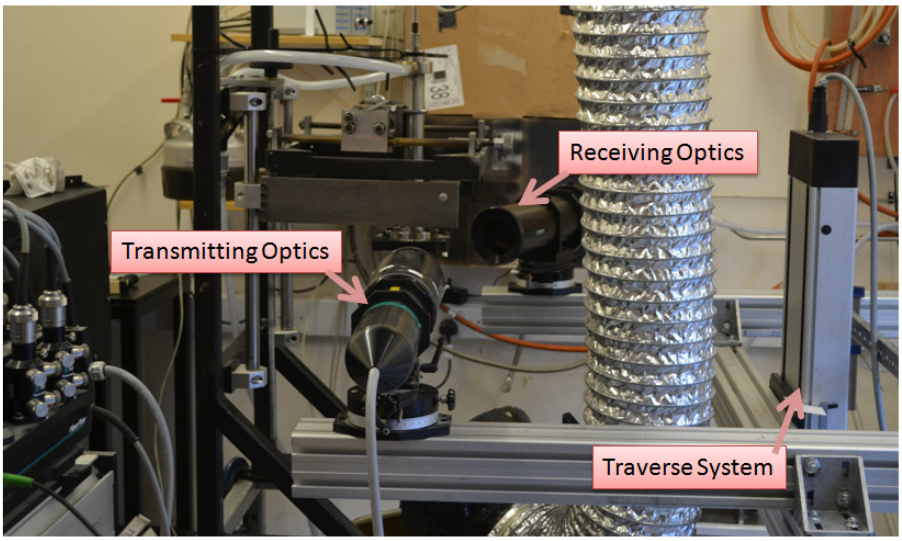

Figure 2.9: Photograph of the LDA setup.

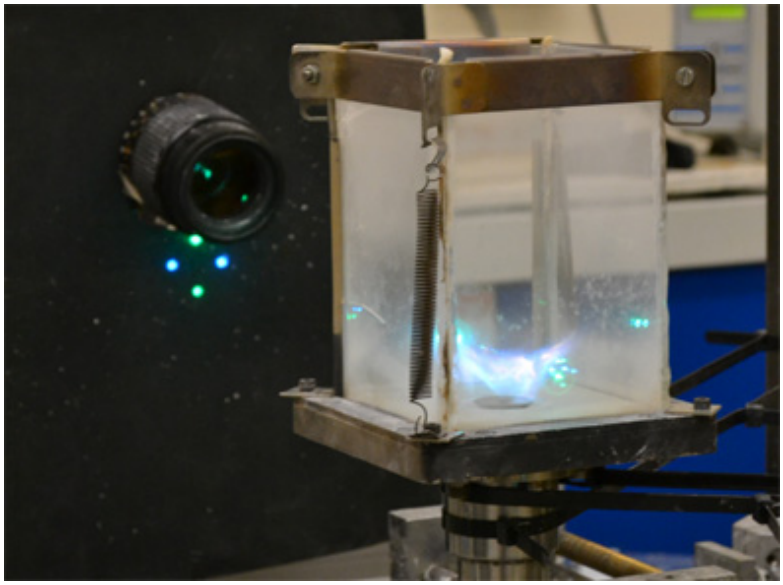

Figure 2.10: Photograph of the four beams and the collecting probe of the 2D-LDA setup during a spray reacting case measurement.

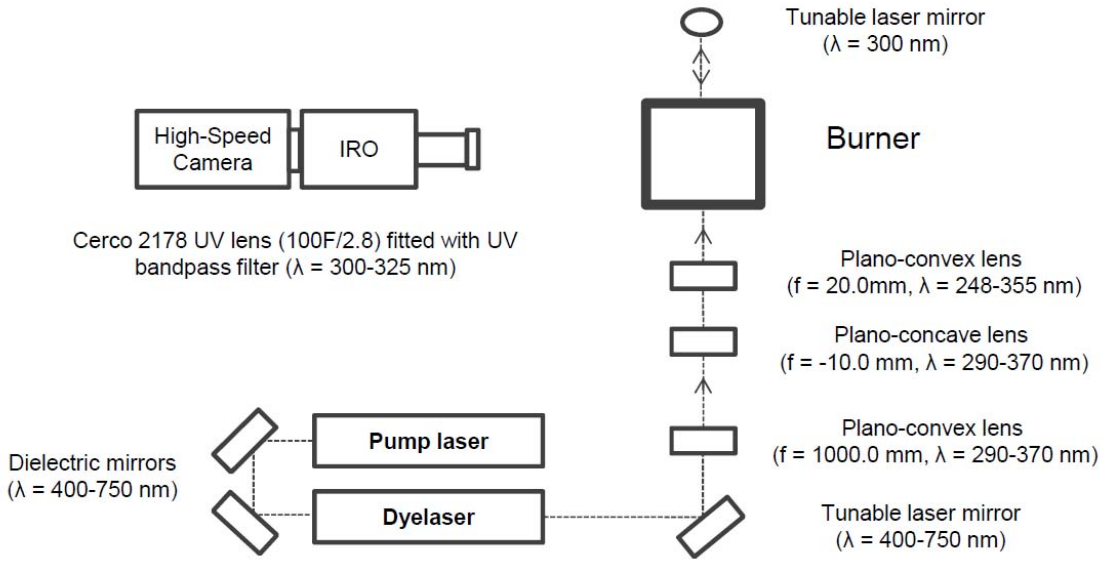

Figure 2.11: Schematic of the laser layout used for OH-PLIF imaging.

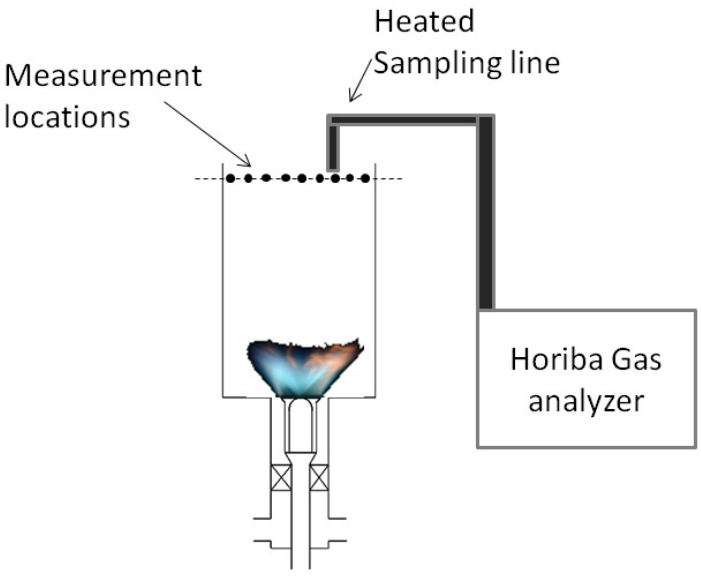

Figure 2.12: Schematic of the setup for emissions measurements.

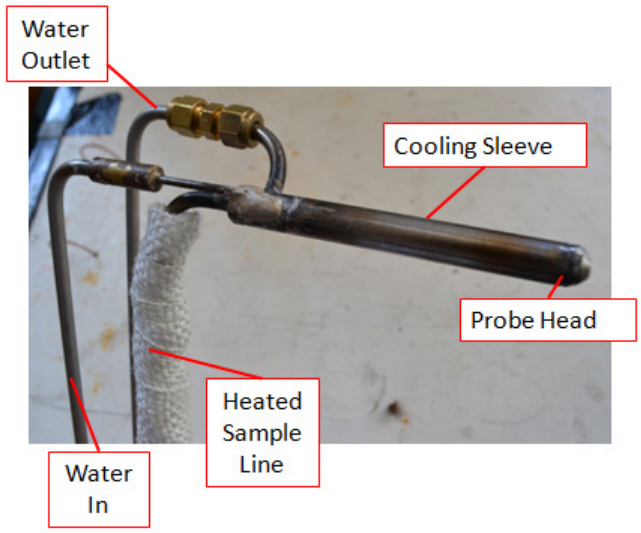

Figure 2.13: A photograph (a) and a dimensioned sketch (b) of the sampling probe used to collect the emissions.

Chapter 3

Velocity Field

This chapter presents some results of the velocity and turbulence in the combustion chamber, Fig. 2.2a. The first section reports the velocity field of two isothermal conditions obtained using 1D-LDA technique. Velocity fields for the non-premixed gaseous case and the spray case have been obtained by 2D-LDA measurements and they are shown in the section 3.2. The flow conditions of the non-reacting cases and the reacting cases are reported in Table 3.1. The main usefulness of the data in this chapter is to provide the aerodynamic flow pattern and some discussion on the velocity field and the related recirculation zones. These measurements are reproduced here to assist later data interpretation on the stabilization region and the blow-off events.

3.1 Isothermal conditions

Measurements of the axial, radial and tangential (swirl) velocity were obtained using the LDA technique described in section 2.2.3. The experimental set-up is described in Section 2.1. All measurements were taken without combustion and with only air at ambient conditions (1 atm, 288 K) and the measurements were carried out under two conditions, CSWH1 and CSWH3, Q=500 L/min and Q=650 L/min respectively. The volume flow rate divided by the annular passage area ($\pi(D^2 - d^2)/4$) gives the bulk velocity U_b and was equal to 14.3 m/s for CSWH1 condition and 18.5 m/s for CSWH3 condition. These give a

Reynolds number (dU_b/ν) equal to 23,000 for CSWH1 and 30,000 for CSWH3. By comparing the velocity at two different flow rates we can comment on whether the flow is at high enough Reynolds number to be Reynolds independent. In the following sections the mean axial velocity is reported as U and its r.m.s. as U'. The mean radial velocity is reported as V and V' the r.m.s.. The swirl velocity is reported as W and W' is the r.m.s..

Table 3.1: Test cases evaluated for the velocity field measurements. The fuel flow rate for the non-premixed gaseous case is 22 L/min and 0.12 g/s for the spray case.

Case	Name	Q_{air}[L/min]	U_{bulk} [m/s]
Non-reacting case	CSWH1	500	14.8
Non-reacting case	CSWH3	650	18.5
Non-premixed gaseous reacting case	F3A2	670	19.1
Spray reacting case	SWH1	500	14.8

3.1.1 Mean and RMS velocity

Radial profiles of the mean and r.m.s. of the axial, radial and swirl component are shown Fig. 3.1-3.4. The axial and the swirl components are measured for the whole width of the burner ($-1.2 < r/d < 1.8$) to show the symmetry of the flow, while the radial component was measured only for the right side of the burner, $0 < r/d < 1.8$. Some practical constraints limit the velocity measurements. First, the beam separation (44 mm) in conjunction with the focal length (310 mm) of the transmitting lens restrict the position of the LDA measuring volume (MV) within the square enclosure. Moreover, the glass windows reflect and disperse the laser light in the near-wall regions.

For a better visualization and comparison of the velocity profiles, the radial component is represented for the whole diameter, reproducing the data of the right side on the left side but changing the sign. In Fig. 3.1 the axial velocity profiles for CSWH1 and CSWH3 conditions at different heights (8-13-18-23-28-33-38-60-80 mm) are reported. The measurements made at various radial po-

sitions indicate an excellent degree of flow symmetry for both conditions. The highest axial velocities at z=8 mm are found at a radius between 12 and 20 mm corresponding to the annular inlet of air at the burner. The central area ($-0.5 < r/d < 0.5$ at z=8 mm) is characterized with low and negative axial velocity (Fig. 3.1a and 3.1c), the presence of a large recirculation zone (CRZ) is evident. It has a width approximately equal to $1.2d$ at z=8 mm and its width increases up to $2.2d$ at z=80 mm. The velocity measurements show that the recirculation zone is higher than the last measured height (length(CRZ)$> 4.7d$), as showed in Fig. 3.1b and 3.1d. The peak value of the axial velocity is approximately $1.2U_b$, while the minimum value inside the central recirculation zone is about of $-0.25U_b$. The zero-velocity surface is located at about r/d=$\pm$0.7 at z=8 mm and then it shifts to r/d=1.2 at about z=80 mm. The radial profiles of the root mean square velocity of the axial component, shown in Fig. 3.2, are consistent with the measured mean velocity profiles with maximum values arising in regions where the gradients in mean velocity are largest, so in the zone of the shear layer ($0.5 < r/d < 1.5$). When normalized by U_b, the mean and rms velocities are very similar for both values of U_b tested. This demonstrates that the flow is approximately Reynolds number independent and therefore insights gained here can be upscaled to realistic burners.

In Fig. 3.3, the radial velocity profiles show that as the distance from the centreline increases the radial velocity decreases at z=8 mm and then changes sign close to the wall. This indicates the presence of a side recirculation zone (SRZ). This small recirculation zone is formed close to the corner of the combustor which is induced by the sudden expansion of the flow.

The swirl velocity profiles reported in Fig. 3.4a and 3.4b show that the maximum velocity decreases with the radial position, but compared to the maximum of the axial velocity (Fig. 3.1), its position moves slower towards the walls. At the closest axial distance measured, the swirl velocity is of similar magnitude of the axial velocity, indicating the strong swirl nature of the flow. The radial profiles of the root mean square velocity of the swirl component, shown in Fig. 3.4c and 3.4d, are consistent with the measured mean velocity profiles with maximum values arising in regions where the gradients in mean velocity are largest. In Fig. 3.5 the comparison of all velocity components for the two flow conditions are

reported, the profiles have the same shape, only the amplitude is changed. Thus, various zones of the flow can be distinguished: the central recirculation zone, the side recirculation zone and the annular jet, which forms two shear layers with CRZ and SRZ; a schematic of the flow pattern and the recirculation zones is reported in Fig. 3.6. The clear identification of the two recirculation zones is important since both of them can assist in the flame stabilization of spray flames by entraining the smaller droplets and hot combustion species from the downstream region of the flame to the flame root.

The characteristic turbulent velocity is defined as:

$$q' = \sqrt{\frac{1}{2}(U'^2 + V'^2 + W'^2)} \tag{3.1}$$

where U', V' and W' are the root mean square of the axial, radial and swirl velocity respectively. Another definition of the characteristic turbulent velocity is:

$$q = \sqrt{\frac{1}{2}(U'^2 + 2W'^2)} \tag{3.2}$$

considering $W' = V'$. A comparison between these two definitions of the characteristic turbulent velocity is reported in Fig. 3.7 for both conditions, CSWH1 and CSWH3 along the right side ($0 < r/d < 2$). It is evident that to approximate $W' = V'$ does not show great discrepancies. The trend is the same for all conditions and for different stations (z=8 mm and 33 mm).

As expected from the r.m.s velocity data and reported in Fig. 3.8, the region of the maximum kinetic energy occurs in the shear region between the annular inlet flow and the central recirculation zone (already observed in the turbulent bluff-body flow by Schefer et al. [93]). This high value of q is directly related to the high shear generated by the velocity differences across these regions. Jones and Wilhelmi [49] observed the same behaviour in swirl combustor, the maximum level of turbulence prevail in the shear layer between the annular swirling jet and the recirculation zone, thus providing a zone of intense mixing in the case of non-premixed configurations.

3.1.2 Probability density functions

The probability density functions for axial, radial and swirl velocity were calculated from 200,000 measurements at different radial positions and different axial stations. Some results are presented in this chapter since they are characteristic of the distributions obtained in other regions of the flow. The distribution at r/d=0 corresponds at the centreline. The distribution at r/d=0.68-0.8 corresponds approximately to the shear layer separating the annular air flow from the central recirculation zone. Each distribution also present several statistical properties to provide a complete description of the distribution. These properties include the mean velocity, maximum velocity, standard deviation (i.e. the absolute variation of the data), skewness (i.e. lack of symmetry), and kurtosis (i.e. tendency of the distribution to have large peaks). Fig. 3.9a and 3.9b present the axial velocity distribution for z=8 mm at r/d=0 for CSWH1 and CSWH3 condition, respectively. Their velocity distribution is mono-modal and negative velocities are present due to CRZ near the centreline. The velocity distribution is positive and slightly skewed and the coefficient of kurtosis indicates that the distribution is somewhat peaked. The axial velocity distribution at z=8 mm and r/d=0.8, reported in Fig. 3.9c and 3.9d, is slightly skewed towards lower velocities for both flow conditions (CSWH1 and CSWH3), the distribution has a tail to the negative velocities and a relatively sharp drop-off at the highest velocities. The coefficient of kurtosis is lower that the centreline position, it indicates a more flat distribution. At z=33 mm and r/d=1.28(Fig. 3.10e-f) the velocity distributions are skewed towards higher velocities, they present a tail to high velocities and a sharp drop-off at the lowest velocities.

The probability distribution of radial velocity, shown in Fig. 3.11, exhibit a mean negative value at r/d=1.16 and z=8 mm, it is due to the presence of the SRZ close to corner. The swirl distribution velocities are reported in Fig. 3.12 and 3.13. They always show a uni-modal behaviour and they are slightly skewed in regions of high shear (r/d=0.68, z=8 mm). All velocity distributions are characterized as uni-modal. The results indicate that the form of the velocity distribution does not change significantly with the radial position. In Fig. 3.14 the axial velocity distributions for CSWH1 are reported for the left and the right

side of the burner ($r/d = \pm 0.8$ and ± 0.32) at two different heights: z=8 and 33 mm. In Fig. 3.15, the axial velocity distributions are reported for the same radial positions for the flow condition CSWH3. Observing the similar shapes and the similar properties (skewness, standard deviation and kurtosis), it is possible to note that the flow field shows a good level of symmetry for both flow conditions, confirming the results from the axial velocity profiles (Fig. 3.1).

3.2 Reacting cases

Measurements of the axial and tangential (swirl) velocity were obtained using the 2D-LDA technique described in section 2.2.3. All measurements were performed with air at ambient conditions (1 atm, 288 K). Two reacting cases were studied: non-premixed gaseous case and the spray case. Reaction can have a strong impact on the flow field structure. It could result in an enhanced rate of back mixing, and a shorther and wider zone of recirculation [17; 49].

3.2.1 Non-premixed gaseous flames

In the non-premixed gaseous case the measurements were carried out under a stable flow condition, F3A2 (Q_{air}=670 L/min and Q_{fuel}=22 L/min). The volume flow rate divided by the annular passage area ($\pi(D^2 - d^2)/4$) gives the bulk velocity U_b and was equal to 19.1 m/s. The mean axial velocity is reported as U and its r.m.s. as U'. The swirl velocity is reported as W and W' is the r.m.s.. The experimental set-up is described in Section 2.1.1. Radial profiles of the mean and r.m.s. of the axial and swirl component are shown Fig. 3.16. The axial and the swirl components are measured for the whole width of the burner ($-1.5 < r/d < 1.5$) to show the good symmetry of the flow.

In Fig. 3.16a the axial velocity profiles at different heights (10-15-55-110 mm) are reported. The measurements made at various radial positions indicate an excellent degree of flow symmetry. The highest axial velocities at z=10 mm are found at a radius between 12 and 20 mm corresponding to the annular inlet of air at the burner. The central area ($-0.5 < r/d < 0.5$ at z=10 mm) is characterized by an high axial velocity due to the fuel penetrating into the central recirculation

zone, while low and negative axial velocity are observed at an height of 110 mm and so confirming the presence of a central recirculation zone. The peak value of the axial velocity is approximately $1.2U_b$, while the minimum value inside the central recirculation zone is about of $-0.2U_b$. The radial profiles of the root mean square velocity of the axial component, shown in Fig. 3.16c, are consistent with the measured mean velocity profiles with maximum values arising in regions where the gradients in mean velocity are largest, so in the zone of the shear layer ($0.5 < r/d < 1$) and in the zone of the fuel penetration ($-0.3 < r/d < 0.3$).

The swirl velocity profiles reported in Fig. 3.16b show that the maximum velocity is at a height of 10 mm in the shear layer area ($0.5 < r/d < 1.2$). It decreases with the radial position and then changes sign close to the wall, indicating the presence of a side recirculation zone (SRZ) as observed for the previous non-reacting case. This small recirculation zone is formed close to the corner of the combustor which is induced by the sudden expansion of the flow.

The radial profiles of the root mean square velocity of the swirl component, shown in Fig. 3.16d are consistent with the measured mean velocity profiles with maximum values arising in regions where the gradients in mean velocity are largest.

Thus, various zones of the flow can be distinguished: the fuel penetration zone at a height lower than 110 mm, the central recirculation zone at 110 mm, the side recirculation zone and the annular jet, which forms two shear layers with CRZ and SRZ. The clear identification of the two recirculation zones is important since both of them can assist in the flame stabilization by entraining the hot combustion species from the downstream region of the flame to the flame root. The fact that along the centreline the velocity is positive in the beginning (fuel jet) but then becomes negative, indicates a flow qualitatively different than the Sydney swirl flames [28] that show a positive axial velocity always along the axis. The short flames observed here (Section 4.5.3) is consistent with the fact that the fuel jet eventually stagnates against the opposing recirculating flow.

Spectra of the instantaneous velocity have been done to determine any peaks and their evolution. Spectral processing was carried out by re-sampling the velocity data into a continuous time series based on the average data rate for each position. The average data rate was calculated by dividing the number of samples,

which was about 2,000, by the sample period. Using the axial and swirl velocity measurements discussed earlier in this section, timeseries of the fluctuations of the axial and swirl velocity at various radial locations were used to evaluate the power spectral density (PSD). They are reported in Fig 3.17, 3.18 and 3.19. In each graph a dashed straight line with equation $y = x^{-5/3}$ is reported for comparison with the characteristics of "Kolmogorov turbulence". In fact power spectral density for a temporal-dependent signal is defined as the Fourier transform of the temporal autocorrelation (at the same spatial point). Power can be actual power, but, more often, is referred to a squared timevarying signal. Therefore, when the signal is a velocity component it refers to a kinetic energy. On the other side the energy spectrum in turbulence is defined as the Fourier transform of the covariance of simultaneous velocity fluctuations measured in two different points. Therefore, power spectral density and energy spectral density refer to frequency (reciprocal of time) or to wavenumber (reciprocal of length). Under the Taylor hypothesis for which the turbulent fluid dynamic structure are all transported by the local average velocity, frequency can be linearly scaled with wave number. In this case, spectra derived by spatial varying velocity components can be compared directly with those obtained on the frequency dominion.

This is relevant for the insert of the -5/3 dashed line reported in Fig 3.17- 3.19. In fact the energy spectrum for turbulent velocity component fluctuations derived by Kolmogorov in the wave number of equilibrium subrange (large scales, which are not affected by viscosity) follow a drop off law with power exponent -5/3. The comparison of the power density spectrum obtained by the measurements is therefore significant in the assessment of the possible Kolmogorov-type behaviour of the fluctuating component recorded in the present swirled flow.

In Fig. 3.17 the power spectrum for the axial and tangential velocity components at z=15 mm and r/d=0 is shown. It is evident that the power spectrum of both components on the centerline cover only one frequency decade in the range 10-100 Hertz. The spectrum is quite regularly continuous with very faint relative maxima. This means that there is not very dominant fluid-dynamic oscillations locked to a single axial vortex shedding or a single tangential vortex precession. The intermittent structure outlined by means of the fluctuating components of the velocity cannot be linked to a quasi-periodic oscillation, but they change

their frequency even if this occurs in a relatively narrow frequency range (only one decade), in the same frequency range and at relatively low level of frequency never higher than hundreds Hertz.

A different picture come from the spectra on the flow periphery at r/D =0.72 (Fig. 3.18). They pertain to spectra families which are typical of turbulent flows. In fact the spectra on both velocity components are quite shifted toward very high frequency level in the range of kHz and allow to interpolate a quite representative line in the log plots with a definite slope. In fact there are no significant relative maxima and they extend to a relatively broad range that cover up to three order of magnitude of frequency values.

The most interesting feature is the spectrum slope, which can be drawn from the comparison of the spectra slope with that of the dashed line reported on right side of the spectra. In fact in the two figures here described as well as in all the others the straight line has been drawn with the same slope, i.e. 5/3. Differently from the two spectra shown before, in this case the spectra better parallel the straight line. Therefore, all the features related to such type of slopes in terms of Kolmogorov type cascade model can be inferred with high accuracy level.

Profiles of the spectra at a further station (z=110 mm), reported in Fig. 3.19, confirm the trend of the previous graphs. It is very likely that the extension of the spectra (more than two decades) and the similarity between the two spectra for the two components leads to conclude that in this case the spectra are representative of the Kolmogorov type of turbulence model.

3.2.2 Spray flames

For the spray reacting case the experimental set-up is described in Section 2.1.2. Two different 2D-LDA measurements were perfomed:

1. Droplet velocity: The velocity measurements have been recorded only for the droplets injected from the pressure-swirl atomizer. No solid seeding has been added to the air.

2. Air velocity field: Solid Seeding have been added to the air inlet and thus the measurements represents the flow of air within the combustion chamber. The velocity profiles close to the liquid injector ($-0.5 < r/d < 0.5$)

have been reported in this section, but they have to be treated carefully, since in this area the simultaneous presence of the solid seeding and the heptane droplets does not allow a realiable interpretation of the measurements, since the LDA picks up signal from both the spray and the seeded air. The measurements (1) unambiguously refer to the droplet velocity; the measurements (2) unambiguously refer to the true air velocity only in regions where droplets do not exist (z >40 mm) or where droplets fully follow the air.

Radial profiles of the mean and r.m.s. of the axial droplet and swirl droplet component are shown in Fig. 3.20.

The axial and the swirl components for the droplet velocity field are measured for a narrow radial profile ($-1 < r/d < 1$). Only in this area the droplets are not yet evaporated and thus the LDA signal is high enough to collect a high number of samples (over 2000) and to have a high data rate (over 1kHz). Further downstream than about z=40 mm, no LDA signal was detected with unseeded air, indicating complete evaporation.

In Fig. 3.20a the axial velocity profiles of the droplets for SWH1 condition at three different heights (10-18-30 mm) are reported. The measurements made at various radial positions indicate an excellent degree of symmetry of the spray injection. Two peaks are observed close to the centre due to the hollow cone spray.

The highest axial velocities at z=10 mm are found at a radius between 12 and 20 mm corresponding to the annular inlet of air at the burner. The peak value of the axial droplet velocity is approximately U_b, while the minimum value is about of $0.2U_b$. The radial profiles of the root mean square velocity of the axial component, shown in Fig. 3.20c, are consistent with the measured mean velocity profiles with maximum values arising in regions where the gradients in mean velocity are largest, so in the zone of the shear layer ($-1.2 < r/d < 0.7$).

The swirl velocity profiles reported in Fig. 3.20b show the maximum velocity at r/d=$\pm$0.8 where the droplets meet the annular air injection. Note the relatively small swirl velocity inside the CRZ.

The radial profiles of the root mean square velocity of the swirl component, shown in Fig. 3.20d, are consistent with the measured mean velocity profiles

with maximum values arising in regions where the gradients in mean velocity are largest.

Thus, various zones of the flow can be distinguished: the central fuel injection and the annular jet. The clear identification of the droplet velocity field is important since it affects the flame shape.

It is of great interest to compare the measurements of the droplet velocities with the air velocity. Therefore the set of measurements just described can be directly compared with the set which is reported in Fig. 3.21, since they refer to the same case named according to our classification as SWH1. They are in sequence the mean axial velocity profiles (a), mean swirl velocity profiles (b), r.m.s of the axial velocity (c), r.m.s. of the swirl velocity (c). All profiles are normalized with the average bulk velocity (U_b).

In Fig. 3.21a the radial profile at 10 mm from the nozzle outlet of the axial velocity component is overlapping the corresponding one for the droplet velocity in Fig. 3.20a only in the peripheral part for radial distance from the centreline higher than 0.6 r/d. This implies that at the high velocity regions the droplet velocities and the air velocities are the same, i.e. the droplets are completely captured by the air and move as the seeding (TiO_2) particles.

This is also consistent with the velocity profiles at 15 mm and 20 mm. In fact the axial velocity peaks shift along the radius according to the expected swirl jet aperture. This similar agreement between droplet and air measurements is not repeated in the central part of reacting flow. The *air* velocities at 10 mm and 15 mm, reported in Fig.3.21a inside the dashed black line are quite different from the droplet velocity profiles at 10 mm and 15 mm of Fig. 3.20a. The air velocities are negative in the first case, where they are always positive for the droplet velocity. This is also consistent with expected spray behaviour. Inside the early part of the spray the larger droplet keep their momentum and follow the conical trajectory either in the quiescent or flowing condition. On the opposite the small particles follow the negative velocity reverse flow in the centre.

It is worthwhile to stress that this is the first evidence of the reverse flow occurrence also inside the early spray zone. The relevance of such observation has to be related to the reverse flow has to be composed mainly of high temperature products and this, in turn, infers that chemical reactions of the evaporated spray

can take place also in the centre early part of the combustion chamber.

There is no direct comparison of the particle and droplet velocities for stations higher than 30 mm, because in the reacting case the evaporation is completed before this height. Nevertheless the gas velocities are very interesting to be compared with the isothermal pattern in the central part of the reactor where optical signals could be detected. In this region profiles pertaining to a distance higher than 55 mm are quite similar. They are all negative for r/d=0.5 and recover positive values in the wider peripheral zone. The similarity of the velocity profiles in this far region is quite striking. There is a combined effect of the expanded reacting gas which reversely flows along the central part and which pushes the direct flow on the wall and the relatively narrow distance between the confine walls, which prevent the direct flow to enlarge indefinitely.

Comparing the velocity component of the reacting case (Fig. 3.21a) and the isothermal case (Fig. 3.1a), we can also note that the central recirculation zone is quite wider for the reacting flow case.

The description of the swirl velocity profiles of Fig. 3.21b is more straightforward. The first three profiles in the early part show the marked absolute maxima well inside the swirling widening flow, correlated well with the positions of the axial maxima of Fig. 3.21a. Nevertheless they are the only peaks. The central-region axial velocity peaks of Fig. 3.21a are not present in these three swirling profiles therefore they are correlated with the axial spray entrainment either they refer to trace particle or to small droplets.

The root mean square of the axial velocity depicted in Fig. 3.20c can be classified, as general trend, similarly to those shown in Fig. 3.20a . The profile at z=10 mm shows three peaks of comparable intensities at the same position as for the mean axial velocity. Their maxima range between 0.25 (the central one) and 0.35 (the external ones). It is interesting to note that the central peak fluctuation value is very similar to the central maximum of the average axial velocity. As matter of fact the ratio between the two is approximately 0.7-0.8.

On the opposite the profiles at z=18 mm and 30 mm have similar behaviour and nearly the same level of intensity. In fact the difference in values between the two profiles in the central part is less than 10%. Furthermore their values are also quite similar to the values of the average axial velocity also with some

outstanding values of the fluctuation at z= 30 mm higher than the corresponding average values.

In Fig. 3.20d the detected azimuthal fluctuations is reported. The fluctuation profile parallels the average velocity profile ranging inside the same value interval. The main difference with axial velocity behaviour is the relatively wide central region with low intensity values for both (average and fluctuating components). This is an unexpected feature because of the presence of the annulus with high tangential velocities according to the generation of the droplets from a droplet conical swirled liquid sheet, but also consistent with the external swirled flow. In other words the peripheral swirled two phase flow is not able to entrain in the same vortical structure the central cloud. This is also more striking feature if the swirled components are compared to the axial ones. In fact, as it has just been commented, the axial fluctuations are relatively high, even higher than the average ones, so that the flow structure from z= 30 mm is not vortical.

More complex structure can be inferred from the analysis of the gaseous flow pattern. The axial component reported in Fig. 3.21c and the swirl component reported in Fig. 3.21d, similarly to the droplet velocity patterns, parallel the corresponding velocity profiles and have similar values. The external maxima of the fluctuations at z=10 mm, reported in Fig. 3.21c, are placed in correspondence of the maxima of the average velocity gradient, characteristic of shear layer turbulence.

The set of the profiles of Fig. 3.21c can be classified in two sets as the average axial velocities. The first one relative to the double swirled structure is present in the profiles at z=10 mm and 15 mm. Namely the swirled gaseous one on the periphery and the spray induced flow in the central part. The second one relative to profiles from 40 mm to 110 mm which are quite similar also in terms of values. This in turn means that the decrease of the corresponding axial negative velocity makes the relative percentage higher and higher up to the station at 110 mm where the fluctuations are higher than the average negative velocity, supporting a positive/negative alternation of values. In this respect this section could be considered the first one where it is possible to observe fluctuations representative of the break-down zone.

Also for the tangential velocity fluctuation reported in Fig. 3.21d the profiles can be classified in two sets (up to 20 mm and 40-110 mm). Also in this case the first can be correlated to the double swirl structure and the second to the recirculation zone. Also in this case there is a signature of the swirl break-down around z=110 mm, which is even more clear than that detected for the axial velocity fluctuation. In fact the region where the fluctuations are much higher than the average values is more extended down to 80 mm and the ratio between the fluctuation versus average components is also much higher than in the case of the axial component.

Two different velocity measurement sets are compared in Fig. 3.22, relative to flow condition SWH1 in spray reacting regime. They are droplet velocity measurements without seeding and the measurements obtained by seeding the air with TiO_2. In Fig. 3.22a the axial component of the velocities are reported, whereas in Fig. 3.22b the tangential components are shown. The profiles have been also separately commented previously, therefore the only additional comments strictly pertain to their comparison. The profiles are nearly coincident along the whole radial range. This means that the spray is in fluid-dynamic equilibrium with the air pattern, in the sense that there is no significant velocity slip between the air and the droplets at least for regions higher than 10 mm from the nozzle. Both profiles have an excellent degree of symmetry of the flow. The two peaks of the axial velocity at $r/d = \pm 1$ have the same value (Fig. 3.22a). The droplets captured in the main swirling flow are entrained just at the air velocity. The only difference consists in the axial component profiles in the region inside the spray (within the CRZ). A similar trend but different values of the mean axial velocity profiles are evident where the spray injection is located. As matter of fact the droplets of the spray in central part, less than 5 mm from the central axis, proceed in the forward direction also at velocity comparable to the bulk velocity (their ratio is higher than 0.4), whereas the velocity of the condensed phase particles which include also the tracer shows a negative velocity minimum. This means that the droplets with their high level of inertia are able to face with opposite negative velocity inside the recirculation zone.

Spectra of the instantaneous velocity have been done to determine any peaks and their evolution for the velocity measurements obtained by seeding the air.

As for the non-premixed gaseous case, spectral processing was carried out by re-sampling the velocity data into a continuous time series based on the average data rate for each position. The average data rate was calculated by dividing the number of samples, which was about 2,000, by the sample period. The spectra at two different stations are shown in Fig. 3.23 and 3.24.

In Fig. 3.23 the power spectrum for the axial and tangential velocity components at z=10 mm and r/d=0.8 is shown. The power spectrum of both components covers only one frequency decade in the range 10-100 Hertz. As for the non-premixed gaseous case the spectrum is quite continuous without any relevant maximum.

The spectra on the flow periphery at r/d =1.12 and at z=20 mm (Fig. 3.24) are typical of turbulent flows. They are quite shifted toward very high frequency level in the range of kHz. There are no significant relative maxima and they extend to a relatively broad range that cover up to three order of magnitude of frequency values. Similarly to the non-premixed gaseous case, a region with the typical slope of -5/3 is evident in both figures. This smooth decay indicates a developed turbulence.

3.3 Conclusions

The velocity fields have been characterised using the LDA technique for two flow conditions in a non-reacting flow, for one flow condition for the non-premixed gaseous case, and for one flow condition for the spray case. Measurements of the axial, radial and swirl velocity at different radial locations are presented.

In the non-reacting case close to the inlet plane the velocity profiles of all three components show sharp peaks which move rapidly towards the walls with increasing downstream distance. This is the typical behaviour for swirl combustors as described in [49]. A central recirculation zone has been observed with a maximum width of 2.2d (d is the diameter of the bluff body). The velocity profiles indicated the presence of a side recirculation zone close to the corner of the combustion chamber which is induced by the sudden expansion of the flow. The clear identification of these recirculation zones is important since they can assist the stabilization of the flame.

The axial and the swirl velocities have been measured by 2D-LDA for two reacting cases: non-premixed gaseous case and the spray case.

In the non-premixed gaseous case the velocity profiles showed a very good symmetry of the flow. The central area of the combustor is characterized by a high axial velocity due to the fuel jet penetrating into the central recirculation zone, but eventually stagnating, while low and negative axial velocities are observed at a distance of 110 mm from the bluff body. The root mean square velocity of the axial component is consistent with the measured mean velocity profiles with maximum values arising in the regions where the gradients in mean velocity are largest (the shear layer zone and the fuel penetration zone). The velocity profiles for this reacting case confirms the presence of a side recirculation zone.

For the spray reacting case two different velocity measurements have been presented: (a) the droplet velocity measurements close to the bluff body (no seeding in the air) and (b) the velocity field of the whole combustion chamber obtained by seeding the air. The velocity droplet profiles indicate an excellent degree of symmetry of the flow. Two peaks of the axial droplet velocity are observed close to the centre of the fuel injection due to the hollow cone spray shape. The swirl droplet velocity profiles show a maximum value where the droplets meet the annular air injection. The clear identification of the droplet velocity field close to the bluff body is important since it affects the flame shape.

For the second set of measurements (case b), the axial velocity peaks shift along the radius according to the expected swirl jet aperture. The air and the droplet measurements are different in the central part of the reacting flow close to the fuel spray injection. There is no direct comparison of the two measurements for station higher than 30 mm due to the complete droplet evaporation. It is important to observe that the central recirculation zone observed for the spray reacting case is quite wider than the corresponding non-reacting case. The non-premixed gaseous case also showed a wider recirculation zone that the cold case. The swirl air velocity profiles are consistent with the typical pattern structure of swirled confined configurations. A description of the root mean square velocity profiles has also been provided.

The velocity and turbulence information obtained are particularly useful for providing data on the velocity field, which is crucial for validation of computa-

tional models.

3.4 Figures for chapter 3

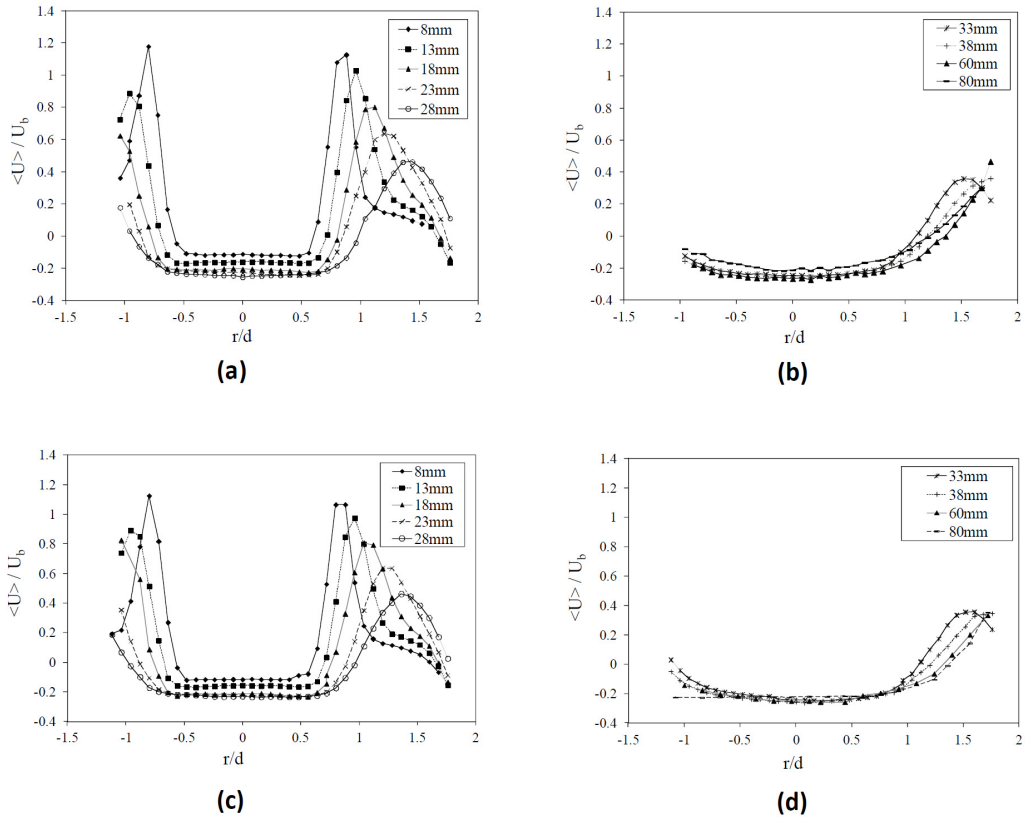

Figure 3.1: Mean axial velocity profiles normalized with the bulk velocity for flow condition CSWH1 (a-b) and condition CSWH3 (c-d).

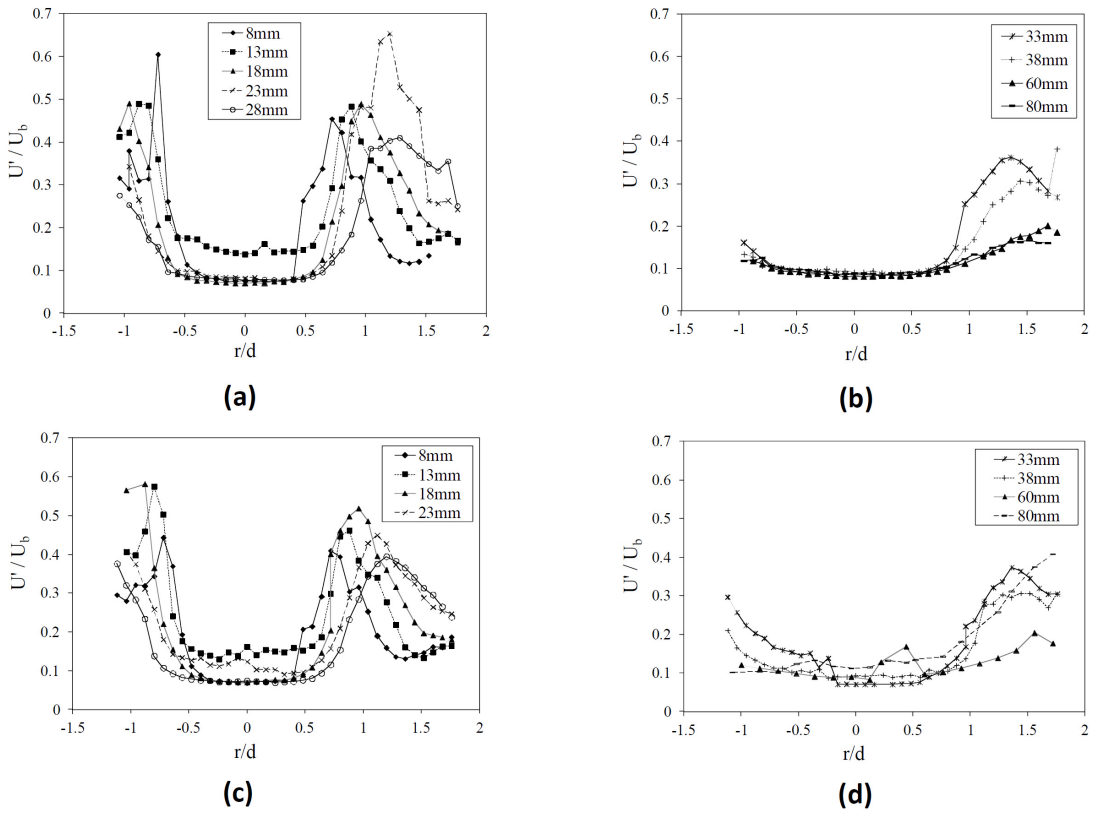

Figure 3.2: R.m.s of the axial velocity at flow condition CSWH1 (a-b) and at condition CSWH3 (c-d).

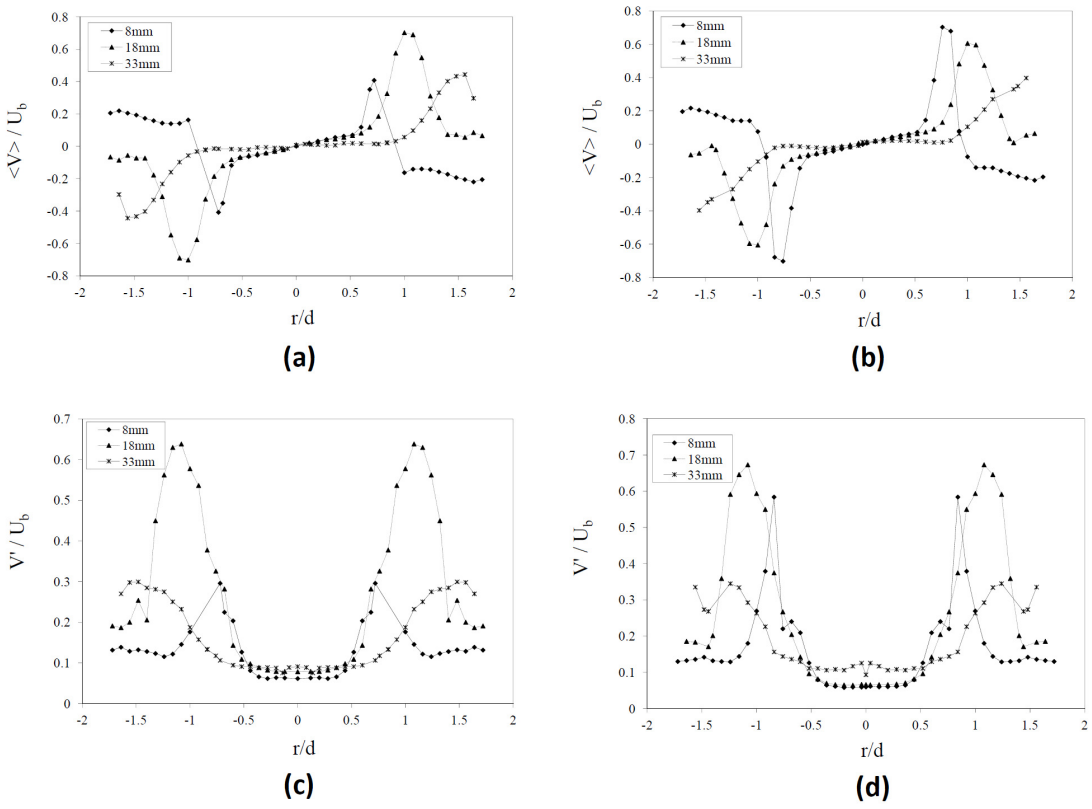

Figure 3.3: Mean radial velocity profiles for condition (a) CSWH1 and (b) CSWH3. R.m.s radial profiles for the condition (c) CSWH1 and (d) CSWH3.

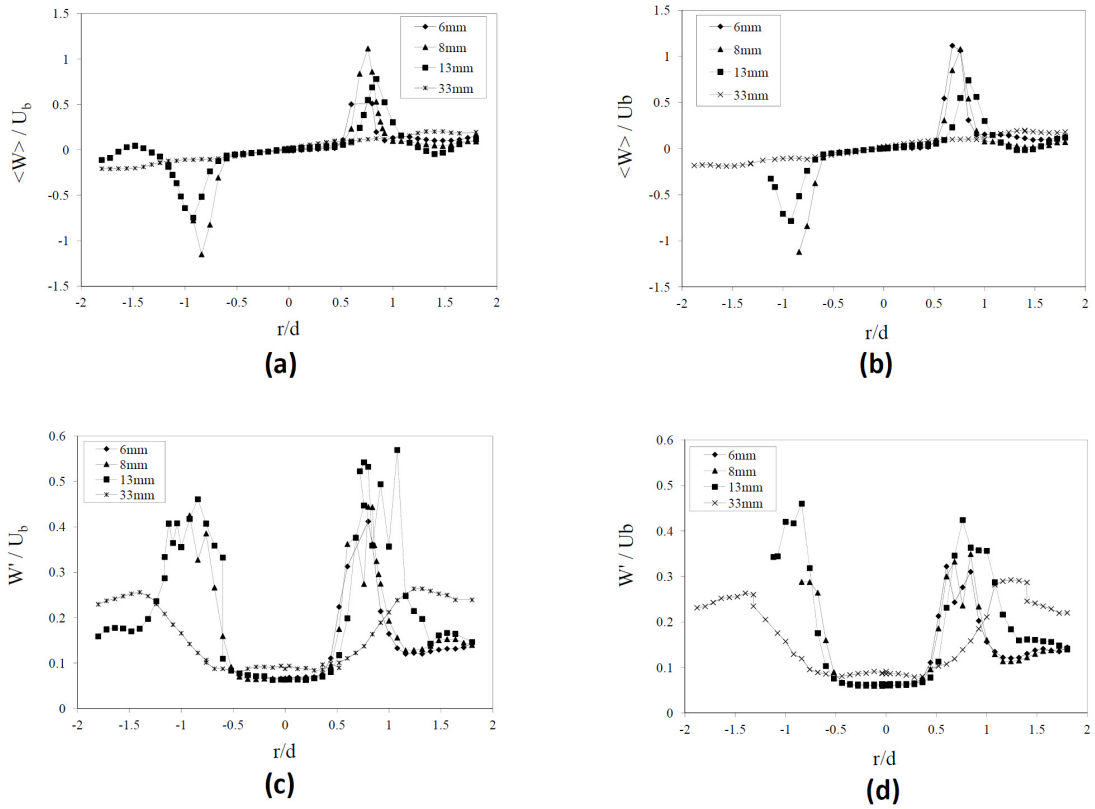

Figure 3.4: Mean swirl velocity profiles for condition (a) CSWH1 and (b) CSWH3. R.m.s swirl profiles for condition (c) CSWH1 and (d) CSWH3.

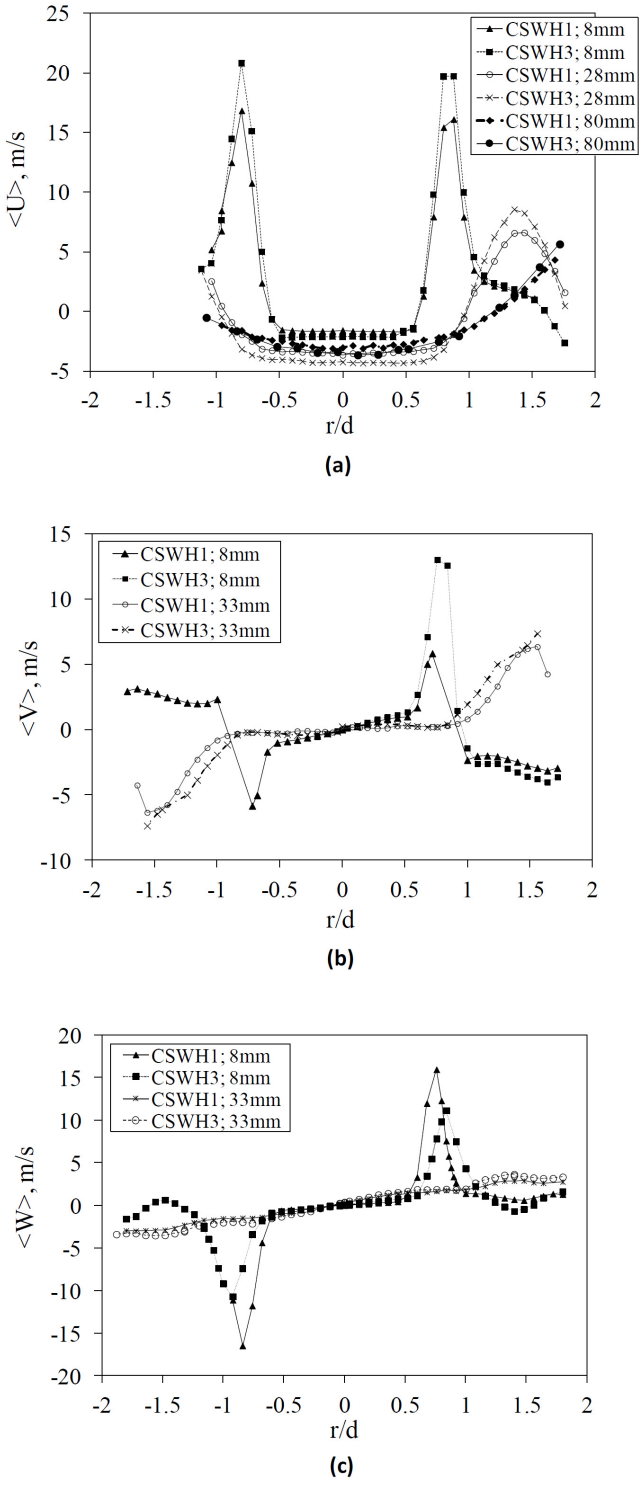

Figure 3.5: Comparison of (a) the mean axial velocity profiles, (b) the mean radial velocity profiles and the (c) the mean swirl velocity profiles for two flow conditions: CSWH1 and CSWH3.

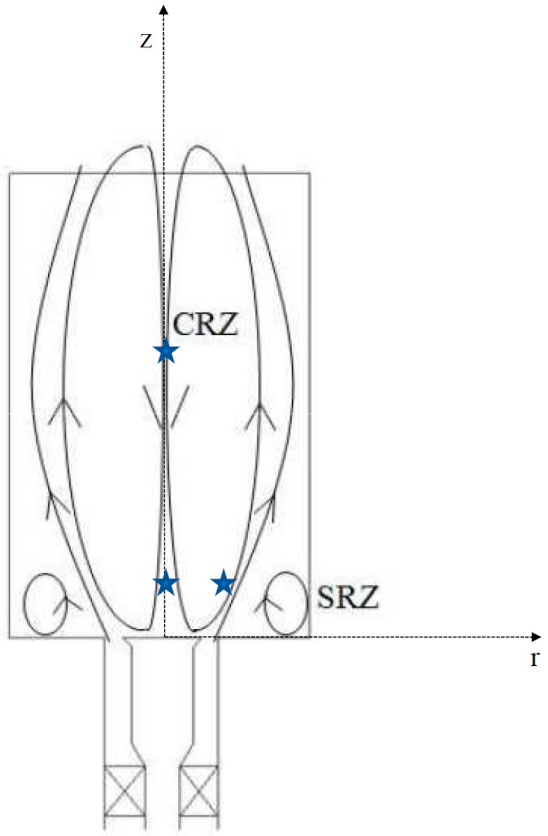

Figure 3.6: Schematic of the flow pattern and the recirculation zones. The stars denote the locations where the spectra of the instantaneous velocity have been determined.

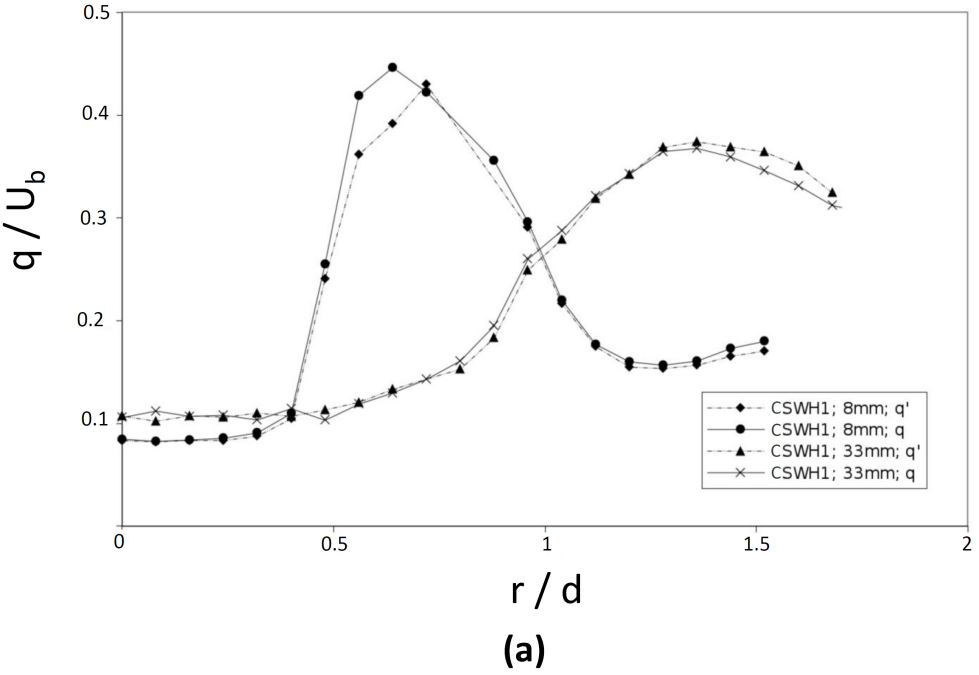

(a)

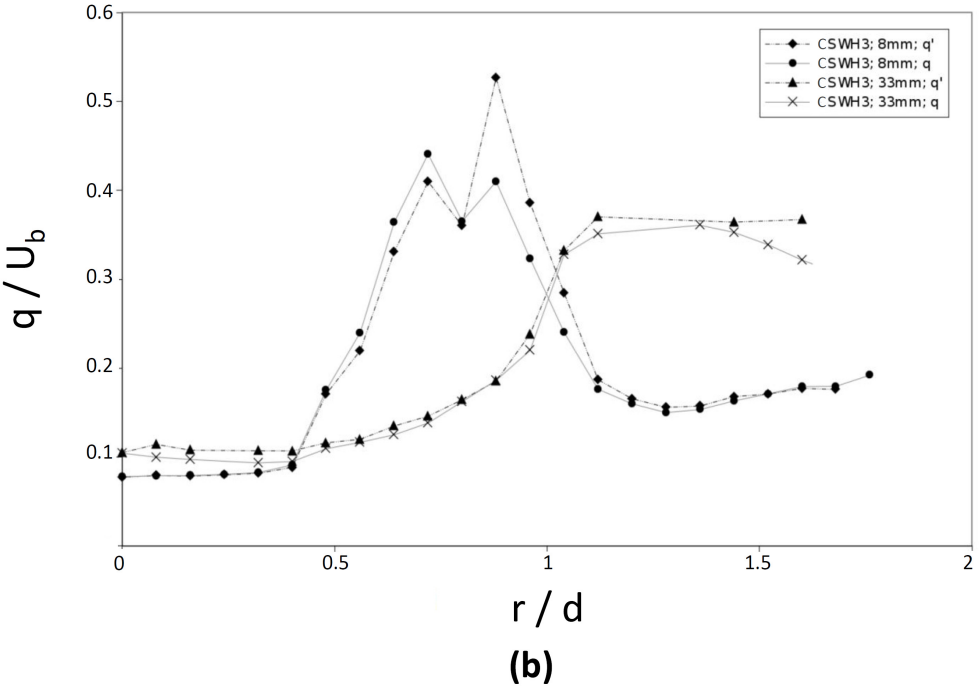

(b)

Figure 3.7: Radial distribution of the typical characteristic turbulent velocity q and q' at the condition CSWH1 (a) and at the condition CSWH3 (b).

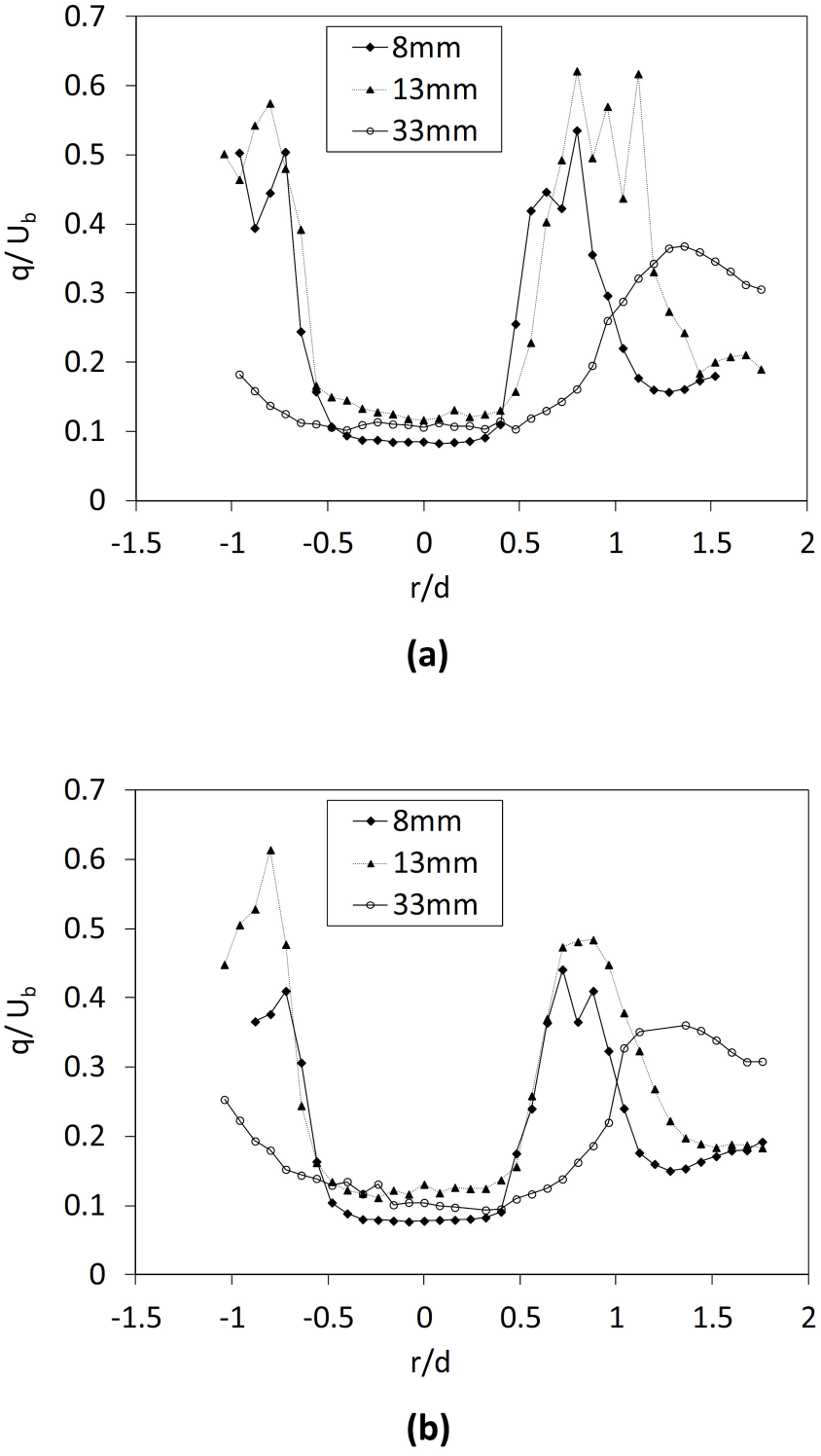

Figure 3.8: Radial distribution of the typical characteristic turbulent velocity, q, at CSWH1 (a) and CSWH3 (b) for three axial stations.

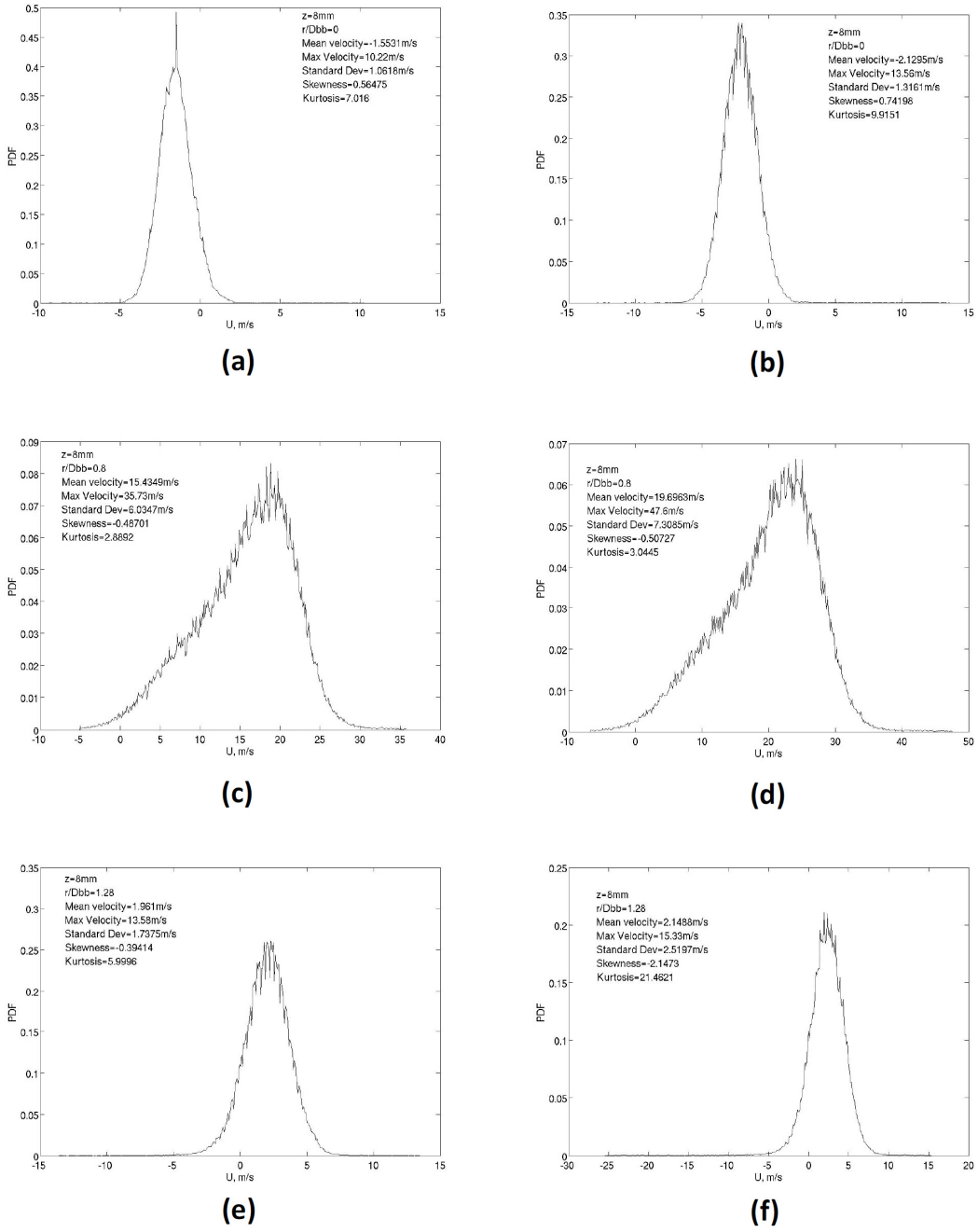

Figure 3.9: Probability density functions of the axial velocity at different radial position at z=8mm for CSWH1 flow condition (a, c, e) and CSWH3 condition (b, d, f).

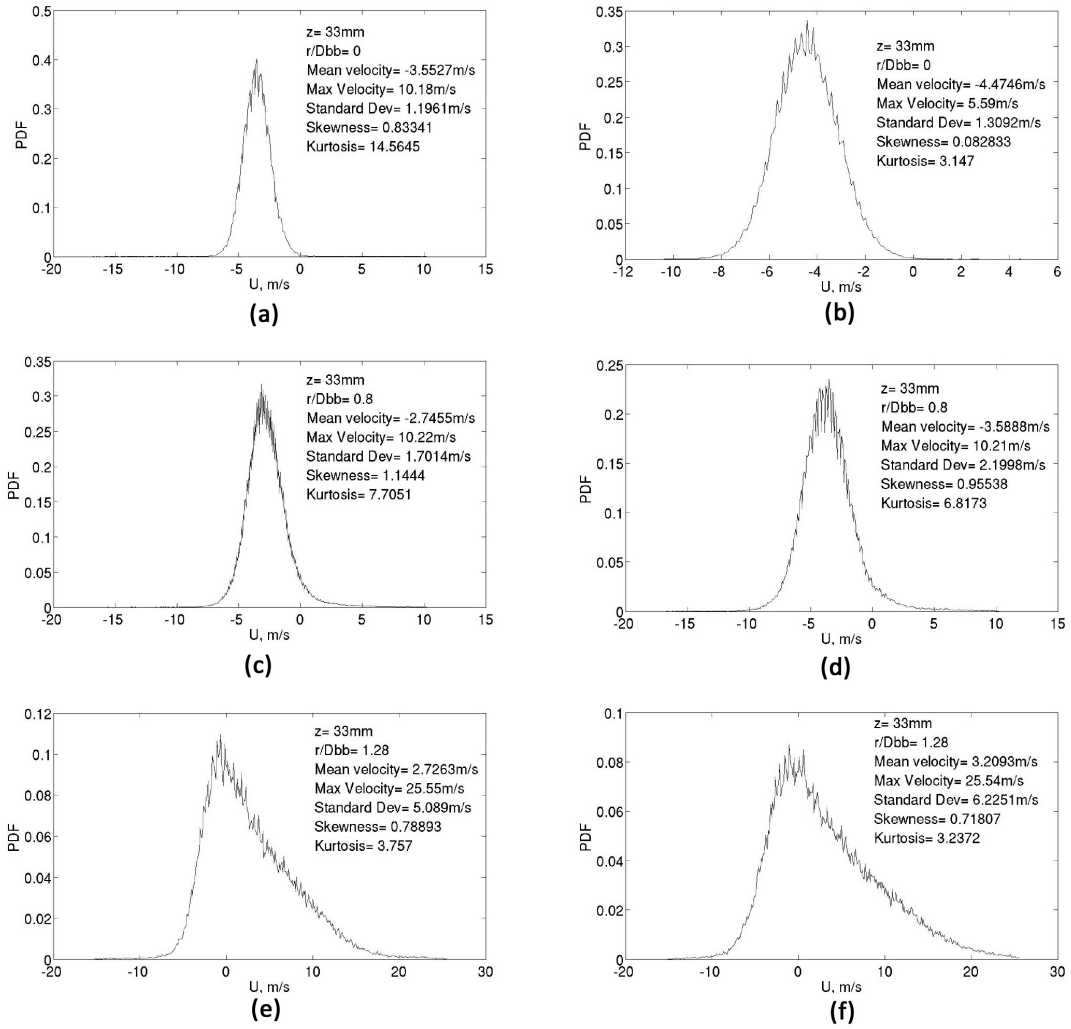

Figure 3.10: Probability density functions of the axial velocity at different radial position at z=33mm for CSWH1 flow condition (a, c, e) and CSWH3 condition (b, d, f).

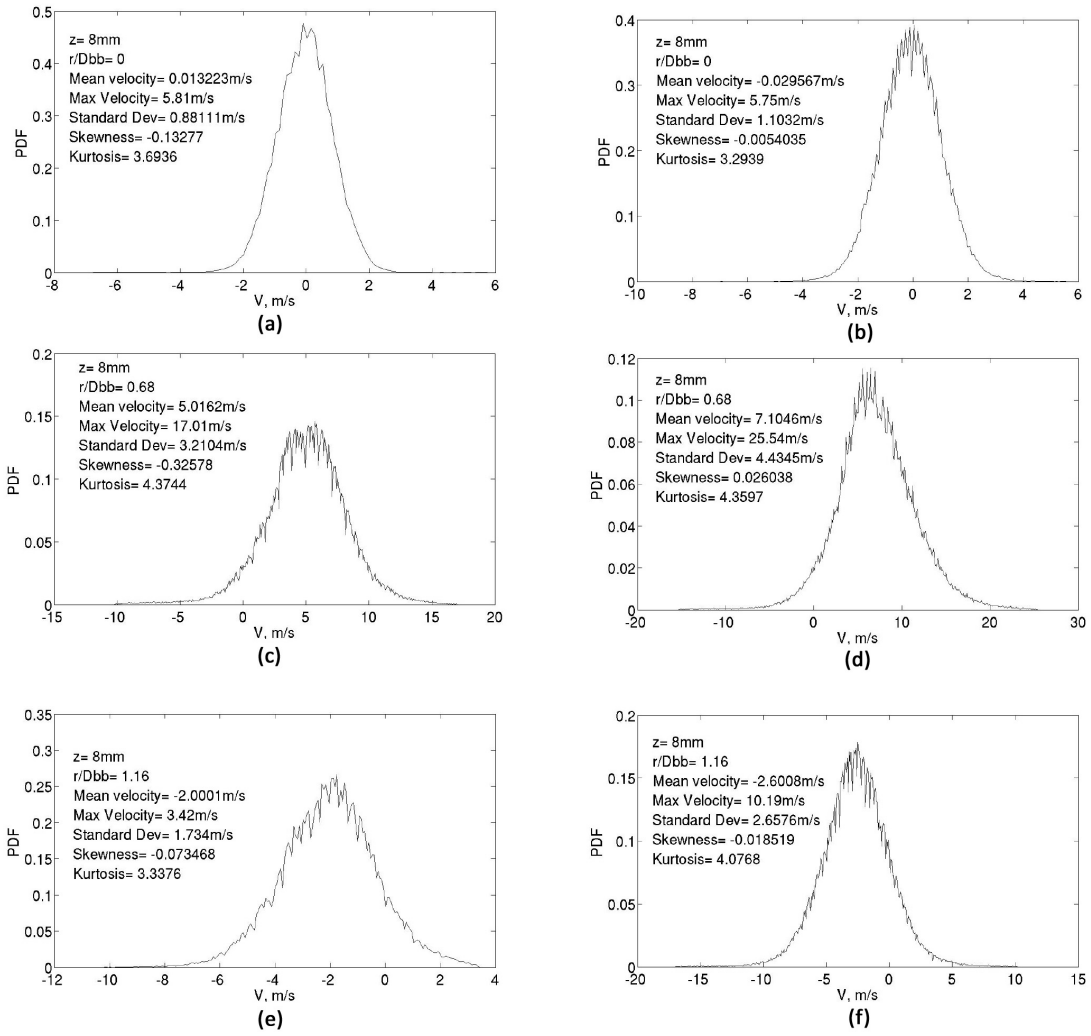

Figure 3.11: Probability density functions of the radial velocity at different radial position at z=8mm for CSWH1 flow condition (a, c, e) and CSWH3 condition (b, d, f).

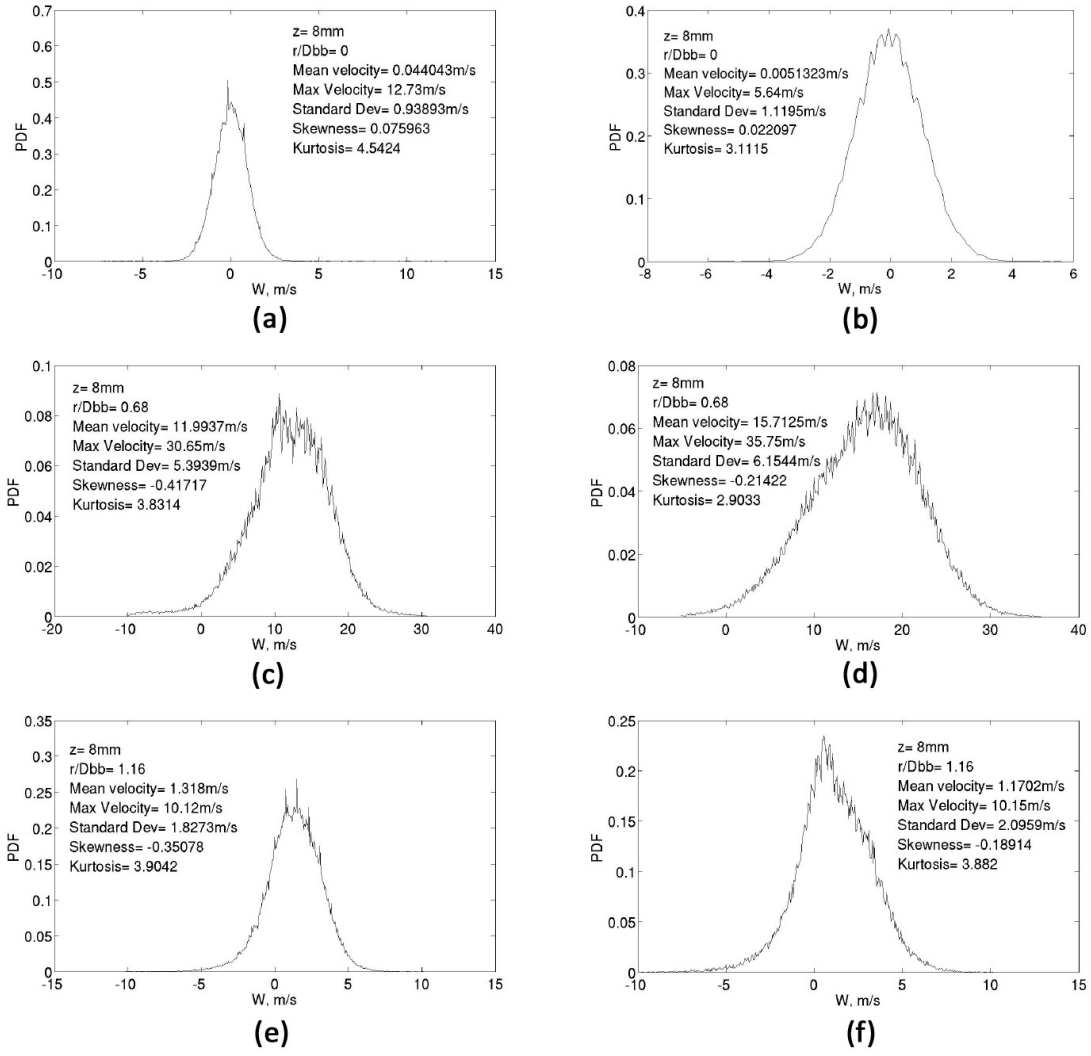

Figure 3.12: Probability density functions of the swirl velocity at different radial position at z=8 mm for CSWH1 flow condition (a, c, e) and CSWH3 condition (b, d, f).

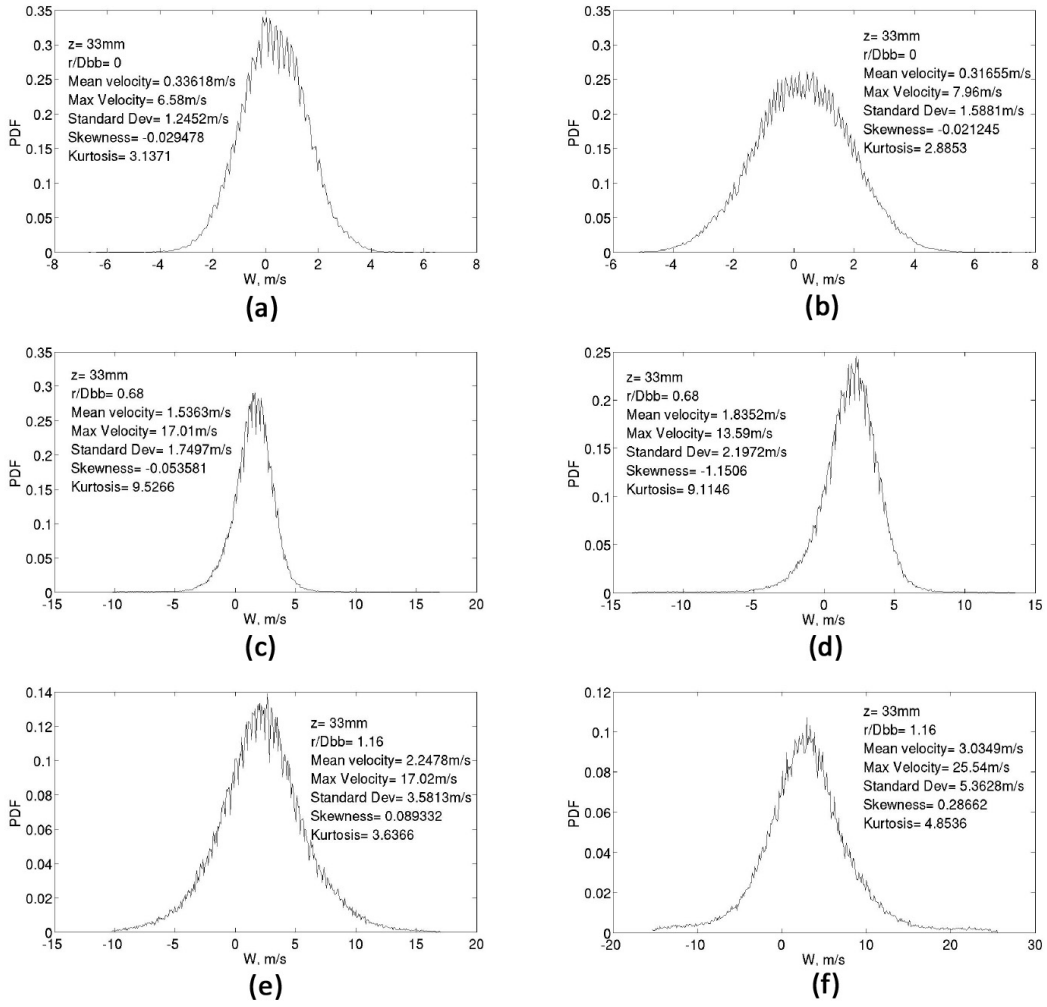

Figure 3.13: Probability density functions of the swirl velocity at different radial position at z=33mm for CSWH1 flow condition (a, c, e) and CSWH3 condition (b, d, f).

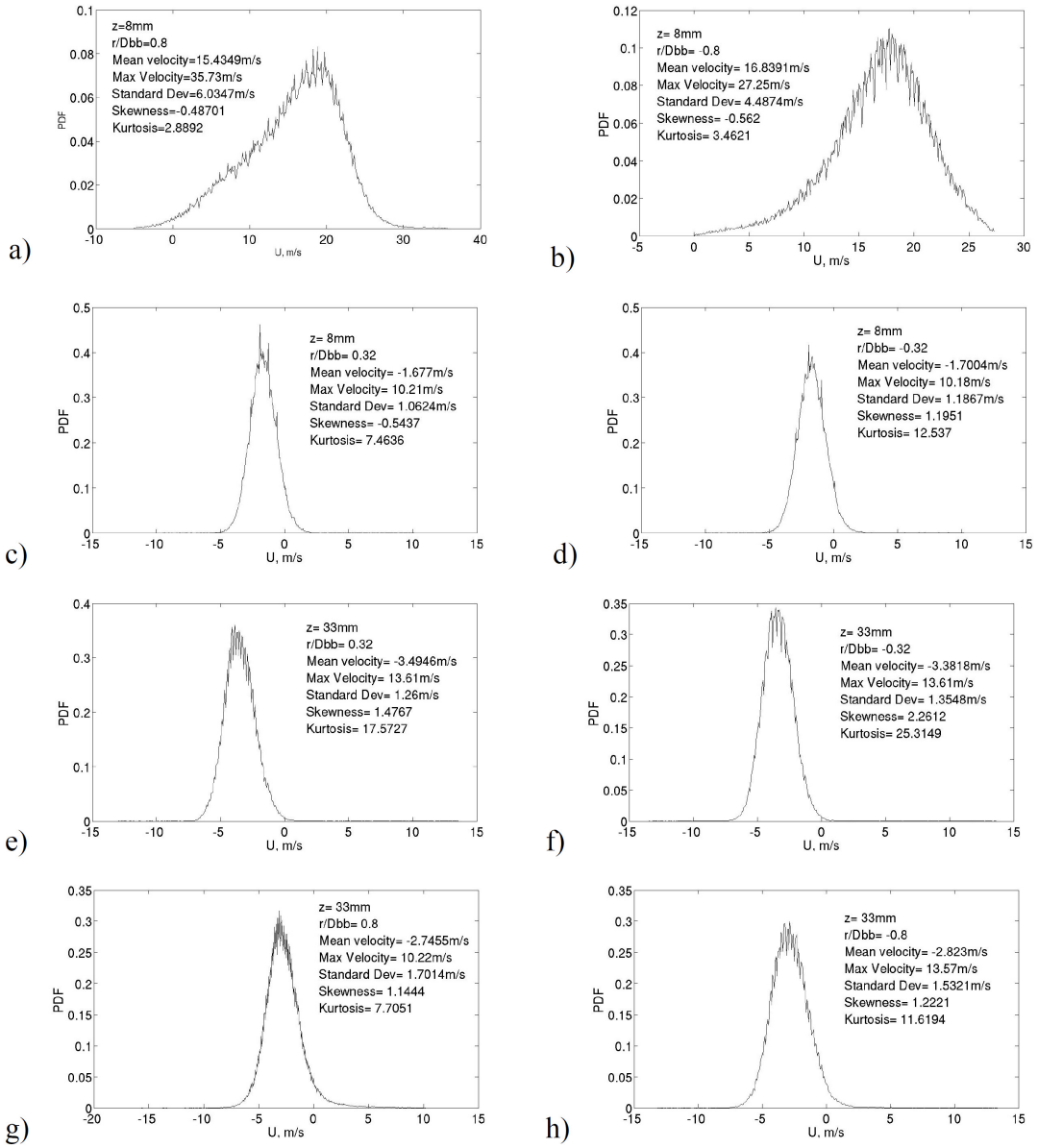

Figure 3.14: Probability density functions of the axial velocity at different radial position at z=8 mm (a-d) and 33 mm (e-h). CSWH1 flow condition.

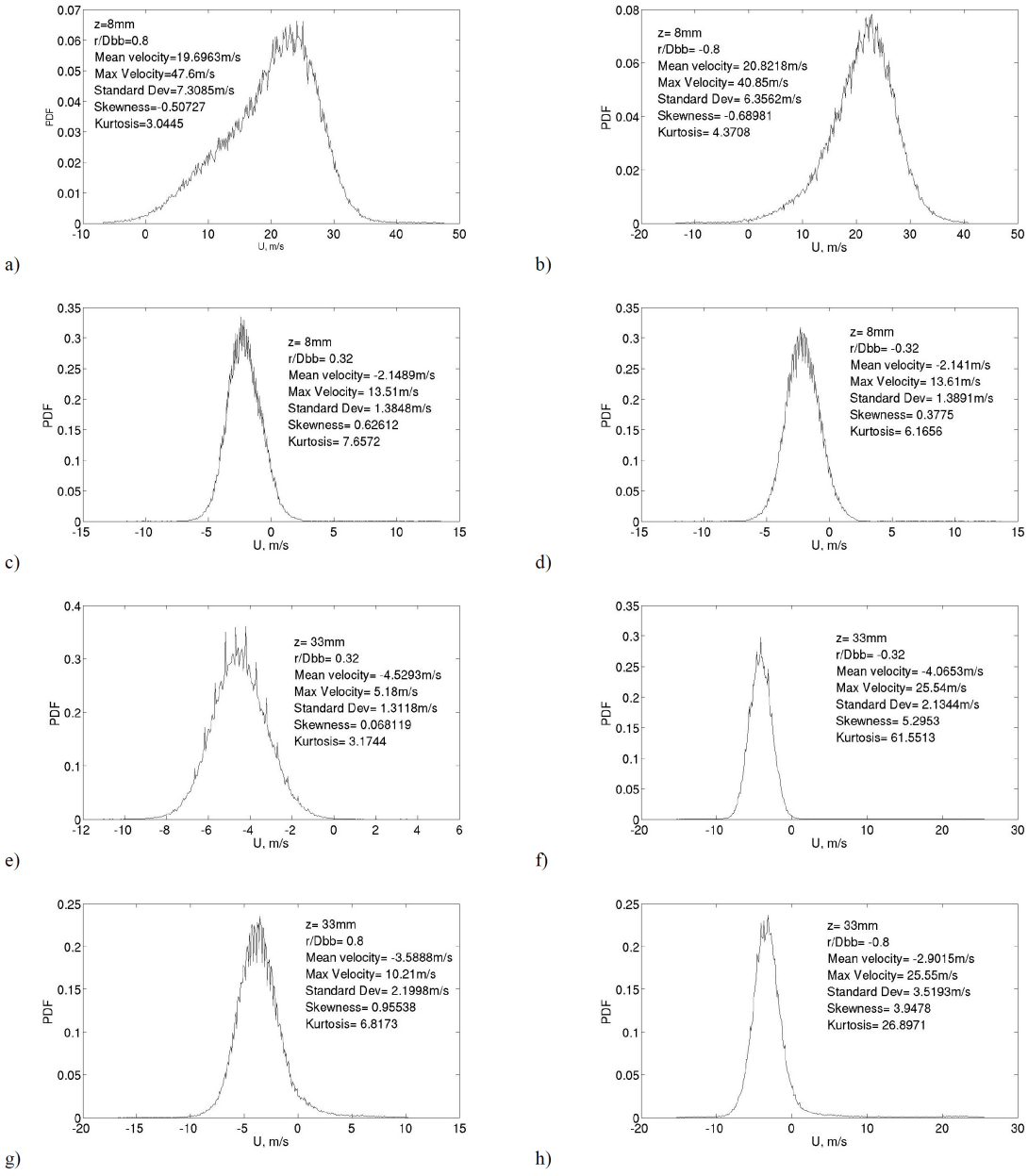

Figure 3.15: Probability density functions of the axial velocity at different radial position at z=8 mm (a-d) and 33 mm (e-h). CSWH3 flow condition.

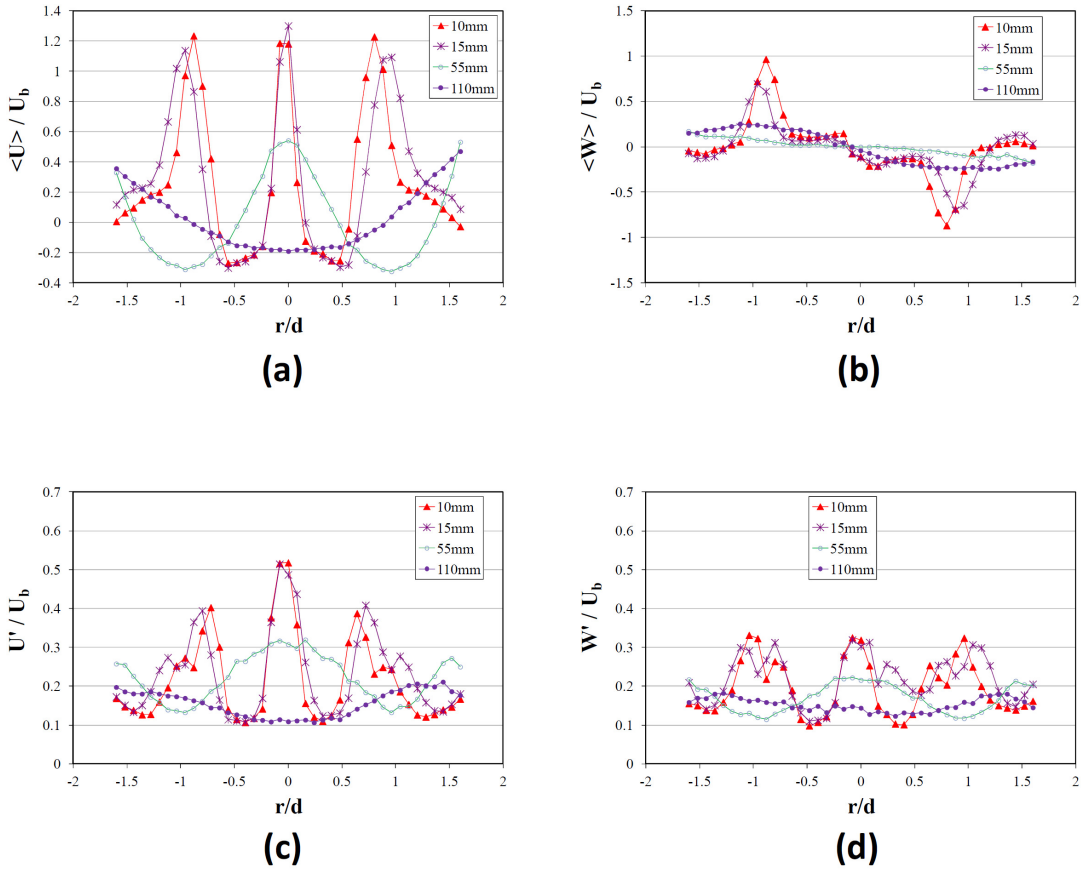

Figure 3.16: Mean axial velocity profiles (a), mean swirl velocity profiles (b), r.m.s of the axial velocity (c), r.m.s. of the swirl velocity (d). All profiles are normalized with the bulk velocity (U_b). The flow condition is F3A2 (non-premixed gaseous reacting case).

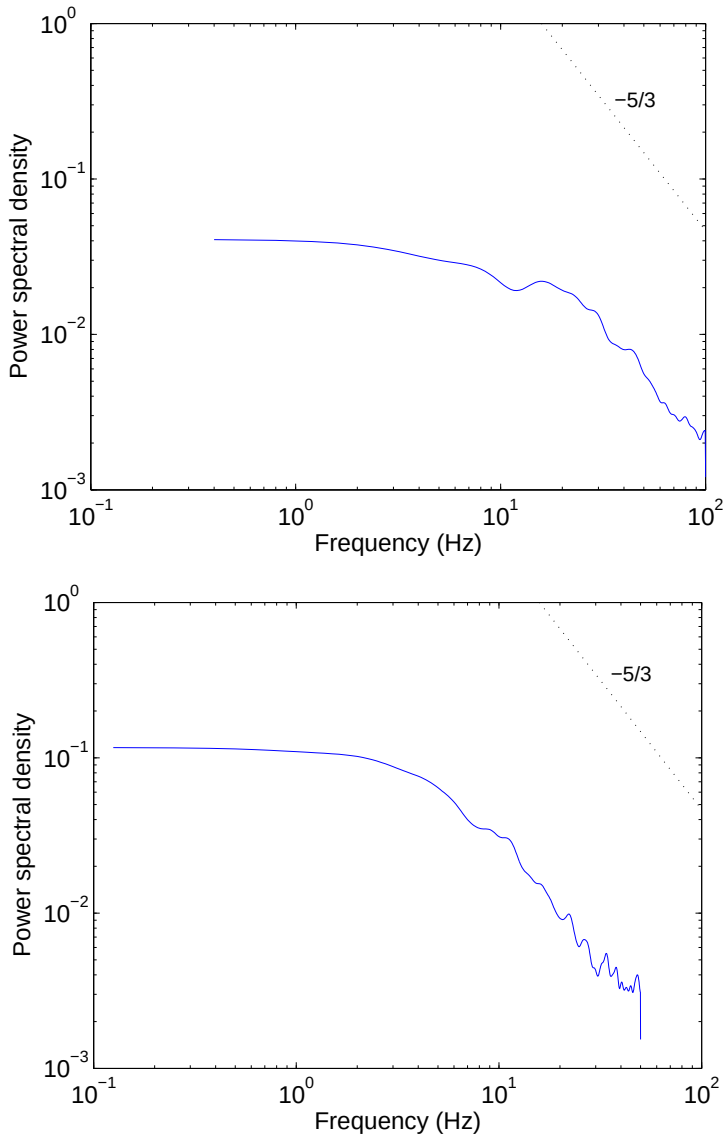

Figure 3.17: Profiles of Power Spectral Density of the axial velocity (upper) and swirl velocity (lower) for a downstream location z=15 mm and r/d=0. The dashed straight line represents the equation $y = x^{-5/3}$. The flow condition is F3A2 (non-premixed gaseous reacting case).

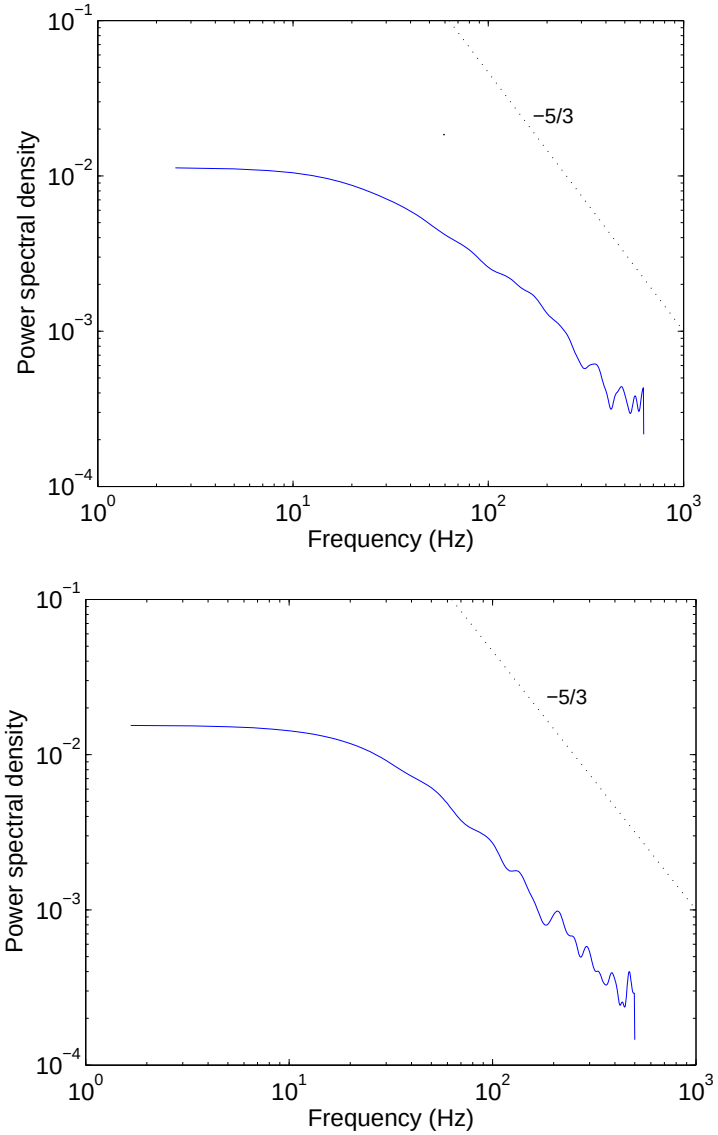

Figure 3.18: Profiles of Power Spectral Density of the axial velocity (upper) and swirl velocity (lower) for a downstream location z=15 mm and r/d=0.72. The dashed straight line represents the equation $y = x^{-5/3}$. The flow condition is F3A2 (non-premixed gaseous reacting case).

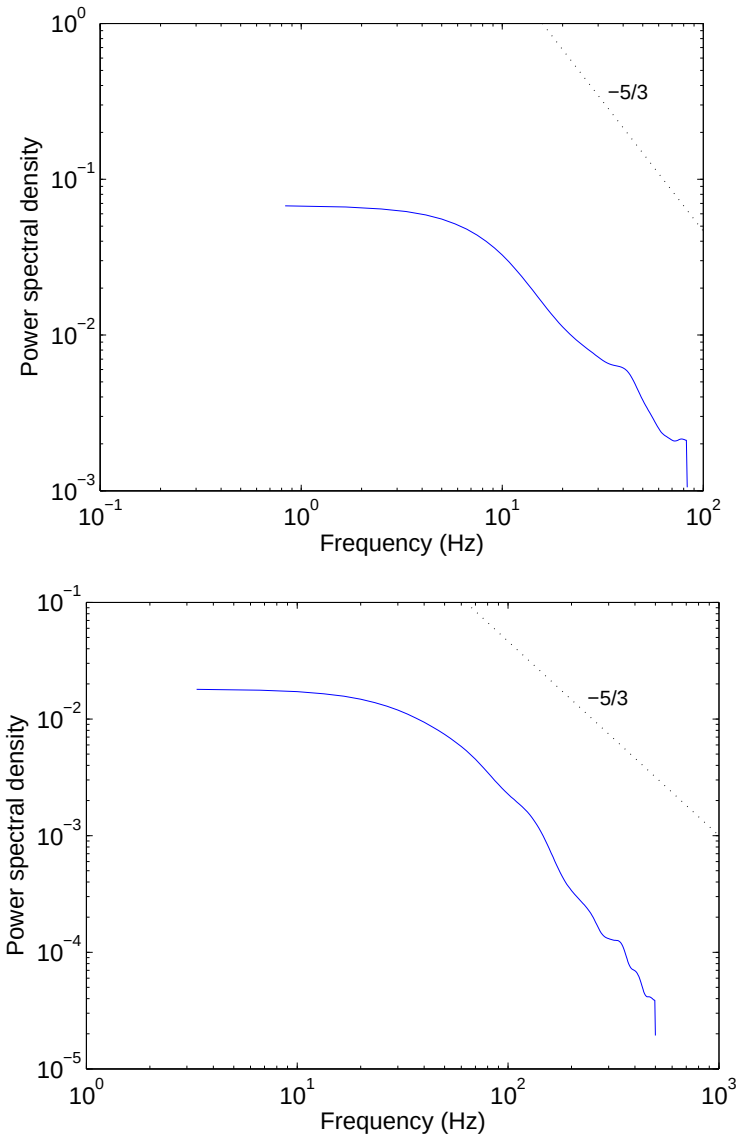

Figure 3.19: Profiles of Power Spectral Density of the axial velocity (upper) and swirl velocity (lower) for a downstream location z=110 mm and r/d=0. The dashed straight line represents the equation $y = x^{-5/3}$. The flow condition is F3A2 (non-premixed gaseous reacting case).

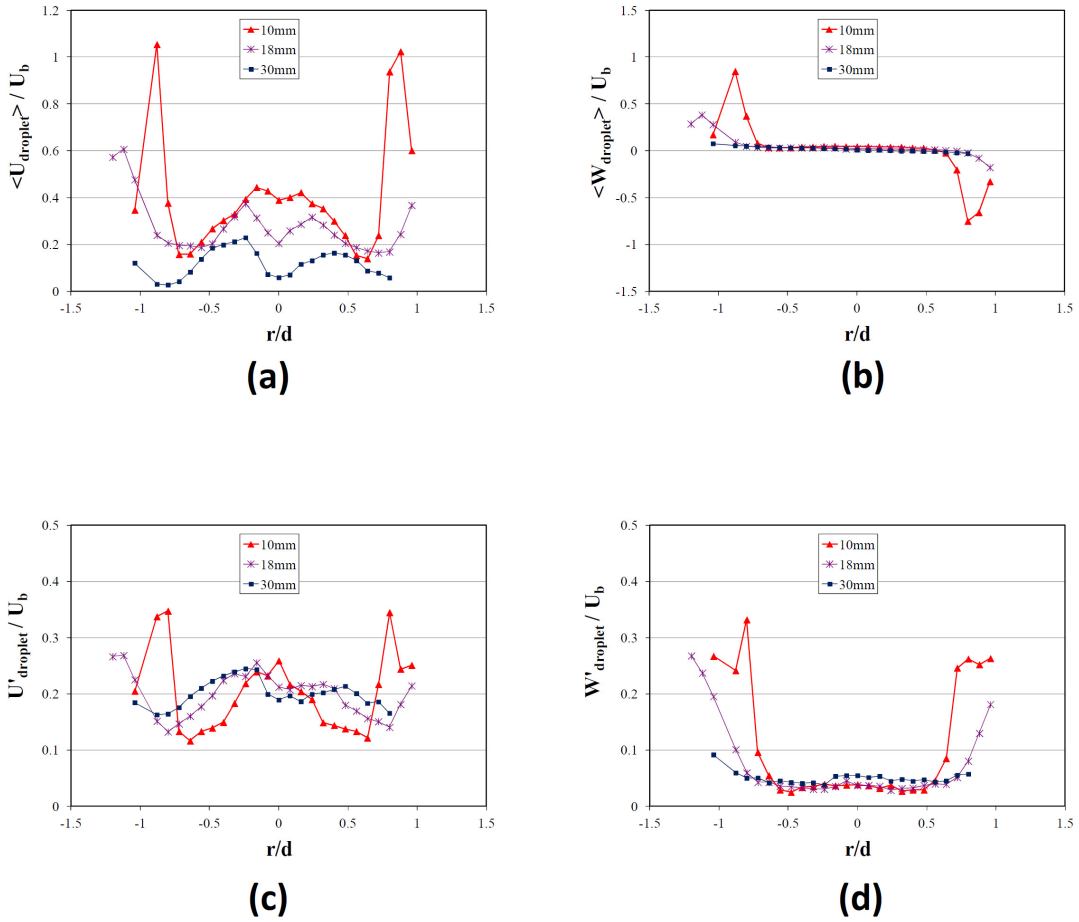

Figure 3.20: Mean axial velocity of the droplets (a), mean swirl velocity of the droplets (b), r.m.s of the axial droplet velocity (c), r.m.s. of the swirl droplet velocity (d). All profiles are normalized with the bulk velocity (U_b) and the radius by d. The flow condition is SWH1.

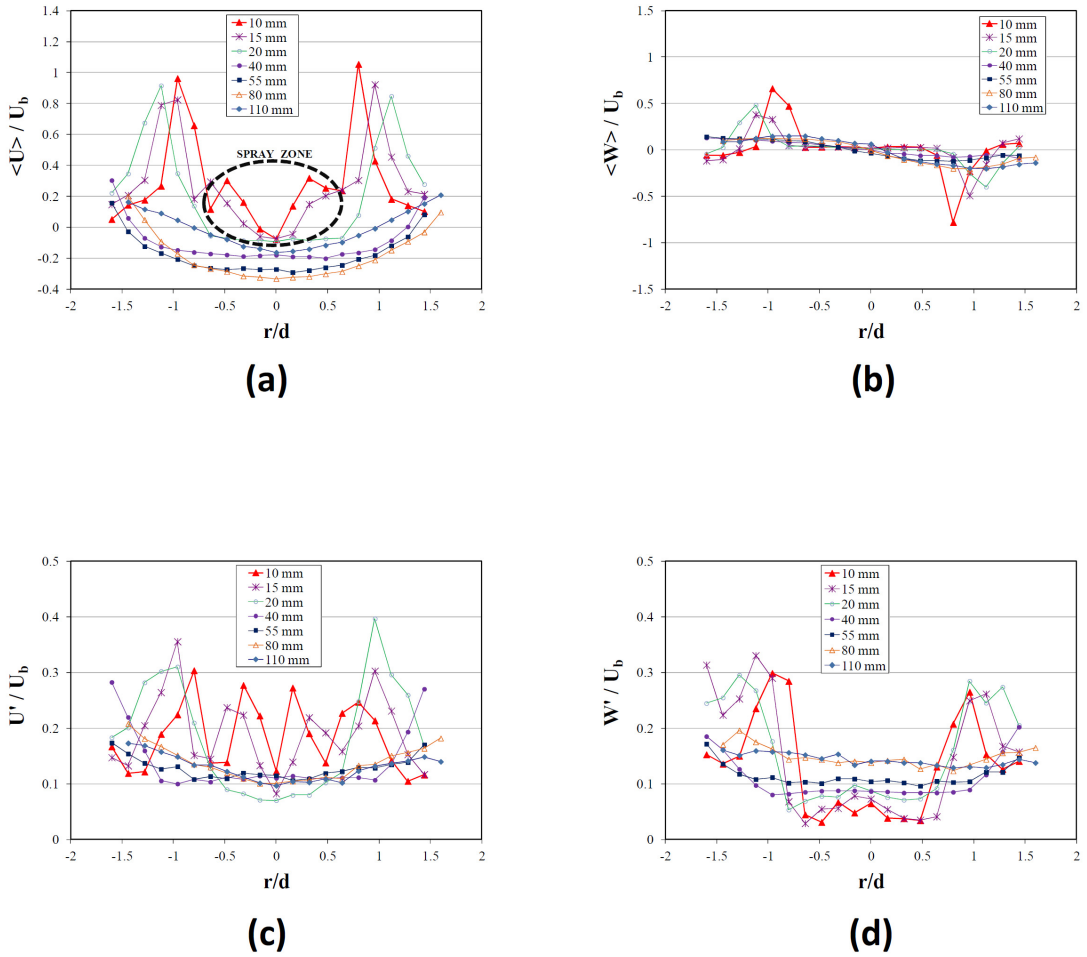

Figure 3.21: Mean axial velocity profiles (a), mean swirl velocity profiles (b), r.m.s of the axial velocity (c), r.m.s. of the swirl velocity (d). All profiles are normalized with the bulk velocity (U_b). The flow condition is SWH1 (spray reacting case).

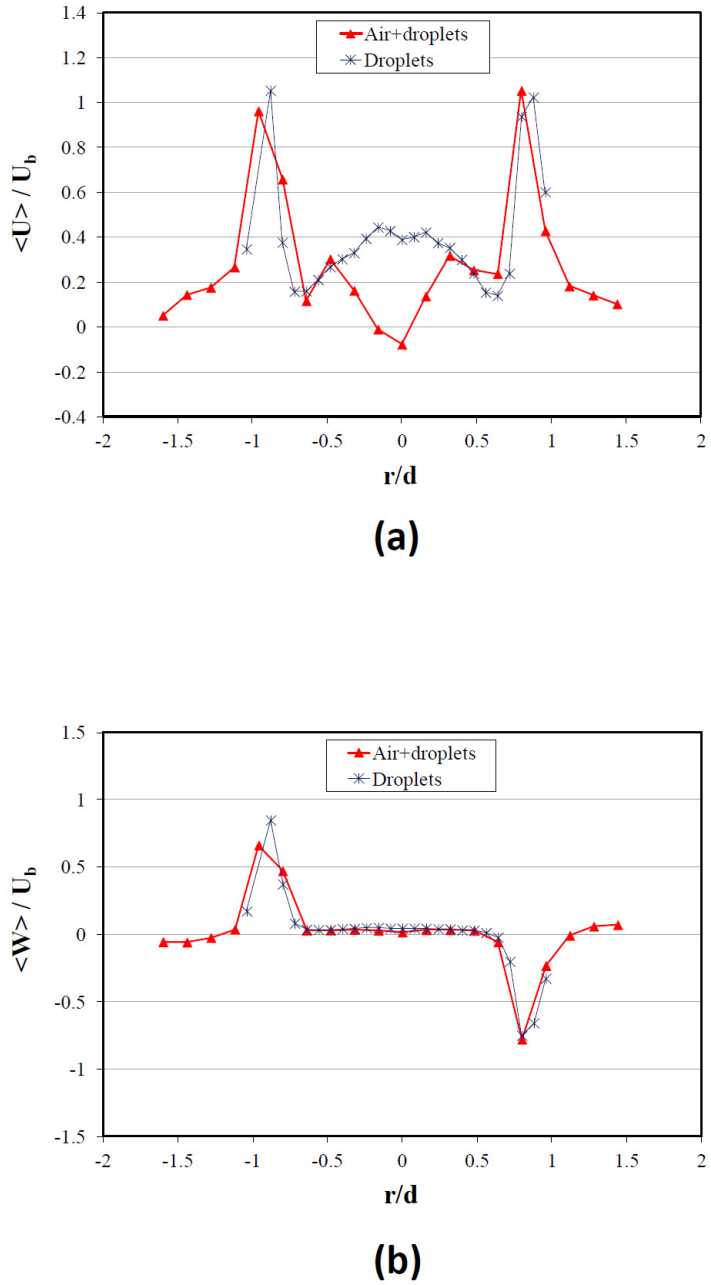

Figure 3.22: Mean axial velocity profiles of the droplets only and of the air with the seeding at z=10 mm (a), mean swirl velocity profiles of the droplets only and of the air with the seeding at z=10 mm. All profiles are normalized with the bulk velocity (U_b). The flow condition is SWH1 (spray reacting case).

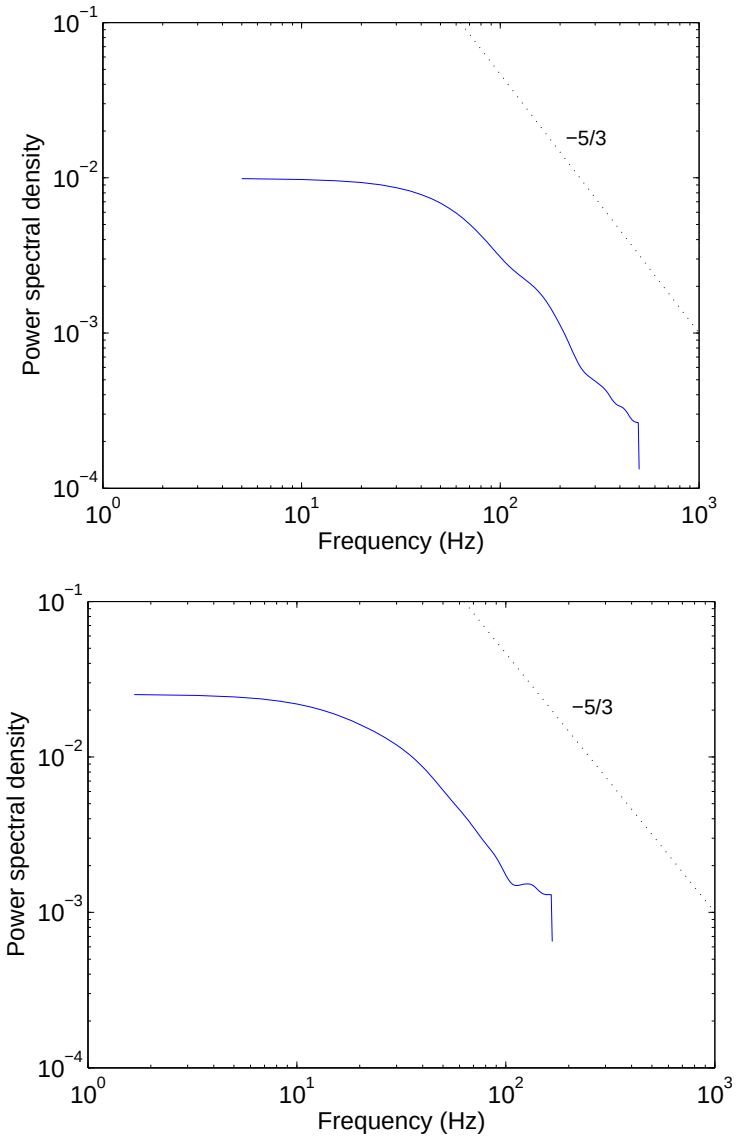

Figure 3.23: Profiles of Power Spectral Density of the axial velocity (upper) and swirl velocity (lower) for a downstream location z=10 mm and r/d=0.8. The flow condition is SWH1 (spray reacting case).

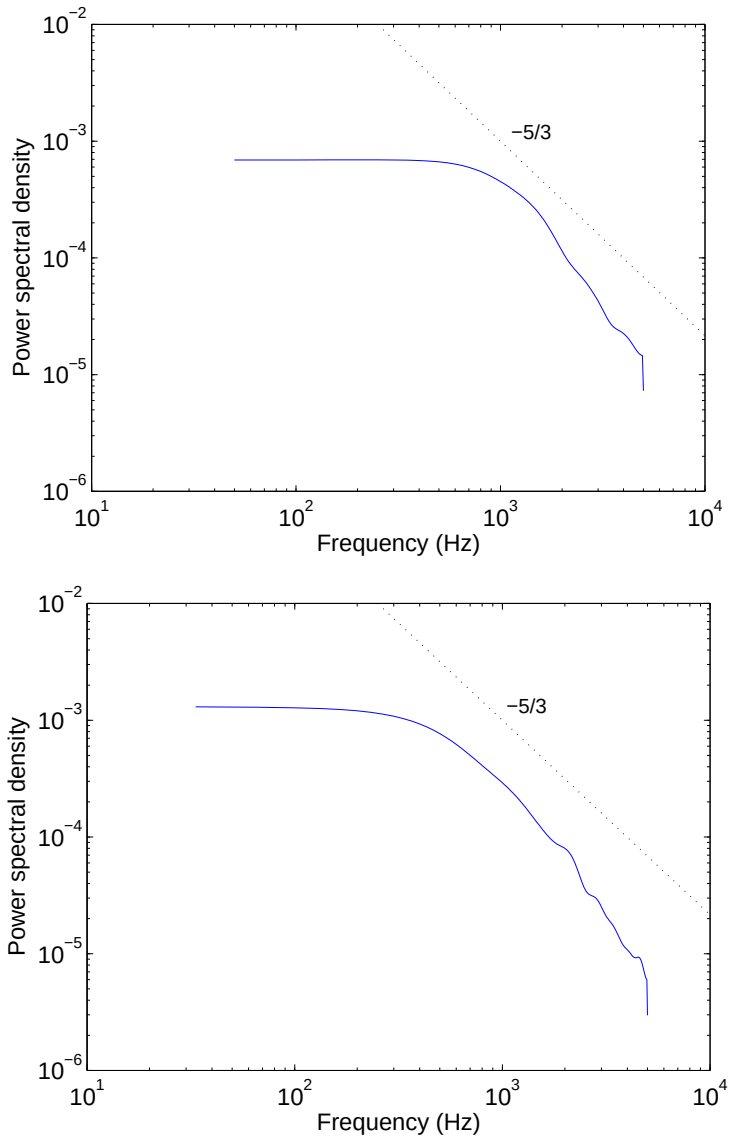

Figure 3.24: Profiles of Power Spectral Density of the axial velocity (upper) and swirl velocity (lower) for a downstream location z=20 mm and r/d=1.12. The flow condition is SWH1 (spray reacting case).

Chapter 4

Non-premixed flame blow-off

4.1 Introduction

This chapter presents an experimental investigation on stability and blow-off of turbulent non-premixed gaseous methane flames. The burner used is that developed by Marchione et al. [68] with a different (square) enclosure, modified for the non-premixed configuration, and described in section 2.1.1. Visualization studies of the flame behaviour both approaching and during a blow-off event are presented. Several measurements include imaging of OH* chemiluminescene and PLIF of the OH radical. Extinction limits of the non-premixed case at different flow conditions are discussed. Lift-off statistics and blow-off transient are presented as well. Emission measurements at the outlet are reported. Finally, the extinction correlation proposed by Radhakrihsnan et al. [89] is used to collapse the extinction data obtained in this study.

4.2 Motivation

The review presented in Chapter 1 showed that most of the investigations were conducted on pilot jet flames or non-swirling flames. The blow-off dynamics of short flames have received little attention. Moreover, to the author's knowledge, a quantitative evaluation of the extinction time for non-premixed cases has not been yet investigated. This study aims to provide measurements of different

flames both far and close to the extinction limit by using fast diagnostics systems and to evaluate the duration of a blow-off event. These data could be applied in comparative studies with new advanced combustion models such as Large Eddy Simulations. In order to help the interpretation of the results, some emphasis on how the flame changes as the extinction condition is approached is also given.

4.3 Experiment methodology

The blow-off limit was obtained in the following manner. The air and fuel flow rates were set to give a mixture condition far from the extinction where the flame is completely stable. U_b is the bulk velocity at the annular exit. The fuel flow rate was fixed and then gradually the air flow rate was increased in steps of approximately 0.258 m/s every 20 seconds until blow-off occurred, and then the blow-off velocity, U_{BO}, and the corresponding overall equivalence ratio, ϕ_{BO}, were recorded. The structure of the flame from stable conditions (F3A1, F3A2) to complete extinction ($F3A3\_E$) was investigated at various stages reported in Table 4.1, and also marked in Fig. 4.1. The extinction limit was measured for a range of different fuel velocities between approximately 20 m/s to 50 m/s. The fuel jet velocity was 29.2 m/s always.

4.4 Data analysis

Images of OH* chemiluminescence were obtained for flames F3A1, F3A2 and $F3A3\_E$. Time averaged and RMS images were obtained from a set of 1000 images for the stable conditions, F3A1 and F3A2. As the average flame is axisymmetric, the location of the reaction zone can be observed from converting the ensemble average chemiluminescence image with an Abel transform. The Abel transform should be used in principle only for fully axi-symmetric systems, which is indeed the case for all flames examined in this work because the flame is far from the wall.

For each stable condition, a data set of 1000 images of OH-PLIF was acquired at an imaging rate of 5kHz. During processing, each instantaneous image was initially filtered using a 2-D median non-linear filter for noise reduction (3×3

filter size). The filtered images were then corrected for inhomogeneities in the laser sheet profile.

4.5 Results and Discussion

In this section stability limits, instantaneous and time averaged images, measurements of the blow-off transient, Damkohler correlation and concentration measurements are presented and discussed for flames F3A1, F3A2 and $F3A3\_E$.

4.5.1 Stability limits

Fig. 4.1 shows the stability limits of the non-premixed case. It is evident that, as expected, the air velocity at extinction increases with fuel jet velocity (so increasing the overall equivalence ratio, ϕ_{ov}). Correlating this data will be discussed later. The flames studied by the diagnostics are shown by stars. The figure also contains some statistical information obtained from the images that is discussed later.

Table 4.1: Test cases evaluated for various stable and blow-off conditions. The fuel exit velocity is 29.2 m/s.

Flame type	Name	Case	U_{bulk} [m/s]	ϕ_{ov}
Non-premixed	F3A1	Stable	15.7	0.38
Non-premixed	F3A2	Stable	19.1	0.31
Non-premixed	F3A3_E	Blow-off	19.9	0.30

4.5.2 Flame shape

Photographs of the non-premixed flame at stable conditions F3A1 and F3A2 are shown in Fig. 4.2a and Fig. 4.2c respectively. The flame is sooty far from blow-off (F3A1), but close to the extinction it becomes blue and shorter. The reaction zone location was revealed by OH* chemiluminescence, Figs. 4.2b and 4.2d respectively. The chemiluminescence images show a slight change in the

flame shape as the blow-off condition is approached. The results of this are presented in Figs. 4.2b and 4.2d, where the time averaged OH* chemiluminescence image is converted using an Abel transform.

For stable burning conditions, the flame takes an inverted conical shape and is anchored on the bluff body with flame being present up to 95 mm. The average length of the flame brush is approximately $3.5d$. Low chemiluminescence is observed above z =35 mm (Fig 4.2d). As blow-off is approached, by increasing the air flow rate the flame becomes shorter, while the emission of OH* chemiluminescence near the attachment point at the bluff body becomes stronger. It is also clear that the flame brush becomes narrower. These flames are similar to the short flames of Ref. [34] with axial fuel injection and to those of Ref. [2] with radial injection.

We expect non-premixed flames to reside mostly along the stoichiometric contour and this is expected to be shorter with an increase in air flow rate with fuel flow rate staying constant, which is consistent with the above observations. However, the change in flame shape as blow-off is approached is not as drastic as that observed with the approach to extinction of the premixed flame in a similar geometrical configuration by Kariuki et al. [52; 53], which shows a migration of the flame into the CRZ.

4.5.3 Flame behaviour approaching blow-off

Measurements of OH-PLIF for the flame approaching the blow-off condition, shown in Fig. 4.3a-d, validate observations from the chemiluminescence images. A characteristic feature is the almost complete absence of OH inside the RZ. This is evident in Fig. 4.3a-d that shows the normalized mean and RMS OH-PLIF for the two stable conditions. In particular, the RMS OH-PLIF image indicates that the concentration fluctuations of OH along the centerline are negligible; the flames in the present stable conditions show OH only in thin regions at the sides of the CRZ.

Figure 4.4 shows a sequence of instantaneous OH-PLIF images every 0.2 ms at the stable flow condition $F3A1$. At conditions far from blow-off, the reaction zone appears contorted. High regions of OH are observed along the shear layer,

indicating reaction. In this sequence it is possible to observe a lift-off event and a reattachment in the range of time 0-1.2 ms and some localized extinctions are evident in the right leg of the flame at 2-2.8 ms. No flame is observed in the side recirculation zones (SRZ) and along the centerline.

The flame intermittently lifts-off the bluff body (at a height h shown in Fig. 4.5; to be discussed quantitatively later). The absence of OH in the central part of the flow (i.e. flame only along the shear layer) is consistent with the quick mixing of the fuel jet. It is evident also that the flame sheet is not continuous, with gaps in the OH field (some of these holes are marked by the white circles on Fig. 4.5). These holes emerge at random, close, and re-appear, and are likely to be localised extinctions. The speed of these phenomena cannot be resolved fully with the present 5 kHz system due to the fast air flow and the presence of swirl. In the absence of simultaneous mixture fraction information, it is not possible to discuss with certainty whether these are indeed extinctions along the stoichiometric contour or not. However, at least for the part of the flame until about $1d$, play-back of the movies do not show any random emergence of flame islands away from the main flame sheet, which would be the characteristic of an out-of-plane motion of a continuous flame occasionally cutting the laser sheet, a behaviour indeed occasionally seen at the downstream end of the observation window. Therefore it is likely that breaks in the early part of the flame are extinctions, similar to those seen in the piloted jets [50; 101].

Since mixture fraction data is not available yet, complete interpretation of the methane flame is not feasible. Further measurements of the mixture fraction must be performed.

4.5.4 Lift-off height statistics

In this Section, the lift-off height h, indicated in Fig. 4.5, is quantified for various conditions. Detachment from the attachment point was investigated by evaluating the gradient of OH of the instantaneous OH-PLIF image corrected for laser sheet inhomogeneities. A suitable threshold was then chosen to filter out low gradients of OH, which were observed not to overlap with the boundary of the high OH regions. The separation distance from the bluff body edge to the high

gradient of OH regions was evaluated, and is here referred to as the lift-off height.

The mean values of the lift-off height, $\langle h \rangle$, have been calculated based only on images that show lift-off, and these values are indicated on Fig. 4.6, together with the probability of finding a lifted flame, P_{lift} (defined as the ratio of the number of images with lift-off to the total number of images; the left and right branches of the flame in each individual snapshot are considered as two different samples). Figure 4.6 shows the pdfs of the lift-off height measured from the OH-PLIF movies, conditional on $h > 0.2$ mm. A wide pdf is observed, with a long positive tail. The non-premixed flame, when lifted, has an average lift-off height that increases as the fuel velocity increases or the air velocity decreases (Fig. 4.6) and P_{lift} increases with fuel velocity.

A spectrum analysis of the time-series of OH-PLIF at few locations along the shear layer (at a distance of 2 mm from the bluff body and at r/d=$\pm$1.45) was performed to investigate the temporal behaviour of flame front observed in Fig. 4.5. The spectra of OH, reported in Fig. 4.7 for the stable conditions F3A1 and F3A2, are relatively smooth, with no distinct peaks observed for any of the locations examined for both flame legs. This indicates no periodicity in the flame front as it corresponds to the random nature of the turbulent flow field for the frequency range investigated here. Thus, the intermittent re-attachment of the flame does not follow a particular frequency, as concluded by the lack of any peaks in the spectrum of the OH-PLIF signal (Fig. 4.7).

Large-eddy simulations with models that can include localized extinctions (for example, the Conditional Moment Closure [7; 37] or the transported PDF method [48]) have been shown to be able to reproduce statistics of localized extinctions. The present data could be used for further validations of such modelling efforts for flames of greater technological relevance.

4.5.5 Blow-off transient and its duration

Increasing the air flow rate from condition F3A2 leads to the blow-off condition $F3A3\_E$. The flame shape and reaction zone behavior during the extinction transient was recorded using OH* chemiluminescence and OH-PLIF imaging system at 5 kHz. The extinction event was approached from conditions away from the

blow-off by increasing the air flow rate and continously triggering the high speed camera imaging system, stopping the acquisition once the flame had completely disappeared.

Sequences of OH* chemiluminescence and OH-PLIF during a blow-off event are shown in Fig. 4.8 and in Fig 4.9 respectively. Figure 4.8 shows the sequence of two independent blow off events starting 200 ms before the flame was fully extinguished. In the first row the frame shrinks up to 60 ms before extinction. Then, starting from 50 ms the flame becomes shorter and in the last two frames at 10 and 5 ms the flame is present only in narrow faint regions. The flame brush is observed to become shorter, decreasing its height from $2.3d$ to $0.6d$ in 180 ms (Fig. 4.8). It is also observed that in the last 20 ms a disintegration of the flame occurs just on the bluff-body. The last flame fragment to survive is above the bluff body.

OH-PLIF measurements during the extinction transient are shown in Fig 4.9. The flame shrinks and it is very fragmented. Regions of high OH emissions are observed on the left leg of the flame between the central recirculation zone and the annular inlet. During the last 20 ms the flame has disintegrated significantly. A last element survives for 10 ms before the complete extinction occurs.

Thus, the complete flame disintegration process lasts a substantial time. The average duration of the blow-off transient was quantified in detail for the first time in Ref. [29] for non-swirling premixed flames, and here we extend these measurements for swirling non-premixed flames. Many blow-off movies, captured with fast imaging (5 kHz) of OH* chemiluminescence, were used to quantify the duration of the blow-off transient. The emission from each image was integrated, which then gave a time series of the area-integrated OH*. Each of these time series was time-shifted such that extinction occurred at an arbitrarily chosen time, here denoted as t_0. The OH* was then averaged over time from the beginning of the time series until the start of the decay to zero, and this average value was used to normalize each corresponding time series, Fig. 4.10. Hence for each blow-off event, we obtain a time series of the normalised, time-shifted, area-integrated OH* chemiluminescence that shows a relatively steady condition with finite emission before blow-off and a transition to zero emission. Ten time series, from different blow-off events at similar conditions, were then averaged. This gives the average

behaviour of the blow-off event. Then, this average signal $\langle OH^* \rangle$ was examined closely to quantify the duration of the blow-off event, τ_{ext}. This was defined as the time needed for the emission to decrease from 90% to 10%. The result is an extinction time of 46.6 ms. This extinction time for a non-premixed swirling flame has the same order of magnitude of the extinction time measured in a turbulent premixed flame without swirl [53].

It is not clear yet which characteristic time should be used to collapse the raw measurement of τ_{ext}. Using the characteristic time d/U_b, we get that the non-premixed flames have $\tau_{ext}/(d/U_b)$ of around 40.

As preliminary comment it is of interest to note that the present data suggest that significant time may be available for transient control strategies to avoid blow-off. Moreover, the extiction times measurement can be used to assess the capability of a combustion model, e.g. based on LES, to predict the transient blow-off behaviour of burners.

4.5.6 Blow-off correlation

Radhakrishnan et al. [89] proposed an interesting turbulent premixed flame extinction theory. It is fully described in Section 1.2.1. This extinction criterion postulates that extinction will occur when

$$\frac{1}{Da} = \left[\left(\frac{C_1}{C_2} \frac{15}{A} \right) \left(\frac{U_b}{d} \right) \left(\frac{\nu}{S_L^2} \right) \right]^{1/2} > R \tag{4.1}$$

This correlation has not been used before for swirling non-premixed flames. In the original paper [89], its validation was based on extensive data sets with fully premixed flames in afterburner-type geometries without swirl.

Here, we employ Eq. 4.1 for the the non-premixed case using the diameter of the bluff body as characteristic length. The value of the laminar flame speed, S_L, was estimated at stoichiometry (taken from the data of Massias et al. [73]) and ν evaluated at a temperature halfway between the reactants and the adiabatic flame temperature as suggested by Mellor [75].

The resulting values of the group $\left[\left(\frac{U_b}{d} \right) \left(\frac{\nu}{S_L^2} \right) \right]^{1/2}$ are shown in Fig. 4.11. The values lie in the range 0.9 to 1.23. The scatter in Fig. 4.11 is considerably

smaller than the scatter generally observed for other correlations in the literature [75; 89; 96]. It is evident that the non-premixed flame at different flow conditions extinguishes at approximately the same critical value of Da. This gives support to the use of Eq. 1.8 for predicting swirling flames. From Eq. 1.8, it is evident that the critical velocity depends on the chemical timescale ν/S_L^2, on the flame-holder size d, and on the exact aerodynamics inside the combustor through the ratios u'/U_b and L_t/d. For the same burner, we expect u'/U_b and L_t/d to be approximately the same for the reported cases, and hence the very good collapse of the blow-off data in Fig. 4.11 gives credence to its general use.

4.5.7 Emission measurements

The pollutants of interest in gas turbine related problems are oxides of nitrogen (NO_x), carbon monoxide (CO) and unburned hydrocarbons (UHC). Sulfur oxides (SO_x) are emitted based on the sulfur (S) content of the fuel [104]. SO_x is a major concern for non-premixed systems burning coal or low-quality oils [104] and since natural gas contains essentially no sulfur, a discussion of SO_x emissions will not be presented in the present work.

The primary nitrogen oxide from combustion systems is NO; although in some non-premixed systems, appreciable NO_2 is produced, usually as result of $NO \rightarrow NO_2$ conversion in low-temperature mixing regions [104]. The nitrogen monoxide (NO) is formed mainly through three mechanisms: (a) the thermal (Zeldovich) mechanism in which O, OH and N_2 species are at their equilibrium values and N atoms are in steady state, (b) the Fenimore (or prompt) mechanism, (c) the N_2O-intermediate route.

Although the chemical processes are the same in premixed and non-premixed combustion, the additional mixing process associated with the non-premixed case can produce a range of local compositions spanning a wide range of stoichiometries. Even if the overall mixture is stoichiometric, within the combustion chamber there may be rich or quite lean regions. This aspect adds complexity to the problem of pollutant formation in non-premixed systems and in fact to temporal and spatial variation of the fuel/air mixing impact emissions of NO_x as observed in [35; 66].

All three mechanisms forming NO_x are likely to be active in non-premixed systems; the determination of the relative contribution of each mechanism to the total NO_x yield is yet a subject of research [104]. However, the main parameters determining NO_x are temperature, composition and residence time. In general, the thermal NO is produced mainly in flame regions that have simultaneously high temperatures and high concentrations of O and OH atoms, while the Fenimore mechanism is particularly important in rich combustion regions and may contribute as much as 50% of the total NO_x emission [16]. The N_2O intermediate mechanism plays an important role in the production of NO in very lean, low-temperature combustion processes [104].

Both CO and UHC are the products of incomplete combustion. Given sufficient time and at high enough temperatures, these two pollutants would be further oxidized to carbon dioxide and water. In the non-premixed case, CO results directly from the nature of the non-premixed combustion. Fuel inlet characteristics and fuel-air mixing patterns are important parameters affecting CO formation. In this work, the stable flames studied are close to extinction, an indicative characteristic of this condition should be very low NO_x and high UHC and CO emissions [61; 104].

In the present non-premixed configuration NO_x, CO, CO_2, O_2 and UHC were measured. The emissions collection system is described in section 2.7. It was used to sample exhaust from non-premixed flames at two different flow conditions reported in Table 4.1: F3A1 and F3A2. Emissions data were collected by performing a traverse along the midsection of the enclosure exit at a distance of 140 mm from the bluff body. Ten points were taken during each traverse, approximately 10 mm apart.

In the literature, emission measurements are expressed in many different ways, which can make comparisons difficult and ambiguous. In this work the emission concentrations are corrected to a particular level of O_2 (15%) in the product stream. The aim of correcting to a specific O_2 level is to remove the effect of various degrees of dilution so that true comparisons of emission levels can be made at different overall equivalence ratios [104].

The collected emission results are presented in Figures 4.12, 4.13, 4.14. The x-abscissa denotes the radial position across the burner outlet (95 mm). In general

the NO_x, CO_2 and O_2 profiles are relatively flat at the combustor outlet. For CO and UHC, the profiles show a dip at the centreline (Fig. 4.12b and 4.14), indicating the inhomogeneous distribution of the species at the outlet. This could be due to the influence of the flow field within the combustor and to the mixture fraction distribution.

The NO_x emissions, shown in Fig. 4.12a, for lean fuel-air mixtures show rather low NO_x concentrations around 10-20 ppm corrected at 15% of O_2 content. Enriching the mixture from condition F3A2 (very close to the blow-off limit) to F3A1 causes a small increase in the nitrogen oxides production. Similar values of NO_x emissions for a non-premixed swirling flame were measured in the TECFLAM by Schmittel et al. [94].

As expected and reported in Fig. 4.12b, leaner flames (F3A2) tend to emit more CO, indicating incomplete combustion. This trend was already described by Lefebvre [61], when the non-premixed flame becomes overall leaner, the carbon monoxide increases due to a inadequate burning rates and due to too low fuel/air ratio and/or insufficient residence time (since the bulk velocity increased).

CO_2 and O_2 concentrations at the outlet are represented in Fig. 4.13. The trend is expected, approaching the blow-off condition the oxygen content at the exit increases while the CO_2 emissions decreases. The unburned hydrocarbon (Fig. 4.14) increases from condition F3A1 to F3A2 due to a decrease of the overall equivalence ratio and thus a higher degree of incomplete combustion.

Some emission data show a minimum close to the centre of the enclosure exit (radial position of 47.5 mm). This is likely due to the presence of the central recirculation zone, already described in the previous chapter. It retains a significant supply of combustion products towards the bluff body.

The present emission data could be useful for future comparisons with advanced combustion modelling.

4.6 Conclusions

The blow-off behaviour of swirling methane non-premixed flames has been visualized and analyzed. The measurements included visualisation of the blow-off transient with 5 kHz OH* chemiluminescence, which allowed a quantification

of the average duration of the blow-off transient. OH-PLIF images at 5 kHz for flames far from and close to extinction showed that the non-premixed flame intermittently lifts-off the bluff body, with increasing probability as the fuel velocity increases. The flame sheet shows evidence of localised extinctions, which are more pronounced as approaching blow-off. The measurements include blow-off limits and their attempted correlation. It was found that a previously proposed correlation based on a Damköhler number does a reasonable job at collapsing the dataset. The emissions of NO_x, CO, CO_2, O_2 and UHC have also been measured for the stable flames. The results show that NO_x has mole fractions lower than 20 ppm and that it decreases when the flame approaches the blow-off condition. In contrast CO and UHC increase as the flame approaches the blow-off. The results can help the development of advanced turbulent combustion models based on large-eddy simulation that have a promise of capturing combustion transients, such as the lift-off statistics and blow-off duration measured here.

4.7 Figures for chapter 4

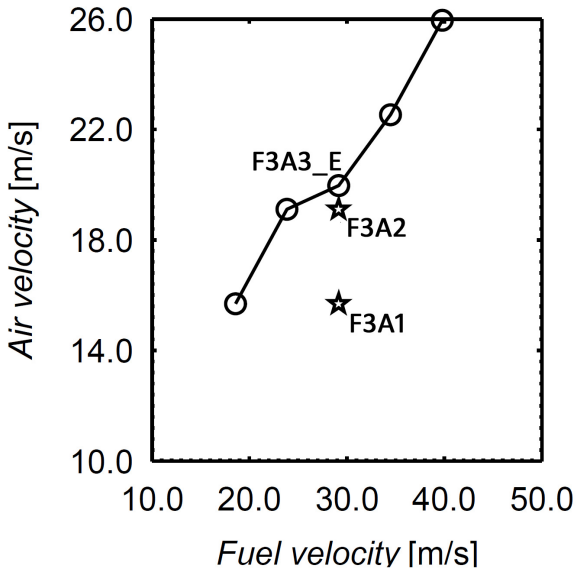

Figure 4.1: Air velocity at blow-off as a function of the fuel jet velocity for the non-premixed flame. The stars denote the stable flow conditions F3A1 and F3A2. The circle denotes the blow-off conditions and F3A3_E is also indicated.

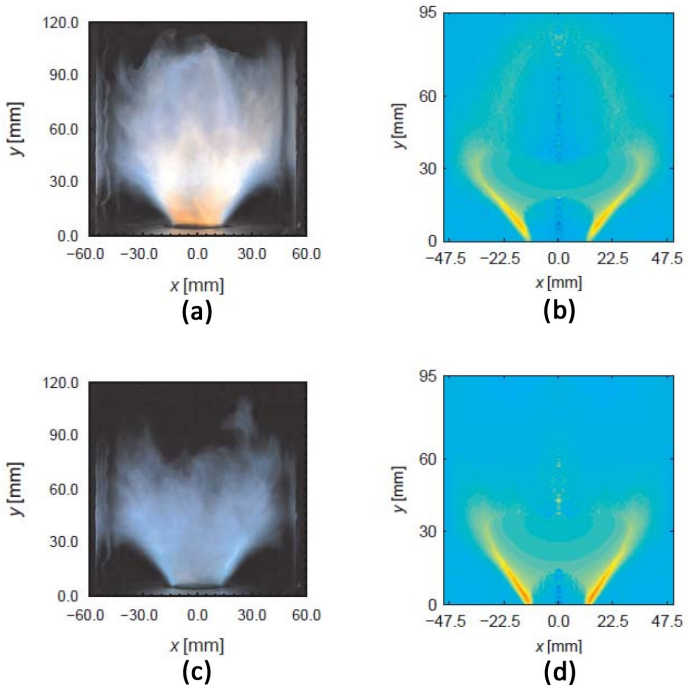

Figure 4.2: (a, c) Photographs of non-premixed flames F3A1 and F3A2. Corresponding Abel-transformed time-averaged OH* chemiluminescence images (b, d).

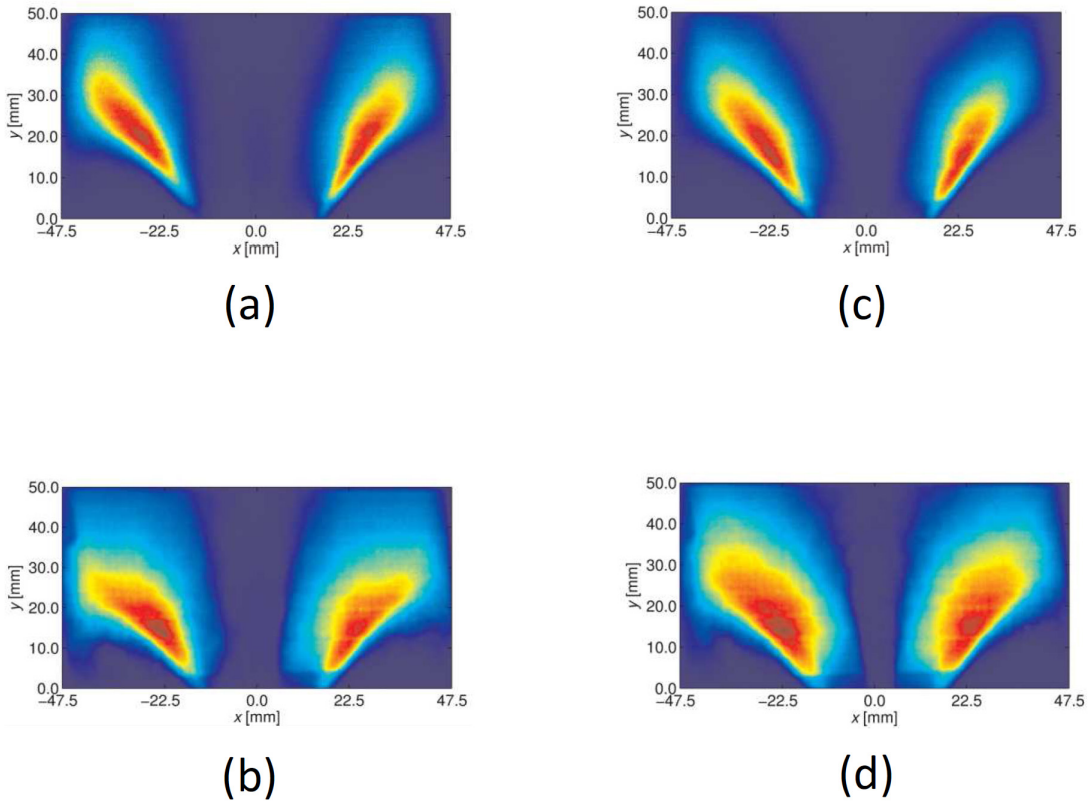

Figure 4.3: Images of the normalized mean (top row) and RMS (bottom row) of OH-PLIF for flames F3A1 (a, b) and F3A2 (c, d).

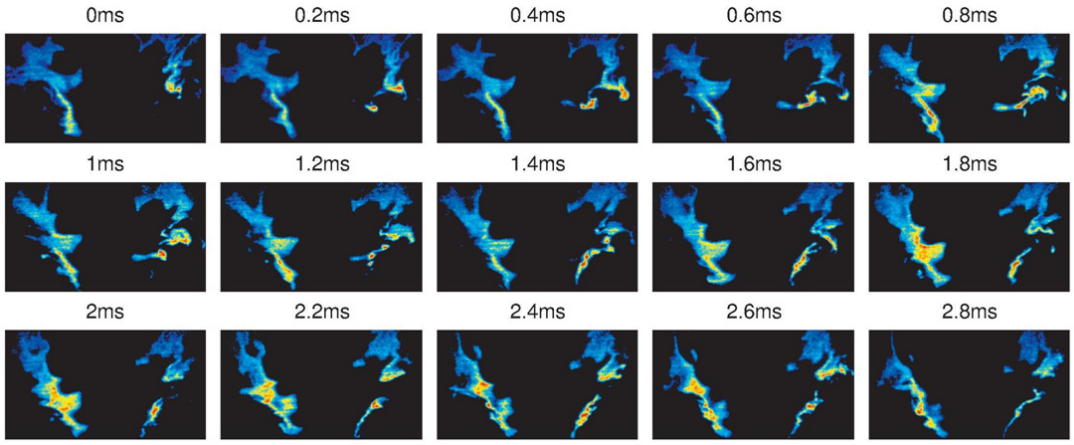

Figure 4.4: Sequence of instantaneous OH-PLIF images (corrected for laser sheet inhomogeneities) showing the temporal evolution of the flame at conditions far from blow-off, F3A1. Image size 50×95 mm. Colour scale varies from blue to red with increasing OH concentration.

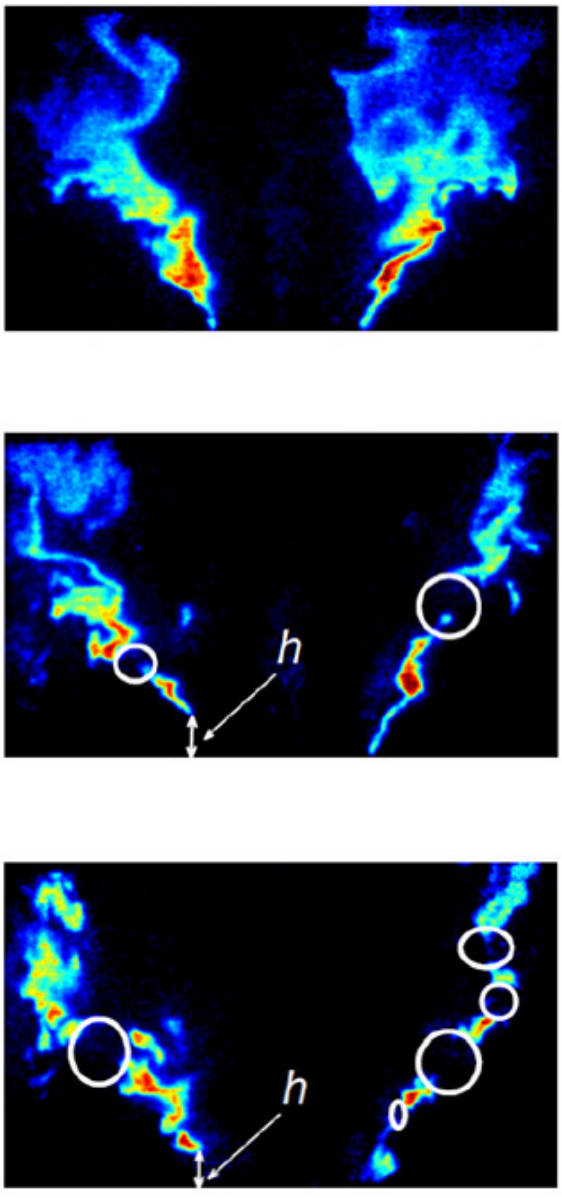

Figure 4.5: Independent OH-PLIF snapshots for non-premixed flames (image size 50×95 mm); from top to bottom: F3A1, F3A1, F3A2. The three instantaneous images are separated by a time delay.

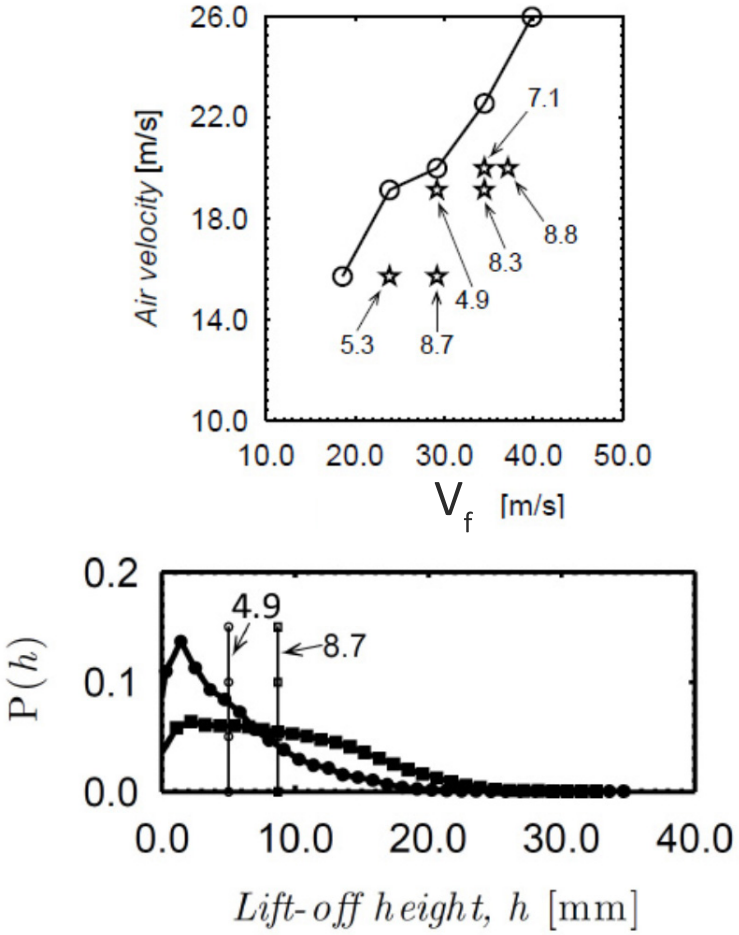

Figure 4.6: Upper: Air velocity at blow-off as a function of the fuel jet velocity for the non-premixed flame. The stars denote flames far from blow-off. The number denotes the mean lift-off height in mm. Lower: Probability density function of the lift-off height for the flow conditions: F3A1 (square), F3A2 (circle). The numbers indicated show the average lift-off height in mm.

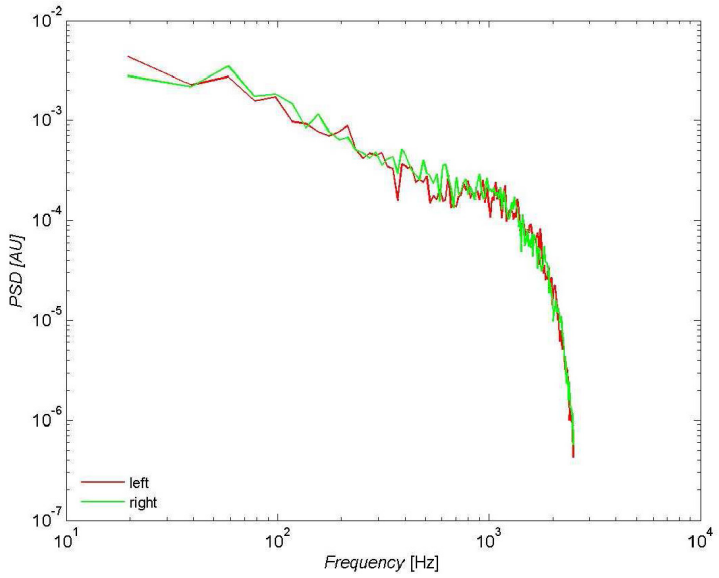

(a)

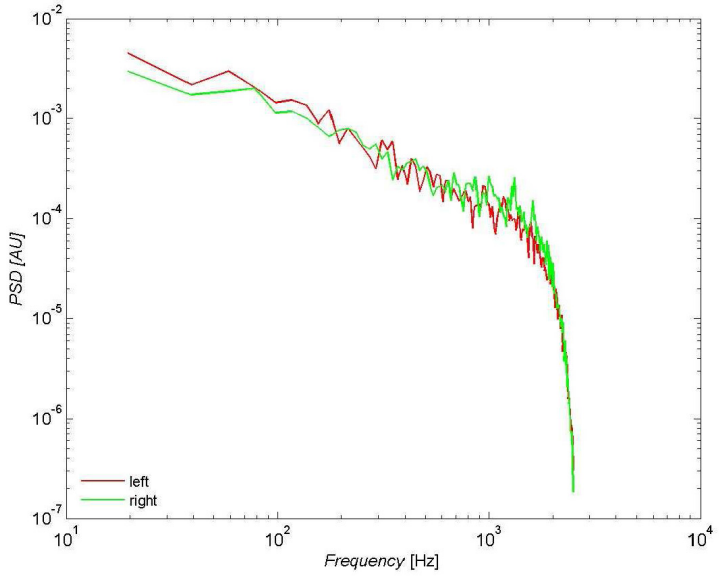

(b)

Figure 4.7: Spectra of OH obtained from the OH-PLIF timeseries for flames F3A1 (a) and F3A2 (b).The spectra were calculated at a distance of 2 mm from the bluff body along the shear layer in the right (r/d=1.45) and left part(r/d=-1.45) of the combustor.

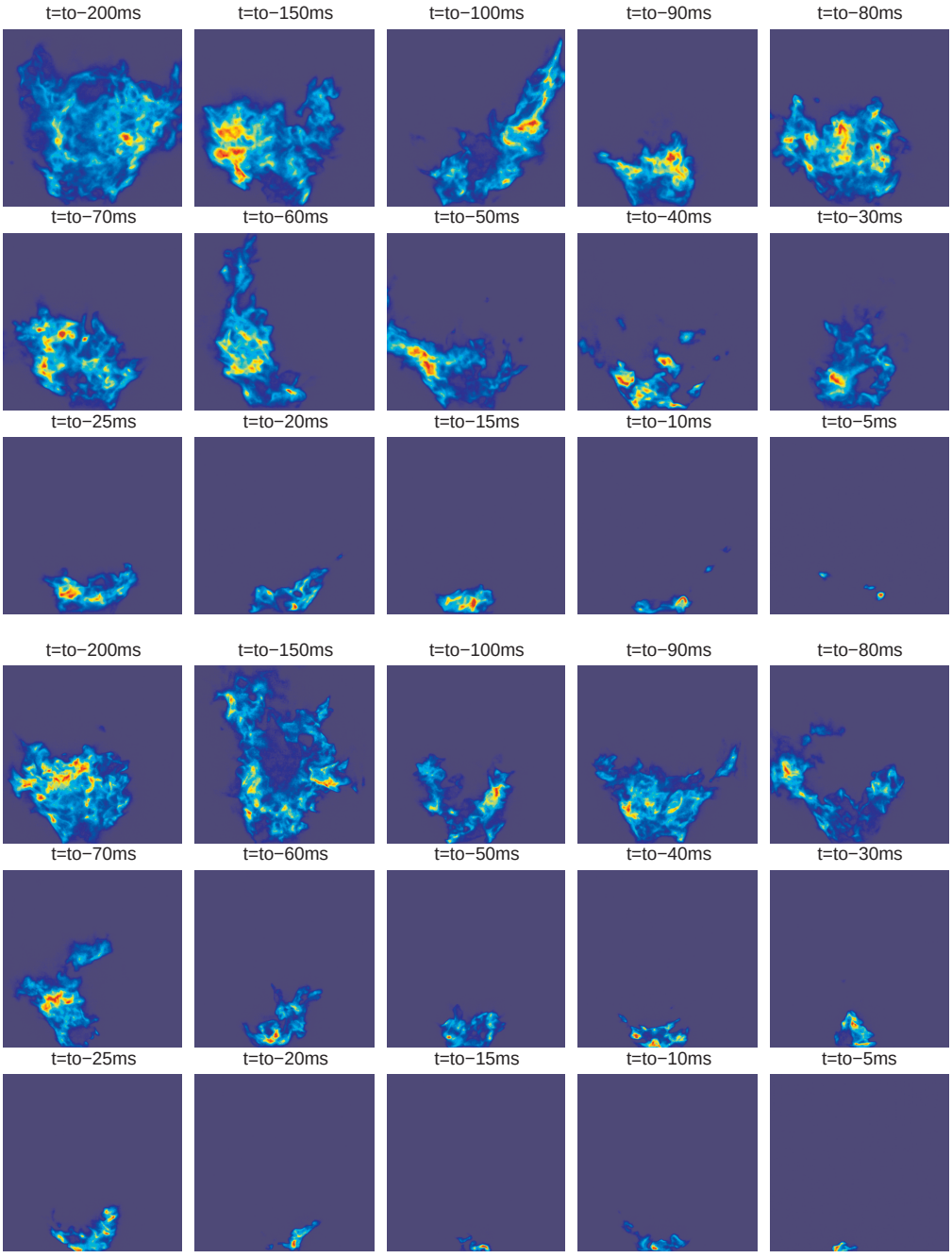

Figure 4.8: OH* chemiluminescence sequence of two independent blow-off events for the non-premixed flame $F3A3\_E$. Side view, flow comes from below, axis of the burner at the centre of the x range. Image size 90 × 90 mm.The sequence on the top has an extinction time of 29 ms. The sequence on the bottom has an extinction time of 71 ms.

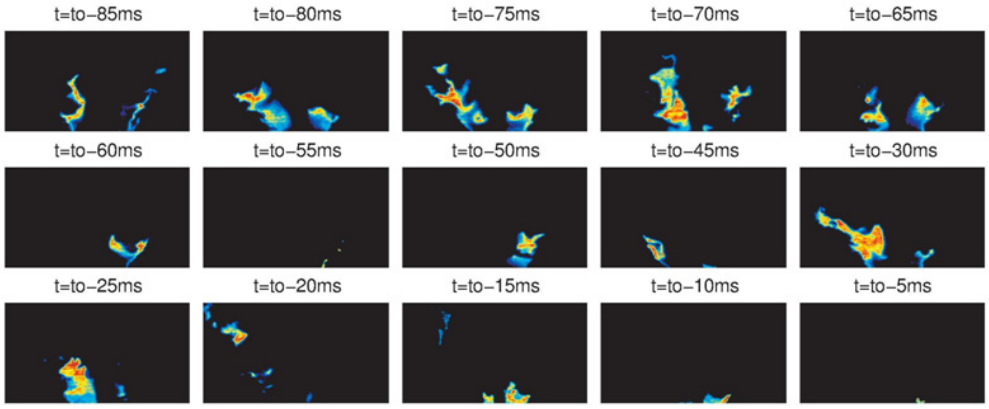

Figure 4.9: Sequence of instantaneous OH-PLIF images (corrected for laser sheet inhomogeneities) showing the temporal evolution of the structure of the flame during a blow-off event, $F3A3\_E$. Image size 50×95 mm. Colour scale varies from blue to red with increasing OH emission.

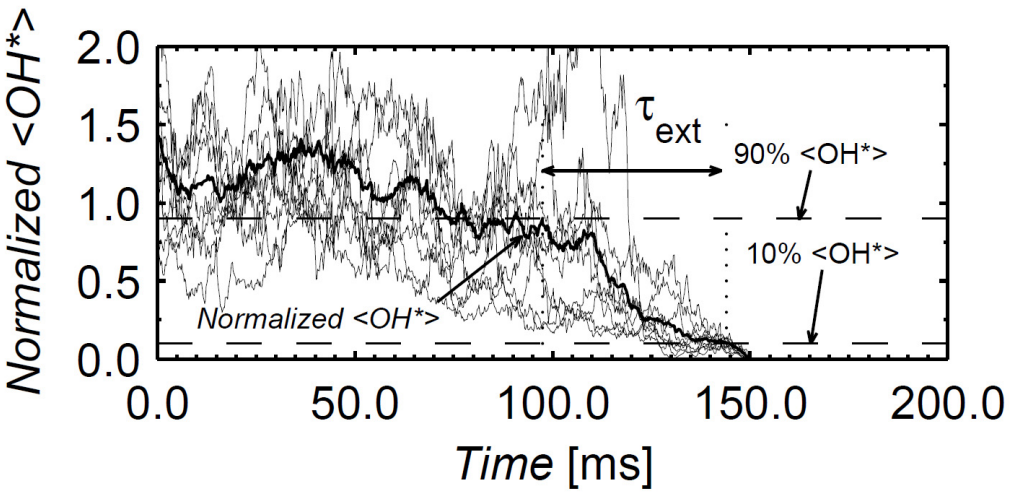

Figure 4.10: Average of area-integrated OH* time series (thick line), and area-integrated OH* from ten individual blow-off events (thin lines), each shifted to match the instant of extinction and normalized by its pre-extinction value. The definition of the average duration of the blow-off event, τ_{ext}, is indicated.

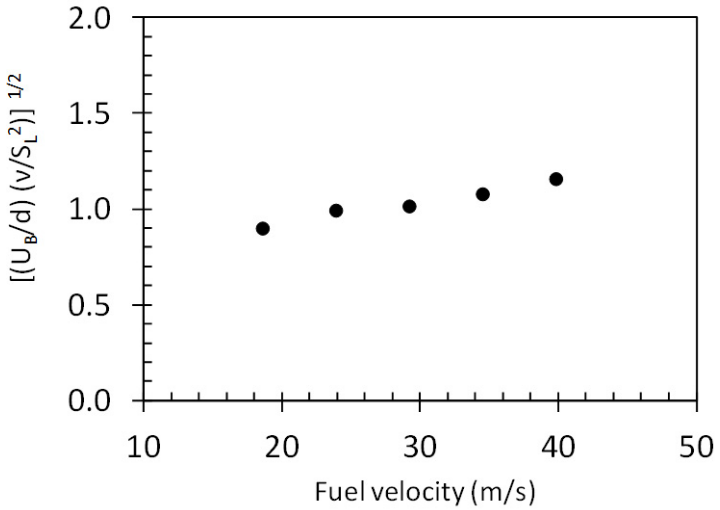

Figure 4.11: Evaluation of 1/Da $\left(\left[\left(\frac{U_b}{d}\right)\left(\frac{\nu}{S_L^2}\right)\right]^{1/2}\right)$ based on the extinction correlation proposed by Radhakrishnan et al. [89], as a function of the fuel velocity.

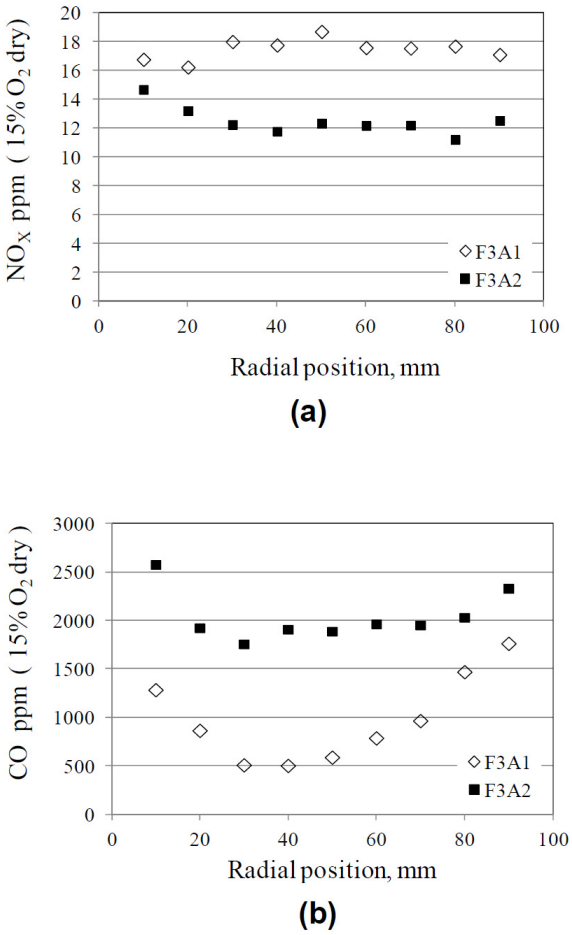

Figure 4.12: Dry NO_x mole fraction (a) and dry CO mole fraction (b) for F3A1 and F3A2 flow condition at 140 mm from the bluff-body.

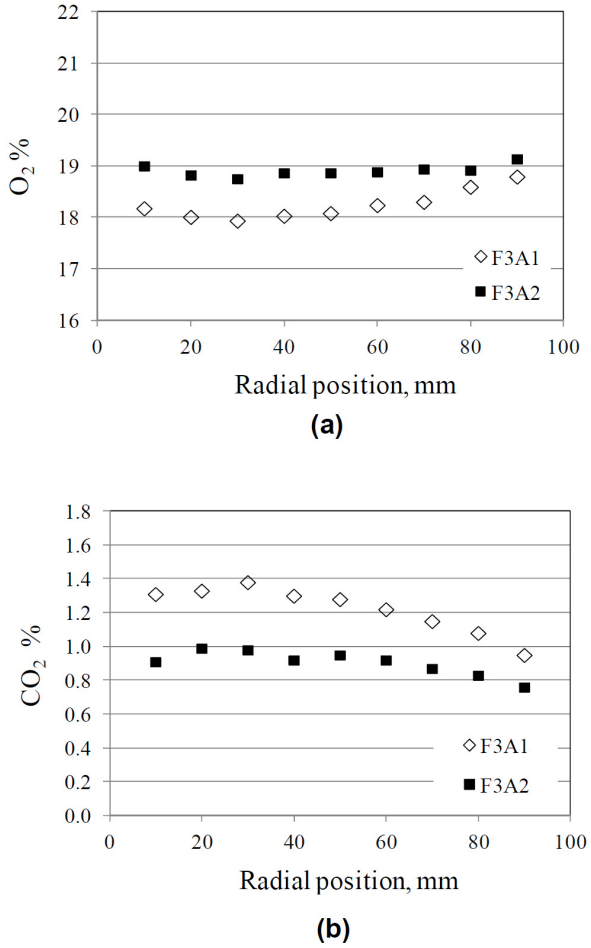

Figure 4.13: Dry O_2 mole fraction (a) and dry CO_2 mole fraction (b) for F3A1 and F3A2 flow condition at 140 mm from the bluff-body. The values are corrected to a 15 % level of O_2 in the dry product stream.

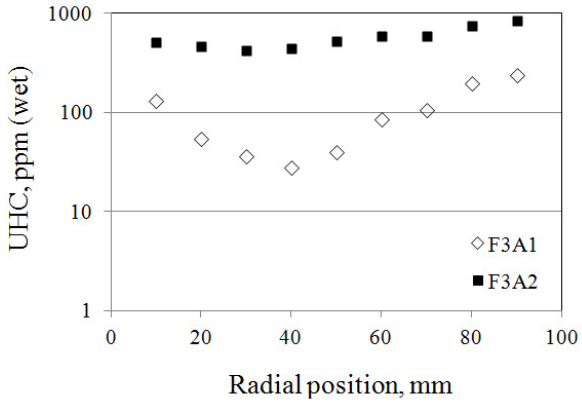

Figure 4.14: Wet UHC mole fraction for F3A1 and F3A2 flow condition at 140 mm from the bluff-body.

Chapter 5

Spray flame blow-off

5.1 Introduction

In this chapter stable conditions approaching blow-off and the blow-off transient of swirling heptane and decane spray flames are described. The measurements include blow-off limits, visualization of the blow-off transient with 5 kHz OH* chemiluminescence and OH-PLIF, and the quantification of the average duration of the blow-off transient. Several correlations for predicting the blow-off are examined and presented. The experimental set-up is described in Section 2.1.2. The results are presented and discussed in Section 5.4, with the chapter closing with the conclusions.

5.2 Motivation

In the past, neither the blow-off limit prediction nor the exact nature of the blow-off transient have been investigated in detail for spray flames. Although some empirical correlations for the blow-off limit exist [61; 75], these have not been thoroughly validated. The progression from localized to global extinction in spray jet flames has only recently been studied [70], while there have been no experiments to the author's knowledge on the quantification of the duration of the blow-off transient in spray flames with swirl.

This chapter aims: (i) to present how the flame shape changes when the blow-

off is approached by increasing the air flow rate; (ii) to discuss the applicability of available correlations for the blow-off limit for spray flames; and (iii) to quantify the duration of the blow-off transient.

5.3 Methodology

The burner used is that developed by Marchione et al. [68] and described in section 2.1.2. The structure of the flame approaching blow-off was investigated at three conditions using n-heptane as liquid fuel, starting from a stable condition (SWH0) to just prior to the blow-off event (SWH2). These conditions are given in Table 5.1. At each stable flame condition, the flame shape was investigated by acquiring five data sets, each consisting of 1000 images sampled at 5 kHz, which were then stored for post processing. Further increasing the air flow rate from this stable conditions at SWH3 leads to the blow-off condition (U_{BO} = 18.1 m/s, ϕ_{BO} = 0.14). The determination of the blow-off condition for the spray flame was done by fixing the fuel flow rate and then increasing the air flow rate in steps of approximately 0.258 m/s every 20 seconds until extinction occurred. The blow-off condition and a single stable flame have been also investigated with a less volatile liquid fuel, n-decane. The flow conditions for these further cases are reported in Table 5.1.

Table 5.1: Test cases evaluated for various stable and blow-off conditions of the spray flames.

Fuel type	Name	Case	Fuel flow rate [g/s]	U_{bulk} [m/s]	ϕ_{ov}
N-heptane	SWH0	Stable	0.12	11.4	0.22
N-heptane	SWH1	Stable	0.12	14.8	0.17
N-heptane	SWH2	Stable	0.12	16.5	0.155
N-heptane	SWH3	Blow-off	0.12	18.1	0.14
N-decane	SWD1	Stable	0.2	15.9	0.26
N-decane	SWD3	Blow-off	0.2	25.1	0.167

5.4 Results and Discussion for n-heptane flames

In this section, instantaneous and time averaged images, temporal sequences and measurements of the blow-off transient are presented and discussed for spray flame using n-heptane as liquid fuel. The section concludes with the discussion of several correlations to predict the blow-off and with the emission measurements of stable flames at different conditions

5.4.1 Stability limits

Figure 5.1 shows the stability limits of the spray flames. The air velocity at blow-off increases at first with increasing fuel flow rate, but levels-off at high fuel flows, so that above a certain value, U_{BO} becomes independent of fuel flow rate. It is possible that the flat behaviour of the spray flame in the narrow flow rate range considered depends on the atomization quality. The initial small increase could be due to a better behaviour of the atomization in the pressure swirl atomizer.

Correlating this data will be discussed later. The flames studied by the diagnostics (SWH0, SWH1, SWH2, SWH3) are shown by triangles.

5.4.2 Flame shape

In Fig. 5.2 direct photographs of the spray flame at conditions SWH0 to SWH2 show that high soot regions, indicated by the orange emission, decrease in size as the blow-off condition is approached, and that the spray flame close to the lean blow-off limit is mostly blue (Fig. 5.2c).

Figure 5.3 reports the average Abel-transformed OH* chemiluminescence image which shows the reaction zone location in spray flames at conditions far from the extinction limit (Fig. 5.3a), and approaching blow-off (Fig. 5.3c). The reaction zone in the stable condition (Fig. 5.3a) has a conical shape and a height about $1.2d$ (d is the diameter of the bluff body). The inner cone corresponds to the stabilization of the flame along the spray cone, while the outer "legs" of the flame are attached to the bluff body edges and follow the shear layer between the annular air injection and the central recirculation zone. For the lower velocity flame, these outer legs are fainter than for the high velocity flames. When the air

flow rate increases (Fig. 5.3b), the length of the flame decreases and the intensity of the OH* emission becomes brighter. Approaching the blow-off condition, the flame height further decreases to about $1d$ and the flame remains anchored on the bluff body (Fig. 5.3c). The OH* intensity decreases along the inner flame zone, but high chemiluminescence intensity is observed along the outer flame. The change in flame shape as blow-off is approached seems to be less drastic than for fully premixed flames, as reported by Kariuki et al. in an experimental study in a similar geometrical configuration [52; 53], possibly because the spray cone angle determines to a large extent the location of the flammable mixture fractions, and hence flame shape.

5.4.3 Flame behaviour approaching blow-off

The fast OH-PLIF system was used to investigate the temporal behaviour of the spray flame for the three flow conditions: SWH0, SWH1, SWH2. Measurements of OH-PLIF approaching the blow-off condition, shown in Fig. 5.4, validate observations from the chemiluminescence images about the length of the flame. A characteristic feature is the more evident flame branch along the spray cone. It is more clearly seen in Fig. 5.5c-d that shows the mean OH-PLIF image superimposed on the mean Mie scattering image (shown also separately in Fig. 5.6 for the three flow stable conditions).

For the spray flame, high OH mostly envelopes the high Mie regions. Note the quite significant distance between the outer wing of the flame stabilised on the bluff body and the spray, indicating fuel vapour only combustion there, and the absence of droplets in the RZ except for the immediate vicinity of the injector, up to about z=45 mm. This agrees with the absence of LDA signal beyond this axial location discussed in the section 3.2.2.

In Fig. 5.6 the average images of Mie scattering only at the three different flow conditions (SWH0, SWH1, SWH2) are reported. Determination of the spray cone angle is performed by detecting the spray edges of the Mie scattered spray images (averaged of 5000 instantaneous images). As blow-off is approached, the spray angle becomes slightly wider, with an inner angle of around 80°, presumably due to the higher velocity of the recirculating air, but very few droplets impinge

on the enclosure or are found downstream of $z \approx 45$ mm, as reported in Fig. 5.5c. Since the Mie and OH-PLIF measurements were not done simultaneously it is not possible to extract flame structure information of the type achieved in Ref. [70].

Figure 5.7 shows individual OH-PLIF snapshots for the three flow stable conditions. At conditions far from blow-off, the reaction zone appears contorted. The spray flame shows a relatively continuous OH sheet, which is in general thinner than that of the methane flame. The outer flame wing lifts-off the bluff body randomly, and when it does, the lift-off height is less than for the non-premixed flame (discussed in the next sub-section). The central part of the flame shows occasional breaks, but less than for the non-premixed flame. In Fig. 5.8 three independent OH-PLIF snapshots are shown, where the lift-off height (h) is more evident and it is indicated. Significant fragmentation is also observed (see, for example, bottom Fig. 5.8).

5.4.4 Lift-off height statistics

In this Section, the lift-off height h is quantified for various conditions as already performed for the non-premixed gaseous case in the previous chapter. Detachment from the attachment point was investigated by evaluating the gradients of OH of the instantaneous OH-PLIF image corrected for laser sheet inhomogeneities. A suitable threshold was then chosen to filter out low gradients of OH, which were observed not to overlap with the boundary of the high OH regions. The separation distance from the bluff body edge to the high gradient of OH regions was evaluated, and is here referred to as the lift-off height.

The mean values of the lift-off height, $\langle h \rangle$, have been calculated based only on images that show lift-off, and these values are indicated on Fig. 5.9, together with the probability of finding a lifted flame, P_{lift} (defined as the ratio of the number of images with lift-off to the total number of images; the left and right branches of the flame in each individual snapshot are considered as two different samples). Figure 5.9 shows the pdfs of the lift-off height measured from the OH-PLIF movies, conditional on $h > 0.2$ mm. Similarly to the non-premixed gaseous case, a wide pdf is observed, with a long positive tail.

The spray flame is lifted much less than the gaseous case and $\langle h \rangle$ is only around 2 mm and depends less on the operating condition. The probability of finding a lifted flame is less than for the methane flame. A maximum $\langle h \rangle$ of 6 mm occurs at the highest fuel flow rate studied (0.26 g/s), where the spray flame is very close to the blow-off limit. The $\langle h \rangle$ evaluated in the fuel flow rate range of 0.09-0.12 g/s varies between 2 and 3.3 mm. For the same air velocity, the probability of finding a lifted flame at low fuel flow rate (0.1 g/s) is higher compared to the values at a fuel flow rate of 0.12 g/s as reported in Fig. 5.9. For the same fuel flow rate, the probability of lift-off decreases as the air velocity increases. The intermittent re-attachment of the flame does not follow a particular frequency, as concluded by the lack of any peaks in the spectrum of the OH-PLIF signal, as for the non-premixed flames.

From the instantaneous images of OH-PLIF, Fig. 5.7 and 5.8, the luminous regions near the attachment point take high values of OH. Also, a separation from the bluff body edge is clearly visible as the OH level drops sharply from the lifted reaction zone to the zero level of the non-luminous regions. Subsequently, the boundaries of the luminous regions are typically associated with large gradient of OH values, and the lift-off height measurements evaluated were observed to have little sensitivity on the chosen OH gradient threshold.

5.4.5 Blow-off transient and its duration

Further increasing the air flow rate from conditions SWH2 leads to the blow-off condition, SWH3. The flame shape and reaction zone behaviour during the extinction transient were captured using the fast OH* chemiluminescence and OH-PLIF imaging systems.

Figures 5.10 and 5.11 show spray flame blow-off events from the side and the top respectively by OH* chemiluminescence recording. The flame progressively gets diminished in size, while remaining anchored at the bluff-body edges. As for the non-premixed gaseous case, the blow-off event occurs inside the RZ just a few mm above the bluff-body. Towards the end of the process, flame fragments seem to remain aligned with the spray cone and the last flame element to survive is always somewhere close to the spray inside the RZ. From the top view, it is evident

that the flame shrinks from all sides and the last remaining flame element seems to be off-axis. The flame disintegration process lasts some tens of milliseconds. In Fig. 5.12, the same qualitative behaviour of the reaction zone is confirmed using the fast OH-PLIF imaging system.

Several blow-off transients, captured with fast imaging (5 kHz) of OH* chemiluminescence, were used to quantify the duration of the blow-off transient as for the non-premixed gaseous case described in the previous chapter. The emission from each image was integrated, which then gave a time series of the area-integrated OH*. Each of these time series was time-shifted such that extinction occurred at an arbitrarily chosen time, here denoted as t_0. The OH* was then averaged over time from the beginning of the time series until the start of the decay to zero, and this average value was used to normalize each corresponding time series, Fig. 5.13. Hence for each blow-off event, we obtain a time series of the normalised, time-shifted, area-integrated OH* chemiluminescence that shows a relatively steady condition with finite emission before blow-off and a transition to zero emission. Many such time series, from different blow-off events at similar conditions, were then averaged. This gives the average behaviour of the blow-off event. Then, this average signal $\langle OH^* \rangle$ was examined closely to quantify the duration of the blow-off event, τ_{ext}. This was defined as the time needed for the emission to decrease from 90% to 10%. The spray flame shows an extinction time of 12 ms, that normalized with d/U_b gives a value of about 10. Thus, the extinction time of the spray n-heptane flame is shorter of the extinction time measured in a turbulent non-premixed gaseous case described in Section 4.5.5.

The blow-off event is therefore a relatively slow process. This suggests that control measures, such as fast fuel injection, coupled with appropriate detection, such as with chemiluminescence monitoring, may have a reasonable chance of success in keeping the flame alight very close to the blow-off limit.

5.4.6 Blow-off correlation

The equations derived by Ballal and Lefebre [12] for predicting the extinction limits have been fully presented in section 1.2.3. They developed a correlation for premixed turbulent flames, also used in the prediction of the extinction equiva-

lence ratio for liquid-fuel air mixtures if the rate of fuel evaporation is sufficiently high to ensure that all the fuel is fully vaporized. The attractiveness of these correlations is that they provide a relationship of how several parameteres (pressure, temperature) influence the blow-off limits. The validity of this proposed model for determining the equivalence ratio when the blow-off occurs is tested in the present work by comparing the measured values of extinction equivalence ratio (ϕ_{ext-m}) with the corresponding predicted values (ϕ_{ext-c}) from equation [12]:

$$\phi_{ext-1} = 1.2 \left[\frac{m_{Air}}{P^{1.25}\ V\ \exp(\mathrm{T_{inlet}}/150)} \right]^{0.16} \tag{5.1}$$

where m_{Air} is the air mass flow rate, P the operating pressure, T_{inlet} is the inlet temperature of the reactants and V is the volume of the combustion zone, considered here as the volume within the quartz enclosure.

The calculated values from equation 5.1 are plotted in Fig. 5.14a, in which all measured values of ϕ_{ext} obtained over a narrow range of fuel flow rate are plotted against corresponding calculated values. The level of agreement of this correlation is not very satisfactory. It does not accurately predict the behaviour of the extinction equivalence ratio measured for values of $\phi > 0.13$. If the fuel does not fully vaporize a more complex correlation was developed for predicting the extinction equivalence ratio [12], it was developed including the SMD (D_{32}) and the turbulent intensity (I_u):

$$\phi_{ext-2} = 0.02 \left[\frac{m_{Air}}{P^{1.25}\ V\ \exp(\mathrm{T_{inlet}}/150)} \right]^{0.16} \left[\frac{\rho_f}{\rho_g\ V\ \log(1+\mathrm{B})} \right] \left[\frac{m_{Air}\ D_{32}^3\ A}{(I_u/100)\ \mu_g} \right]^{0.5} \tag{5.2}$$

In this correlation the percentage turbulent intensity (I_u) is defined as the ratio of the RMS velocity and the mean velocity. It is estimated from the LDA results presented in section 3.1.1. ρ_f and ρ_g are respectively the densities of the liquid fuel and the air at the inlet conditions. A is the area of the combustion zone. The Sauter mean diameter was estimated equal to 40 μm. This value was not measured in the present work, but it is taken from Marchione et al.

[68], where the authors used the same type of atomizer with similar fuel flow condition. In Fig. 5.15 a comparison of the measured values of extinction with the corresponding predicted values from 5.2 is reported, three different D_{32} have been used: 20 , 40 and 80 μm. The prediction of the extinction is improved by using a sauter mean diameter equal to 40 μm.

A comparison of the measured values of extinction equivalence ratio (ϕ_{ext-m}) with the corresponding predicted values (ϕ_{ext-c}) from equation 5.2 is reported in Fig. 5.14b. Here, the prediction of the extinction equivalence ratio is improved compared to the previous correlation (equation 5.1). An unaccuracy of 35% is observed for high values of fuel flow rate.

For baffle-stabilized flames the role of turbulence is more complex because it affects not only the rate of fuel evaporation, but also the rate of entrainment of air into the wake region [12]. For this type of configuration the extinction equivalence ratio is given by [12]:

$$\phi_{ext-3} = \left[\frac{0.00003\ \rho_f}{d\ \log(1+\mathrm{B})}\right]\left[\frac{U D_{32}^3(1+0.12I_u)}{\rho_g\ \mu_g\ (T_u/100)B_g(1-B_g}\right]^{0.5} \left[\frac{U\ (1+0.12T_u)}{P^{0.25}\ d\ (1-B_g)T_{inlet}\exp(\mathrm{T_{inlet}}/150)}\right]^{0.16} \tag{5.3}$$

Predictions of extinction equivalence ratios based on the above equation show good agreement with the corresponding experimental values as reported in Fig. 5.14c. But including new parameter as the blockage ratio (B_g) and the diameter of the bluff body (d) does not improve the prediction of the extinction compared to the previous correlation in Eq. 5.2.

Plee and Mellor [86] developed one the most advanced empirical timescale correlations for the prediction of the extinction in spray flames. It is fully described in Section 1.2.3. Four characteristic times are expected to be important: the mixing time (τ_{sl}), the fuel injection time (τ_{fi}), the evaporation time (τ_{eb}) and the ignition delay time (τ_{hc}). Testing different configurations and fuels, Plee and Mellor [86] developed the following equation to predict the extinction:

$$\tau_{sl}\ + 0.12\ \tau_{fi} = A_1\ (\tau_{hc}\ +\ 0.011\ \tau_{eb})\ +\ A_2 \tag{5.4}$$

When the left hand side of equation 5.4 is equal or smaller than the right hand side, blow-off can occurs. Or, in other words, when the fluid mechanical time (composed by τ_{sl} and τ_{fi}) is higher than the chemical/evaporation times, the flame is stable and blow-off will not occur. In the present work at the blow-off point, τ_{sl} is equal to the ratio of the diameter of the bluff body and the blow-off velocity measured. τ_{fi} is equal to $\tau_{eb}(T/T_{inlet})/U_{fuel}$ where U_{fuel} is the velocity of the liquid fuel at the inlet. The evaporation time (τ_{eb}) is equal to D_{32}^2/λ. As in the previous correlation D_{32} is estimated to be equal to 40 μm, while the evaporation constant λ is taken by Lefebvre [60]and it is equal to 0.97 mm^2/s. Plee and Mellor [86] estimates the ignition delay time from the empirical following equation:

$$\tau_{hc} = \frac{T}{T_{inlet}} \frac{e^{21000/RT}}{\phi} 10^{-4} \tag{5.5}$$

In Fig. 5.16 the characteristic times are represented in the same way of the original paper [86]. The black line represents the original correlation of Plee and Mellor [86] where two empirical coefficients (A_1= 2.12 and A_2= 0.095) were used to collapse all experimental data. In the present work, the empirical coefficients are changed to collapse all data along the dashed line reported in Fig. 5.16. In the present spray case, the extinction will occur when:

$$\tau_{sl} \ + 0.12 \ \tau_{fi} \leq 0.653 \ (\tau_{hc} \ + \ 0.011 \ \tau_{eb}) \ + \ 0.95 \tag{5.6}$$

The experimental conditions under the dashed line in Fig. 5.16 will be stable flames, while over the line the blow-off occurs. However, the use of different empirical coefficients makes this predicting model highly dependent on empirical data and on the geometrical configuration applied. A general use of the Plee and Mellor correlation to new configurations is limited by a preliminary experimental campaign to find the right empirical coefficients.

The correlation of Radhakrishnan et al. [89], already tested for the non-premixed gaseous case in the previous chapter, is here used for the first time on a spray case. Eq. 1.8 is employed for the spray blow-off data using S_L at stoichiometry (0.39 m/s, taken from the data of Davis and Law [36]) and ν evaluated for the gaseous phase at a temperature halfway between the reactants

and the adiabatic flame temperature, as suggested by Mellor [75].

The resulting values of the group $\left[\left(\frac{U_b}{d}\right)\left(\frac{\nu}{S_L^2}\right)\right]^{1/2}$ for the spray flame blow-off are shown in Fig. 5.17. The values lie in the range 0.87 to 0.99 for the spray flames. The scatter is considerably smaller than the scatter generally observed in the literature [75; 89; 96] and with the other correlations described here. Note that values around unity have also been reported for fully premixed non-swirling flames [89] and for the non-premixed flames of this thesis (Fig. 4.11).

In Fig. 5.18 the Damköhler correlation of Radhakrishnan et al. [89] has been reported for the two combustion regimes of this work and for a premixed case in the same geometrical configuration [52].

For the fuel air ratio considered the Damköhler number do a reasonable job at collapsing all datasets in the range 0.7-1.5.

The success of this Damköhler correlation [89] to correlate the blow-off point is of some practical relevance, as it implies that it can be tried for other configurations too, but it cannot be used to imply that locally the non-premixed and the spray flame are indeed of premixed character. The OH-PLIF images in Chapter 3 and 4 showed thin, fragmented flame sheets, similar to the jet non-premixed flames with strong local extinctions [50; 101] and therefore let us assume that the present non-premixed and spray reaction zones follow approximately the stoichiometric contour and extinguish where the local scalar dissipation is high. This is the common wisdom of extinction of a non-premixed flame. In this picture, one can attempt to build a global blow-off correlation as follows. Peters and Williams [83] postulated that extinction of the turbulent flame will occur when the mean scalar dissipation evaluated at the mean stoichiometric mixture fraction isosurface, χ, is greater than the critical value, χ_{ext}, for the extinction of a laminar opposed-jet diffusion flame. This concept has been shown to produce good predictions of turbulent opposed-jet non-premixed flame extinction [74], but it has not been generally applied to flames of more complicated geometry or for spray flames. The mean scalar dissipation can be modelled as $\chi = 2u'/L_t\xi'^2$, where ξ'^2 is the variance of the mixture fraction at the mean stoichiometric isosurface. A theoretical result for the critical scalar dissipation at stoichiometry of a laminar

flame is given as [82].

$$\chi_{ext} = \frac{\xi_{st}^2(1-\xi_{st})^2}{\frac{\nu}{S_L^2}} \tag{5.7}$$

For example, for methane ($\xi_{st} = 0.0554, S_L = 0.38\ m/s$), we get $\chi_{ext} = 26.3\ 1/s$, which is to be compared to about 28 $1/s$ from a laminar flamelet calculation with the GRI 3.0 scheme, while for heptane ($\xi_{st} = 0.062, S_L = 0.39\ m/s$), we get $\chi_{ext} = 34.3\ 1/s$ which is to be compared to about 52 $1/s$ as found from a laminar flamelet calculation with the scheme of Held et al. [43]. Considering the uncertainties involved in capturing the extinction conditions with detailed mechanisms, we could argue that Eq. 5.7 underpredicts the critical scalar dissipation but by approximately a constant factor for all fuels. Note that in Eq. 5.7 ν is to be evaluated at the cold, reactants condition. The extinction criterion then becomes:

$$2\frac{C_1}{C_2}\frac{\xi'^2}{\xi_{st}^2(1-\xi_{st})^2}\left(\frac{U_b}{d}\right)\left(\frac{\nu}{S_L^2}\right) > C \tag{5.8}$$

where C is some constant (of order unity, as postulated by Peters and Williams [83] based on an insightful percolation theory). Assuming that ξ' at the mean stoichiometric isosurface is not too far from ξ_{st} (based on CFD of the present flow; see Ref. [106]), then it becomes evident that, by comparing with Eq. 1.8 the scalar dissipation based extinction criterion is consistent with both the Radhakrishnan et al.' s [89] postulate and with the strain-rate based correlation of Ref. [102]. More extensive use of Eq. 5.8 would necessitate estimates of ξ'^2 which are very difficult to makein the absence of experimental data for ξ or detailed CFD solutions.

5.4.7 Emission measurements

In the present configuration NO_x, CO, CO_2, O_2, UHC mole fractions have been measured. NO_x, CO, CO_2, O_2 on dry basis, while UHC on wet basis. The emissions collection system is described in section 2.7. It was used to sample exhaust from two spray stable flames at different flow conditions reported in Table 5.1: SWH1 and SWH2. Emissions data were collected by performing a

traverse along the midsection of the enclosure exit. Ten points were taken during each traverse at a distance of 140 mm from the bluff body, approximately 10 mm apart. As already described in the non-premixed gaseous case, the concentrations of NO_x and CO are corrected to a particular level of O_2 (15%) in the product stream.

The collected emission results are presented in Figures 5.20, 5.19. The abscissa denotes the radial position across the burner outlet (95 mm). In general all emissions profiles are relatively flat at the combustor outlet. As expected approaching the blow-off from condition SWH1 to SWH2, the O_2 mole fraction increases (Fig. 5.19), while the CO_2 decreases since the overall equivalence ratio is decreased and the flame is overall leaner. As reported in Fig. 5.20a, the NO_x concentrations are around 9 ppm corrected at 15% of O_2 content, and they are rather similar for the two considered flow conditions. The carbon monoxide slightly decreases when the flow condition is closer to blow-off as shown in Fig. 5.20b. Both CO and UHC are the products of incomplete combustion. Given sufficient time and at high enough temperatures, these two pollutants would be further oxidized to carbon dioxide and water. In the two flow conditions examined, the unburned hydrocarbon emissions are high indicating that the combustion is incomplete (Fig. 5.21). The UHC profiles do not show a homogeneous distribution at the outlet as observed in Fig. 5.21. This could be due to the influence of the droplet distribution within the combustion chamber. In fact as observed in Fig. 5.6, where the average images of spray Mie scattering at the three different flow conditions (SWH0, SWH1, SWH2) are reported, the spray injection has a wide angle and no droplets are present within the central recirculation at an height over 40 mm.

This emission data can be useful for future comparisons with advanced computational models.

5.5 Results and Discussion for n-decane flames

In this section, instantaneous and time averaged images, temporal sequences and measurements of the blow-off transient are presented and discussed for spray flame using decane as liquid fuel. N-decane has a higher boiling point and a higher density than n-heptane as reported in Table 2.2. A stable flow condition

SWD1 and a blow-off transient condition SWD3 will be discussed. The flow condition values are reported in the Table 5.1.

5.5.1 Stability limits

Figure 5.22 shows the stability limits of the spray flames using n-decane as liquid fuels. The air velocity when the blow-off occurs increases at first with increasing fuel flow rate, but levels-off at high fuel flows (over 0.24 g/s), so that above a certain value, U_{BO} becomes independent of fuel flow rate, similar to the n-heptane flame. Correlating this data will be discussed later.

5.5.2 Flame shape

A photograph of the decane flame at stable condition SWD1 is shown in Fig. 5.23. High soot regions similar to the heptane case are visible. The length of the flame is around 30 mm and a conical shape is observed with a maximum width of 60 mm.

The reaction zone location was also revealed by measurements of OH-PLIF at the same stable condition (SWD1), reported in Fig. 5.24. It validates observations from the direct photography about the length of the flame. A characteristic feature is the more evident flame branch along the spray cone. The reaction zone has a conical shape and a height about $1.2d$ (d is the diameter of the bluff body). The inner cone as for the n-heptane flame corresponds to the stabilization of the flame along the spray cone, while the outer "legs" of the flame are attached to the bluff body edges and follow the shear layer between the annular air injection and the central recirculation zone.

5.5.3 Blow-off transient and its duration

Further increasing the air flow rate from conditions SWD1 leads to the blow-off condition, SWD3. The flame shape and reaction zone behaviour during the extinction transient was captured using the fast OH* chemiluminescence and OH-PLIF imaging systems.

Figures 5.25 shows a flame blow-off events from the side by OH* chemiluminescence recording. The behaviour of the extincion transient is very similar to the previous case where n-heptane was used as fuel .The flame progressively gets diminished in size, while remaining anchored at the bluff-body edges. The blow-off event occurs inside the RZ just a few mm above the bluff-body. Towards the end of the process, flame fragments seem to remain aligned with the spray cone and the last flame element to survive is always somewhere close to the spray inside the RZ. The flame disintegration process lasts some tens of milliseconds. In Fig. 5.26, the same qualitative behaviour of the reaction zone is confirmed using the fast OH-PLIF imaging system. Thus, the blow-off transient of the spray flame is quite similar for the two liquid fuel used in this work (heptane and decane). It occurs above the bluff body and the last flame element is quite close to the atomizer for both cases.

Several blow-off transients, captured with fast imaging (5 kHz) of OH* chemiluminescence, were used to quantify the duration of the blow-off transient as for the non-premixed gaseous case and the spray heptane case described in the previous sections. The emission from each image was integrated, which then gave a time series of the area-integrated OH*. Each of these time series was time-shifted such that extinction occurred at an arbitrary chosen time, here denoted as t_0. The OH* was then averaged over time from the beginning of the time series until the start of the decay to zero, and this average value was used to normalize each corresponding time series, Fig. 5.13. Hence for each blow-off event, we obtain a time series of the normalised, time-shifted, area-integrated OH* chemiluminescence that shows a relatively steady condition with finite emission before blow-off and a transition to zero emission. Ten time series, from different blow-off events at similar conditions, were then averaged. This gives the average behaviour of the blow-off event. Then, this average signal $\langle OH^* \rangle$ was examined closely to quantify the duration of the blow-off event, τ_{ext}. This was defined as the time needed for the emission to decrease from 90% to 10%. The decane flame shows an extinction time of 16 ms, that a normalized with d/U_b gives a value of about 16. This value has the same order of magnitude as the previous heptane case, showing that a difference in the boiling point and density does not affect the extinction time and the blow-off transient behaviour of the spray case.

5.5.4 Blow-off correlation

The correlation of Radhakrishnan et al. [89], already tested for the non-premixed gaseous case and the n-heptane case, is here extended to a spray case with decane as fuel.

The resulting values of the group $\left[\left(\frac{U_b}{d}\right)\left(\frac{\nu}{S_L^2}\right)\right]^{1/2}$ for the spray flame blow-off are shown in Fig. 5.28. S_L at stoichiometry was taken from the data of Neophytou and Mastorakos [80] and ν evaluated at a temperature halfway between the reactants and the adiabatic flame temperature, as suggested by Mellor [75]. The values lie in the range 0.85 to 1.1. The scatter is considerably smaller than the scatter generally observed in the literature [75; 89; 96]. It confirms the possibility to extend the use of this correlation to spray flames.

5.6 Conclusions

The blow-off behaviour of swirling spray flames has been examined for two different fuels: n-heptane and n-decane. The measurements include blow-off limits and their attempted correlation, visualisation of the blow-off transient with 5 kHz OH* chemiluminescence, and the quantification of the average duration of the blow-off transient. It was found that a previously proposed correlation based on a Damköhler number does a reasonable job at collapsing both datasets. It was also found that the average duration of the blow-off event, τ_{ext}, is in order of the tens of ms for both spray flames (10-16 ms), which when normalized by d/U_{BO} becomes 10 for heptane and 16 for decane.

The blow-off event is therefore a relatively slow process for the spray flames using n-heptane and decane fuels. This suggests that control measures, such as fast fuel injection, coupled with appropriate detection, such as with chemiluminescence monitoring, may have a reasonable chance of success in keeping the flame alight very close to the blow-off limit.

OH-PLIF images at 5 kHz for flames far from and close to extinction showed that the spray flames intermittently lifts-off the bluff body, but less that the previous non-premixed gaseous case. The mean values of the lift-off height were around 2 mm depending less on the operating conditions comparing to the gaseous

case. Morover, the flame sheet showed evidence of localised extinctions.

The PLIF images showed a thin OH-zone typical of non-premixed flame structure. The reaction zone of the heptane and the decane flames had a conical shape. The inner cone corresponded to the stabilization of the flame along the spray cone, while the outer "legs" of the flame were attached to the bluff body edges and followed the shear layer between the annular air injection adn the central recirculation zone.

The emissions profiles measured for the heptane flames were relatively flat at the combustor outlet. Approaching the blow-off, the O_2 mole fraction increased, while the CO_2 decreased since the flame was overall leaner. In the flow conditions examined, the unburned hydrocarbon emissions were high indicating that the combustion was incomplete.

Even though it is reasonable to expect that different liquid fuels yield different atomization and evaporation times (and thus a different blow-off behaviour), this is not the case in the two cases presented in this thesis. In fact the atomization, for these low viscosity fuels (heptane and decane) is only driven by the surface tension which does not change significantly for many paraffin based fuels. Also the evaporation time, which is proportional to the evaporation rate, is not very sensitive to the fuel change. In fact as it is shown by Lefebvre [60], the boiling temperature of the fuel does not affect significantly the evaporation rate.

These results, together with those obtained for the non-premixed gaseous case in the previous chapter, further the body of experimental data available for the validation of turbulent non-premixed flame models. The quantification of some properties during the blow-off transient can assist studies of extinction based on large-eddy simulation that have a promise of capturing combustion transients.

5.7 Figures for chapter 5

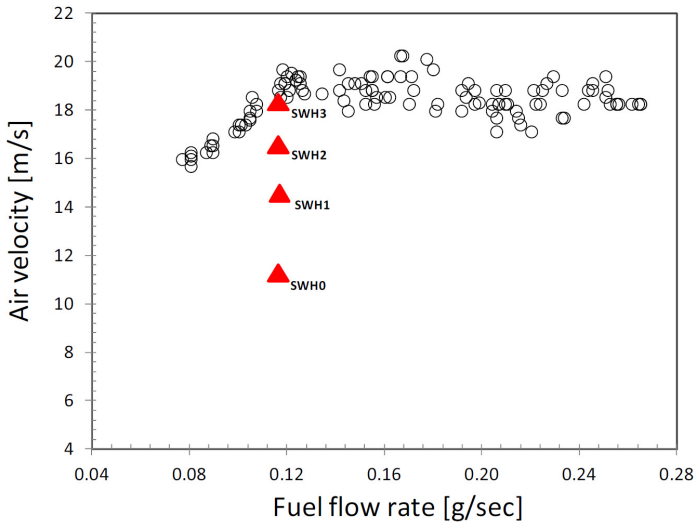

Figure 5.1: Air velocity at blow-off as a function of the fuel flow rate for the spray heptane flame. The triangles denote the stable flow conditions SWH0, SWH1, SWH2 and the blow-off condition SWH3.

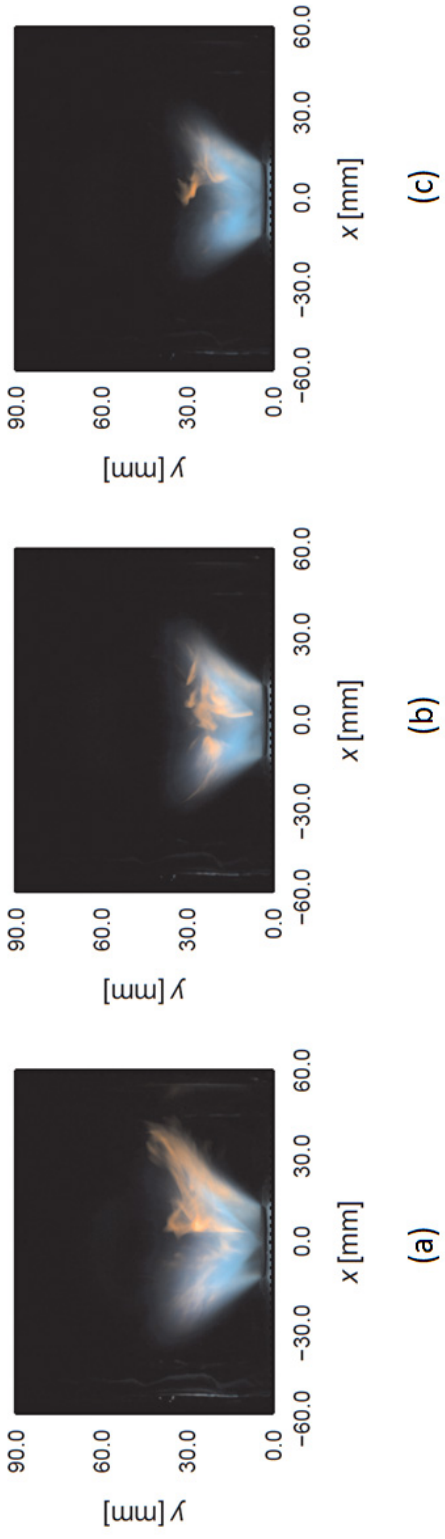

Figure 5.2: Photographs of heptane spray flames: (a) SWH0 (b) SWH1, (c) SWH2. Exposure time: 30 ms.

Figure 5.3: Abel-transformed time-averaged OH* chemiluminescence images for heptane spray flames at different stable flow conditions: (a) SWH0, (b) SWH1, (c) SWH2.

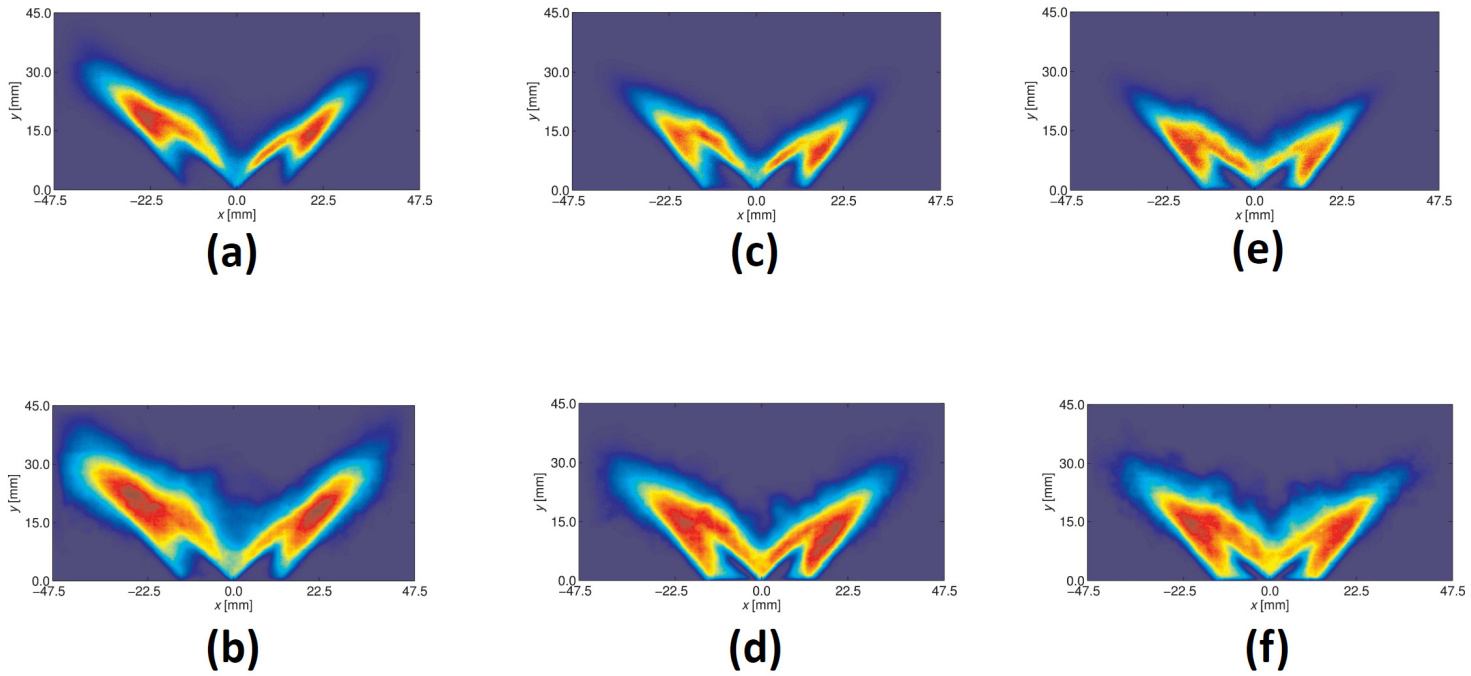

Figure 5.4: Time-averaged images over 5000 frames (equivalent to a data acquisition time of 1 s). First row: average images. Second row: RMS. Flow conditions SWH0 (a-b), SWH1 (c-d) and SWH2 (e-f). Side view, flow comes from below, axis of the burner at the centre of the x range.

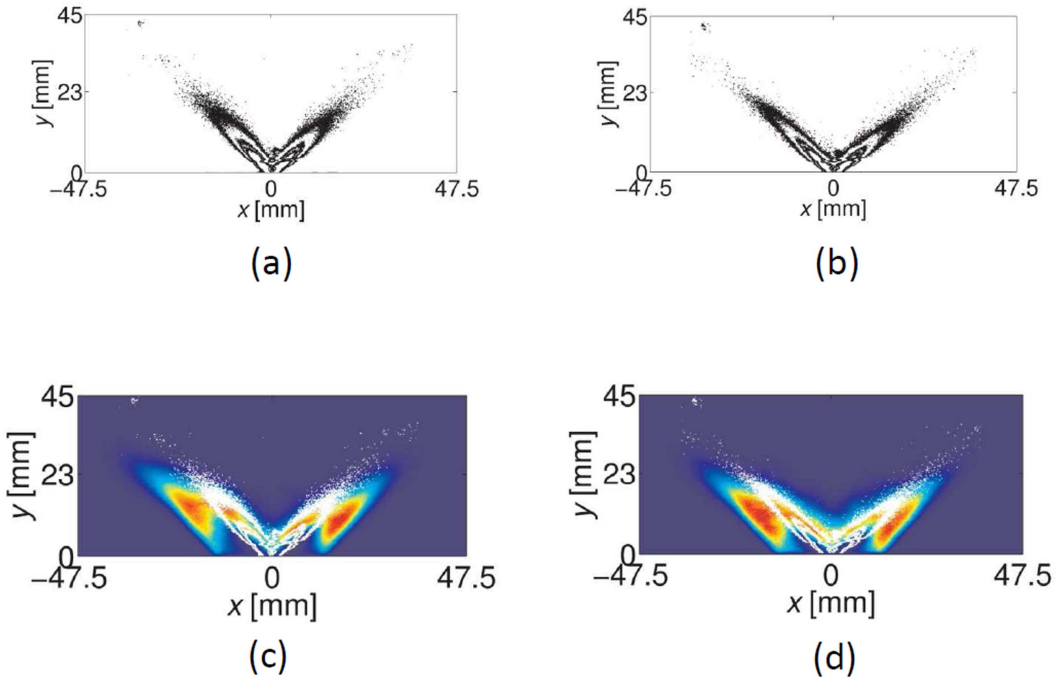

Figure 5.5: Time-averaged images over 5000 frames of heptane spray Mie scattering (top row) and OH-PLIF images superimposed on the same Mie scattering images (bottom row) of spray flames: (a, c) SWH1 and (b, d) SWH2.

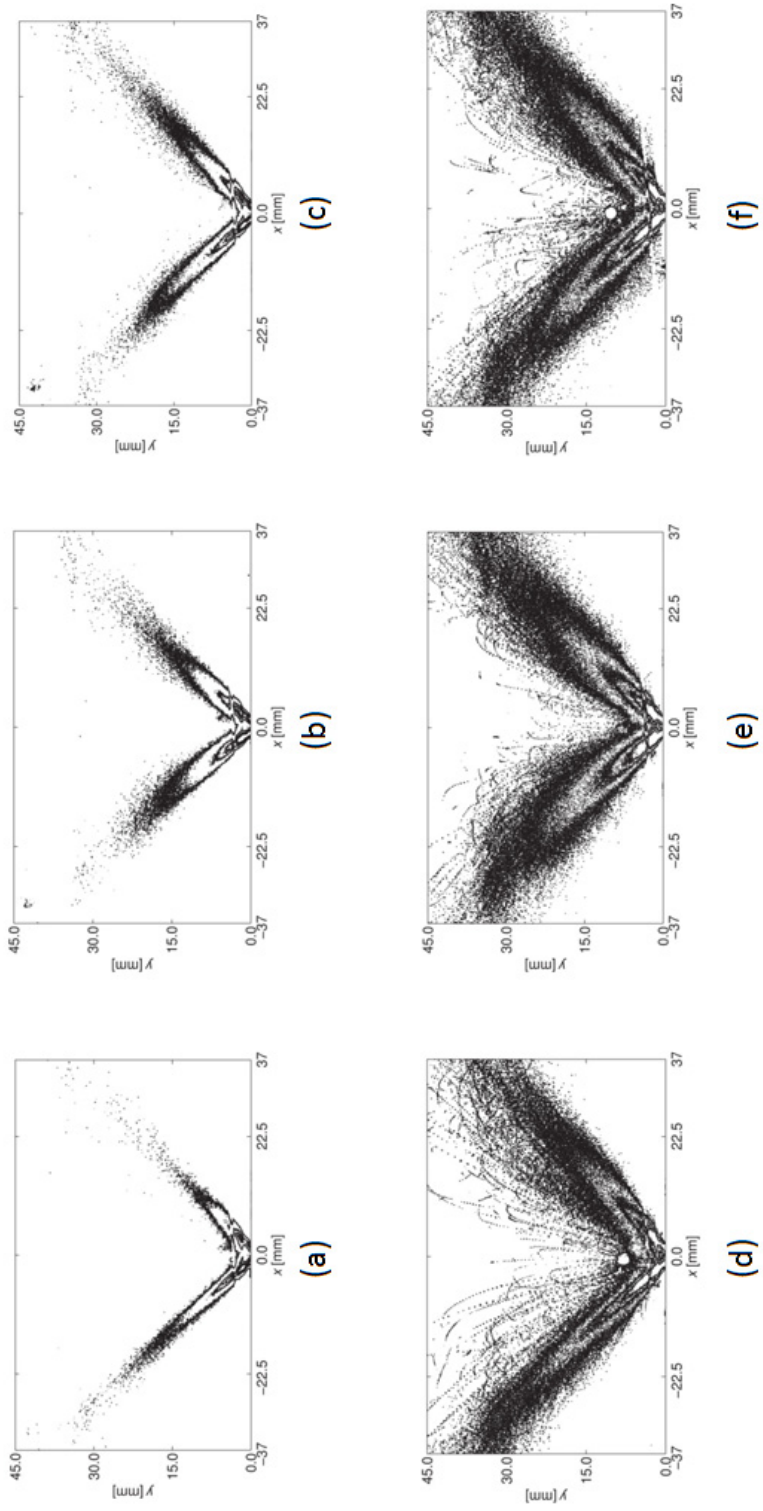

Figure 5.6: Time-averaged images over 5000 frames of spray Mie scattering at stable flow conditions: (a) SWH0, (b) SWH1, (c) SWH2. First row: average images. Second row: RMS.

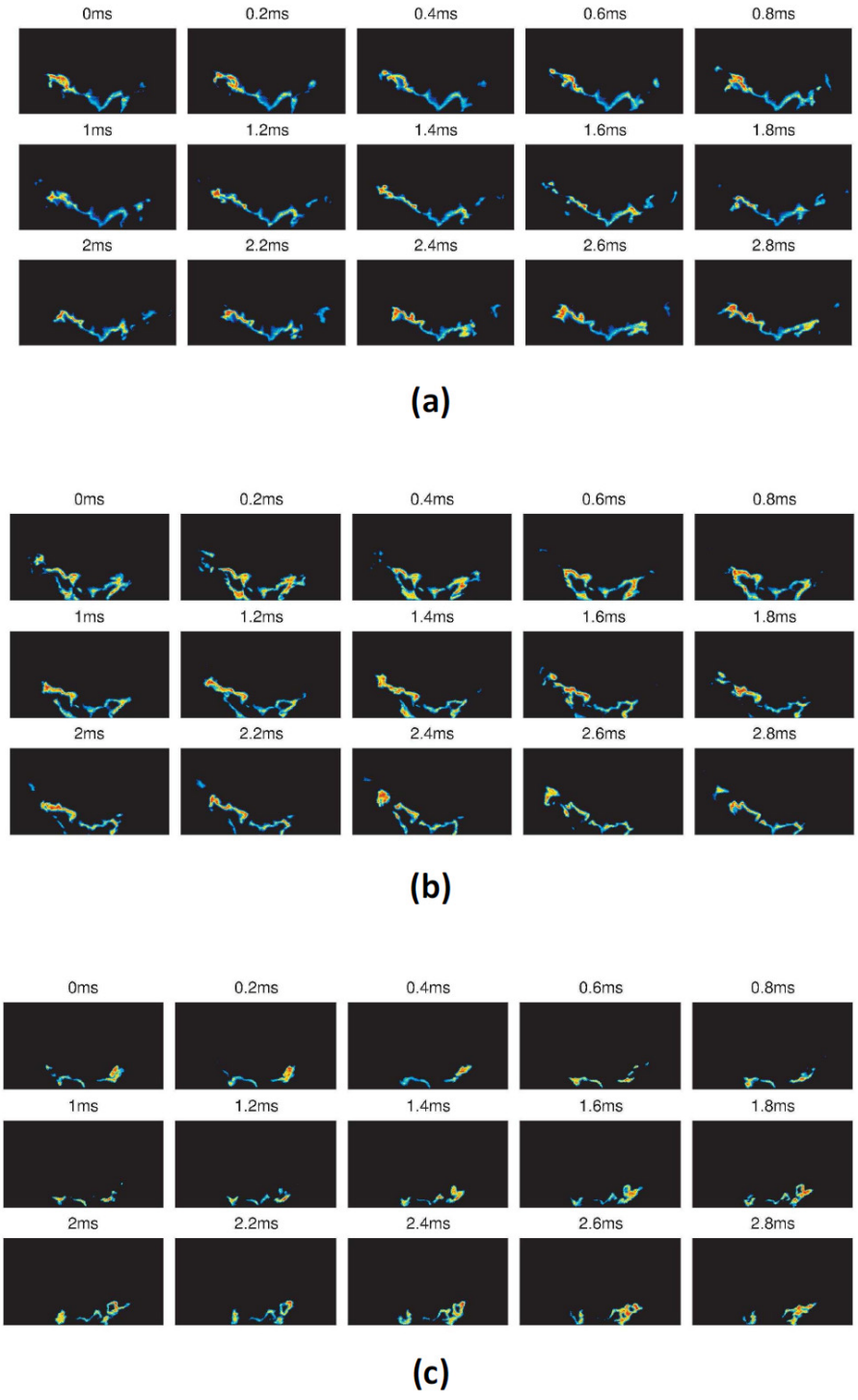

Figure 5.7: Sequence of instantaneous OH-PLIF images showing the temporal evolution of the structure of the flame at stable conditions: (a) SWH0, (b) SWH1, (c) SWH2.

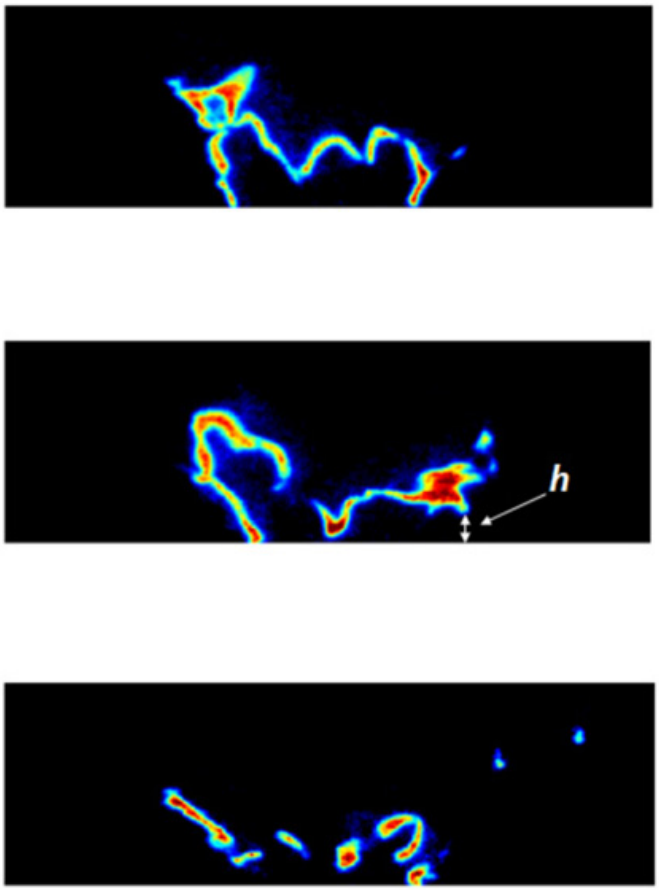

Figure 5.8: Independent OH-PLIF snapshots for spray heptane flames (image size 30×95 mm); from top to bottom: SWH1, SWH1, SWH2. The three instantaneous images are separated by a time delay.

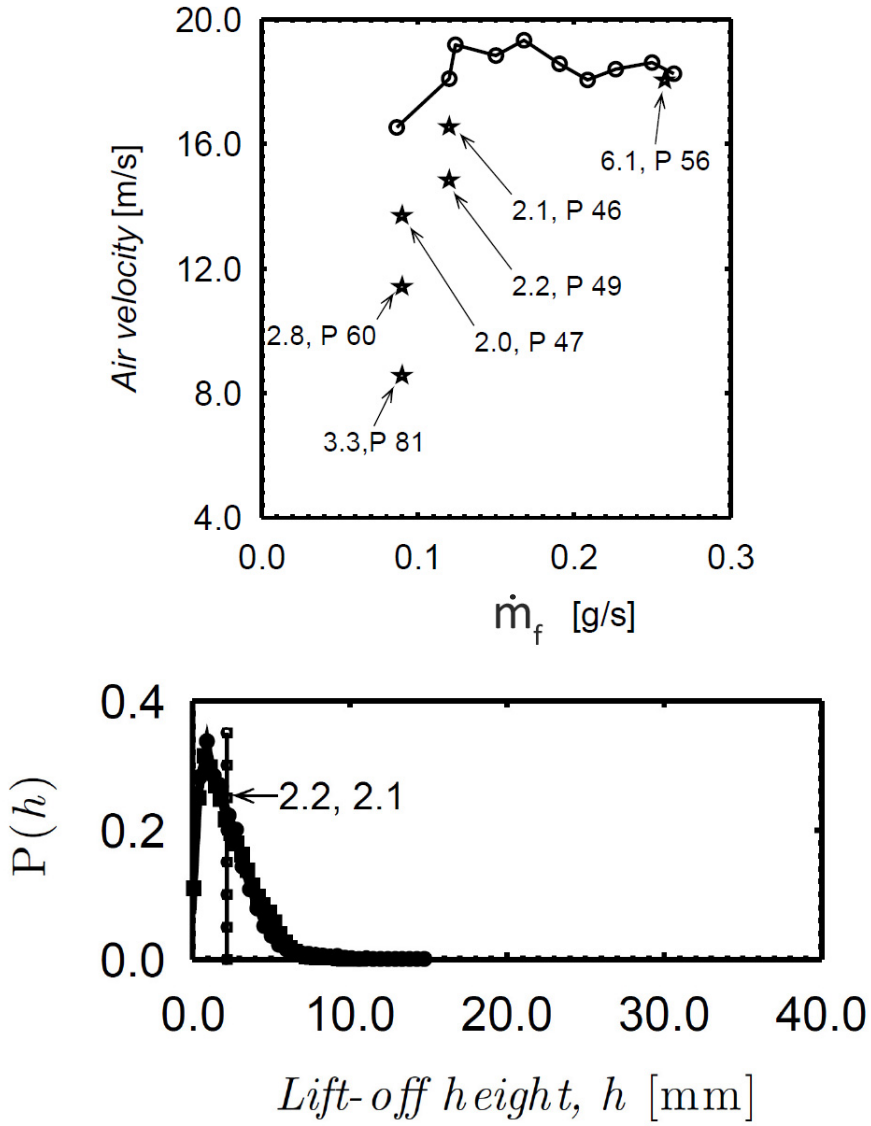

Figure 5.9: Upper: Air velocity at blow-off as a function of the fuel flow rate. Same data as Fig. 5.1, replotted here for clarity. The stars denote flames far from blow-off. The number denotes the mean lift-off height in mm. The first number denotes the mean lift-off height in mm and the second the percentage of time the flame is lifted. Lower: Probability density function of the lift-off height, SWH1 (square) and SWH2 (circle). The numbers indicated show the average lift-off height in mm.

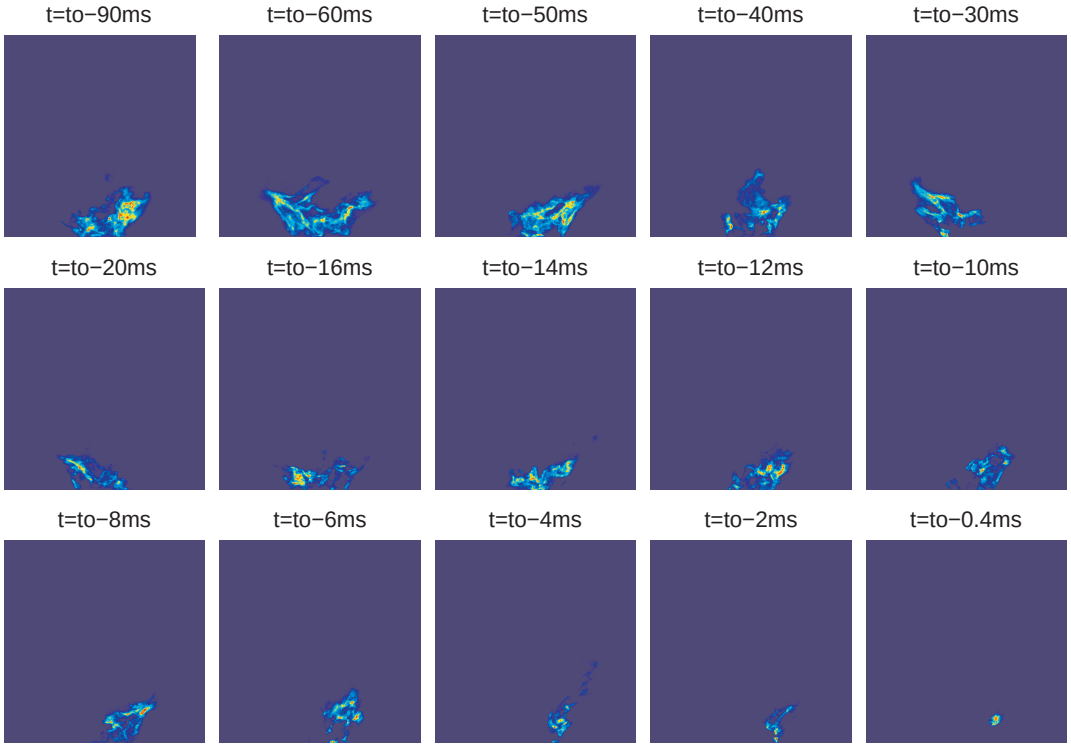

Figure 5.10: OH* chemiluminescence sequence of a blow-off event for a spray flame at condition SWH3. Side view, flow comes from below, axis of the burner at the centre of the x range. Image size 90 mm $\times$ 90 mm.

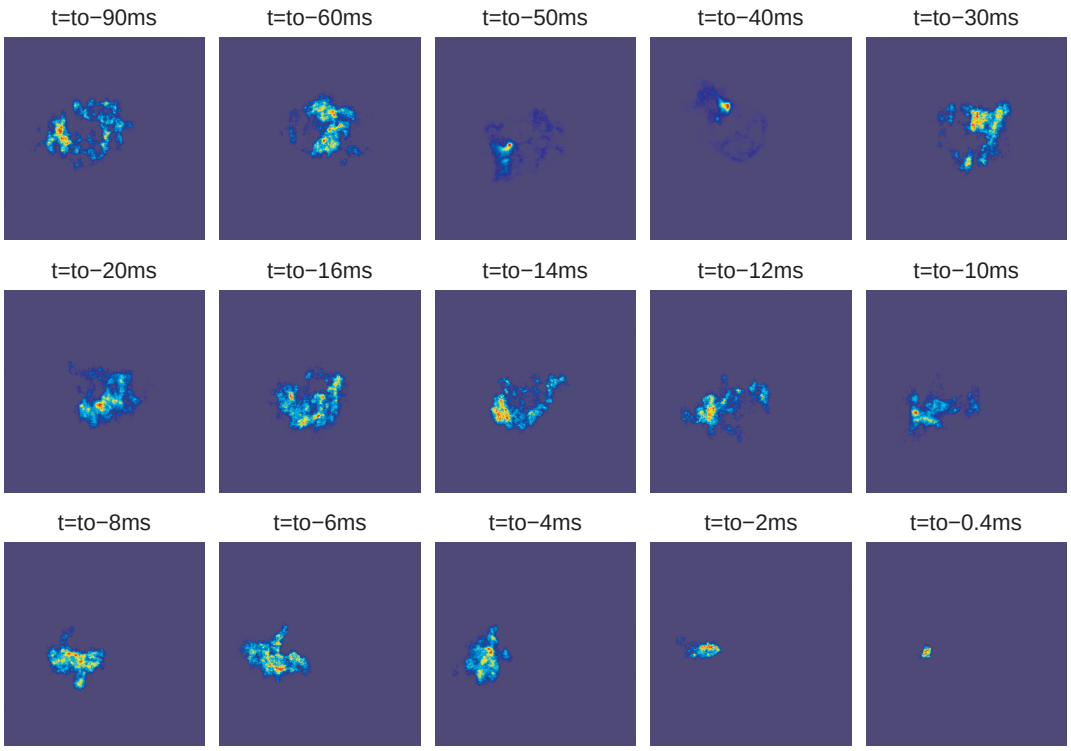

Figure 5.11: OH* chemiluminescence sequence of a blow-off event for a spray flame at SWH3 condition. Top view, burner axis at the centre of the image. Image size 90 mm × 90 mm.

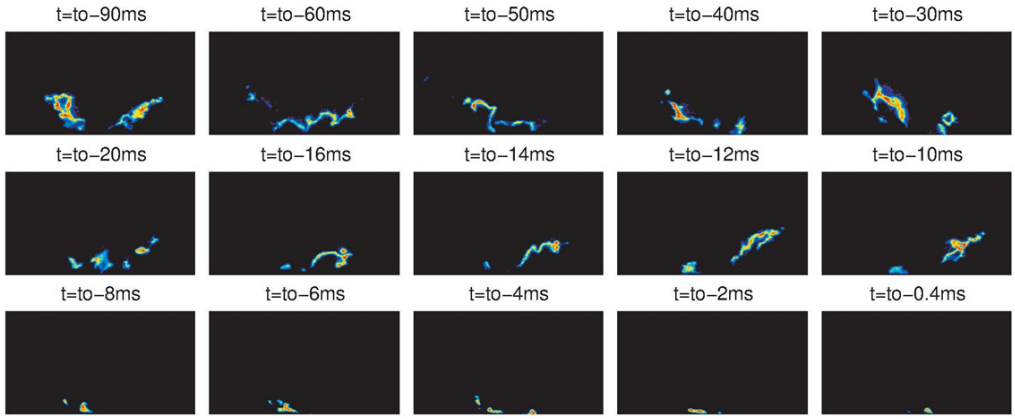

Figure 5.12: OH-PLIF sequence of a blow-off event for a spray flame at SWH3 condition.Burner axis at the centre of the image. Image size 50 mm × 95 mm.

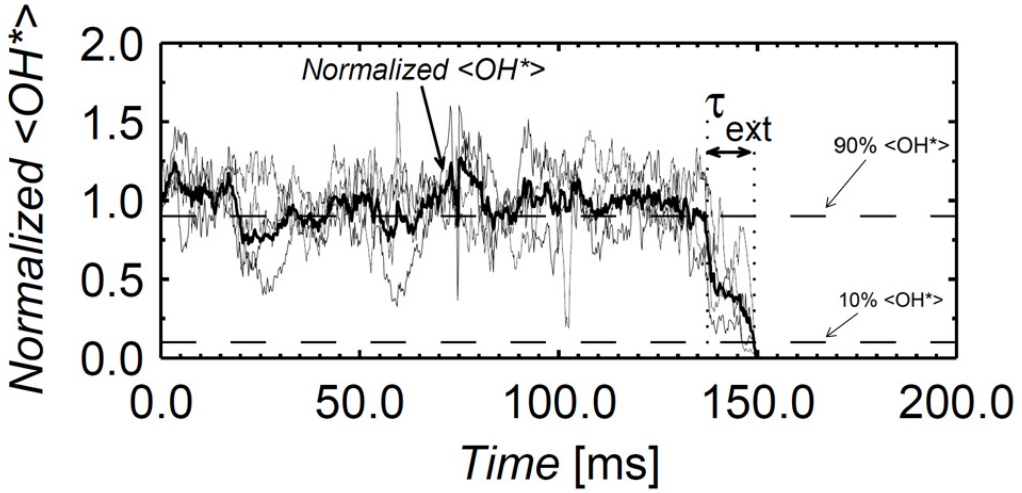

Figure 5.13: Average of area-integrated OH* time series (thick line), and area-integrated OH* from individual blow-off events (thin lines), each shifted to match the instant of extinction and normalized by its pre-extinction value. The definition of the duration of the blow-off event, τ_{ext}, is indicated.

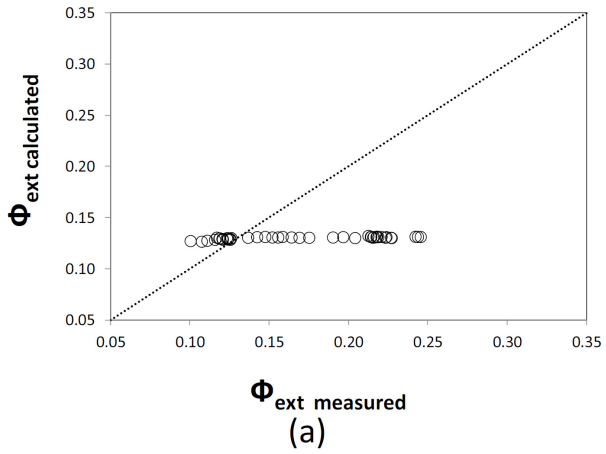

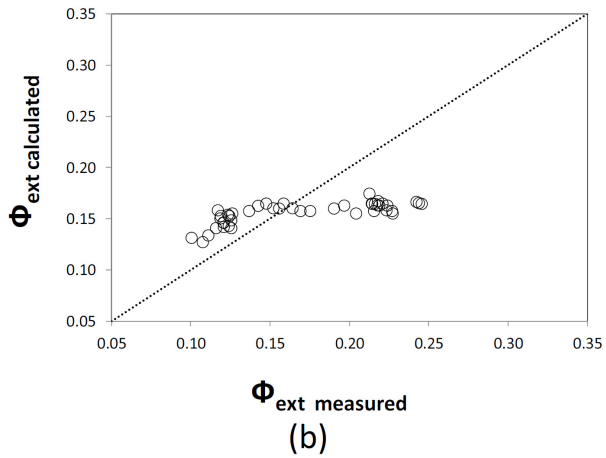

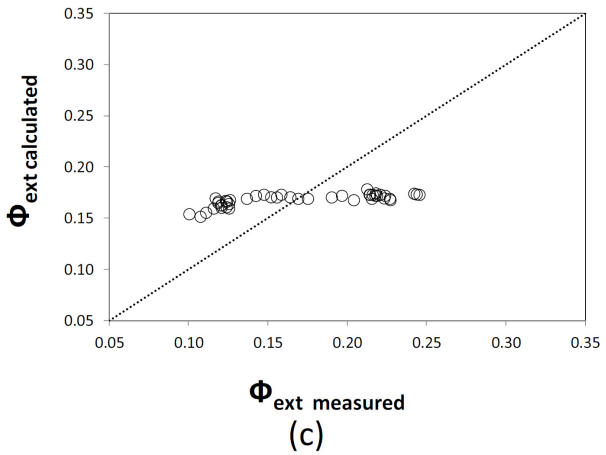

Figure 5.14: Comparison of measured and predicted values of extinction limits with different correlations. (a) Equation 5.1. (b) Equation 5.2. (c) Equation 5.3.

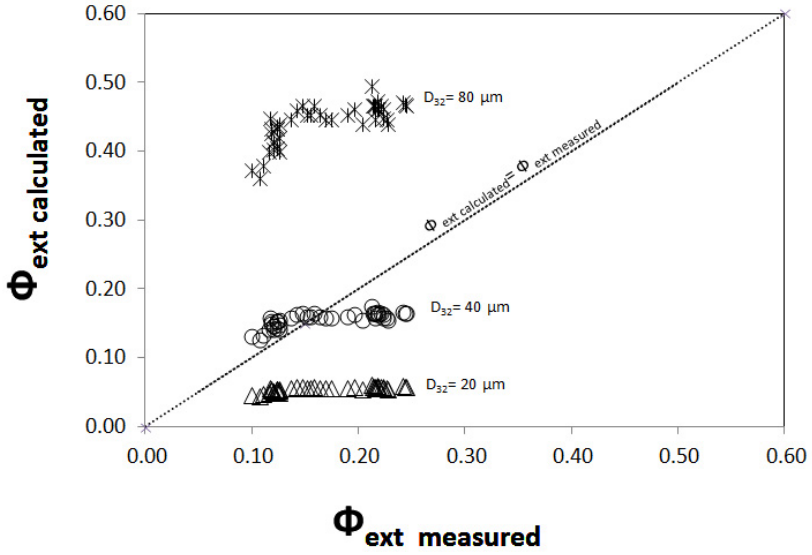

Figure 5.15: Comparison of measured and predicted values of extinction limits with equation 5.2 and three different D_{32}. Triangles represent the values calculated with D_{32}= 20 μm, circles with D_{32}= 40 μm, stars with D_{32}= 80 μm.

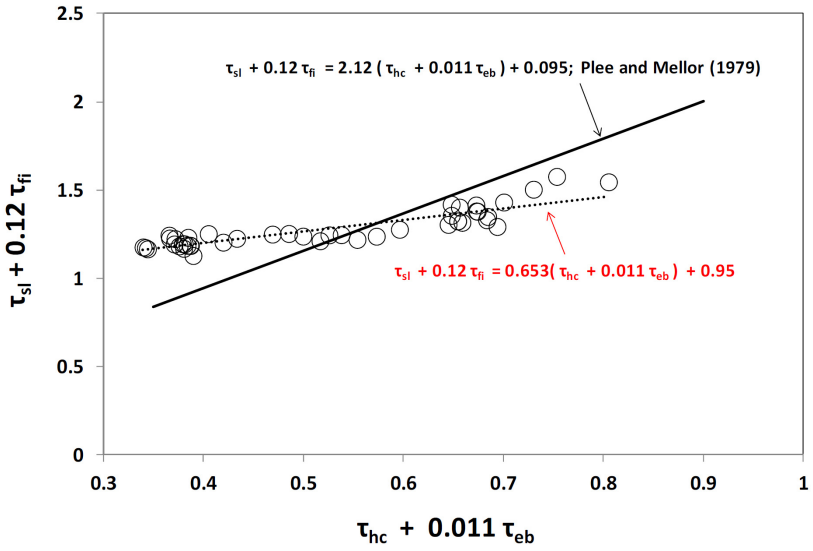

Figure 5.16: Complete characteristic time correlation for blow-off limit based on the correlation of Plee and Mellor [86], Eq. (5.6).

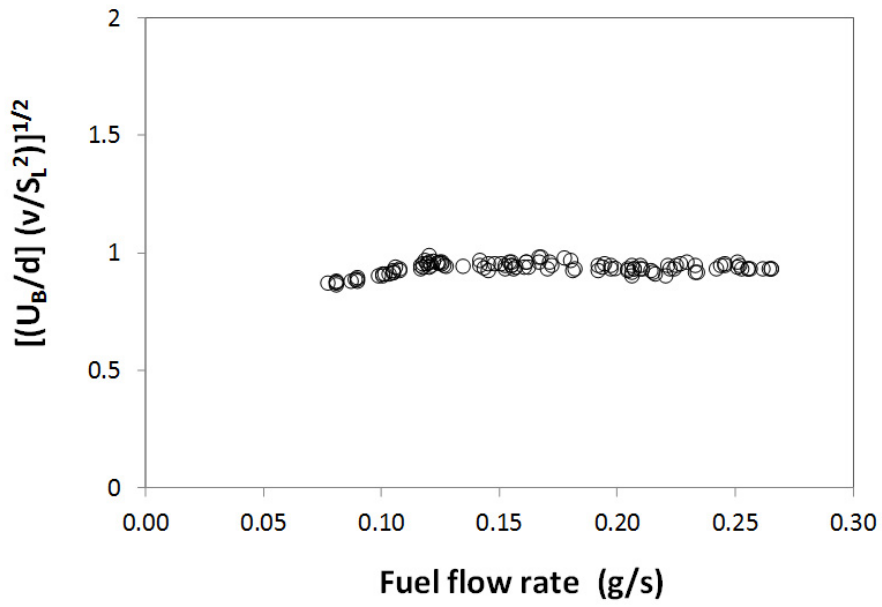

Figure 5.17: Evaluation of 1/Da $\left(\left[\left(\frac{U_b}{d}\right)\left(\frac{\nu}{S_L^2}\right)\right]^{1/2}\right)$ based on the extinction correlation proposed by Radhakrishnan et al. [89], as a function of the fuel flow rate, for the heptane spray flames.

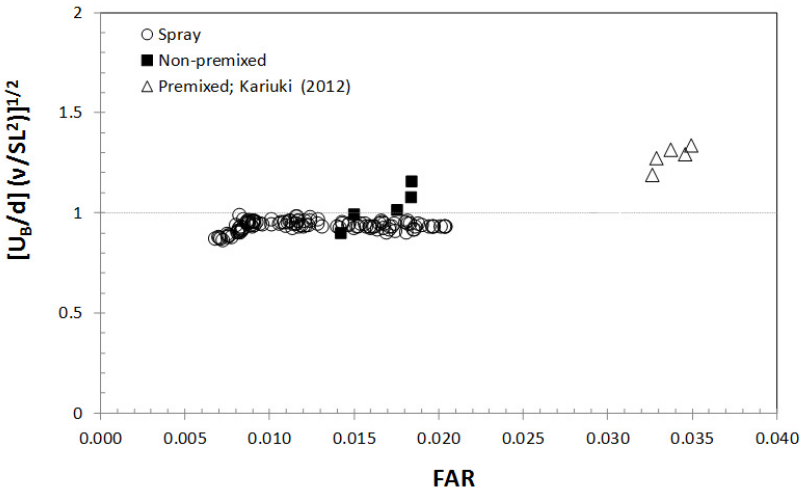

Figure 5.18: Evaluation of Da $\left(\left[\left(\frac{U_b}{d}\right)\left(\frac{\nu}{S_L^2}\right)\right]^{1/2}\right)$ based on the extinction correlation proposed by Radhakrishnan et al. [89], as a function of the fuel air ratio for different combustion regimes. The premixed data are from Kariuki et al. [52].

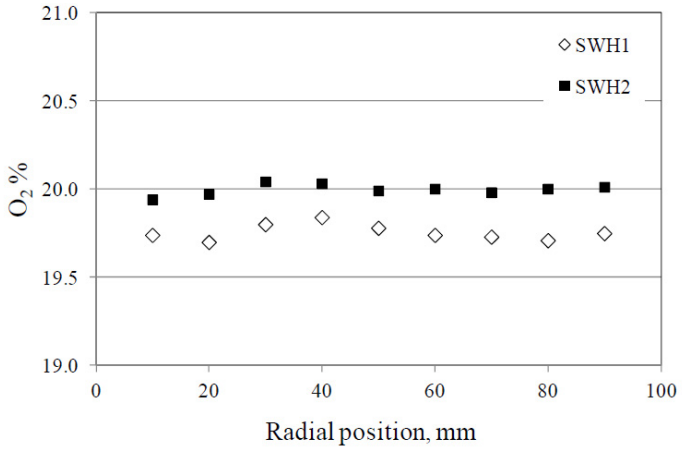

(a)

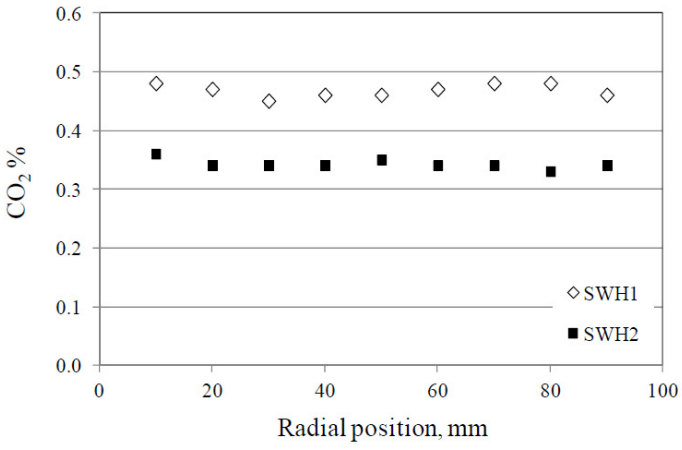

(b)

Figure 5.19: Dry O_2 mole fraction (a) and dry CO_2 mole fraction (b) for SWH1 and SWH2 flow condition. The values are corrected to a 15 % level of O_2 in the dry product stream.

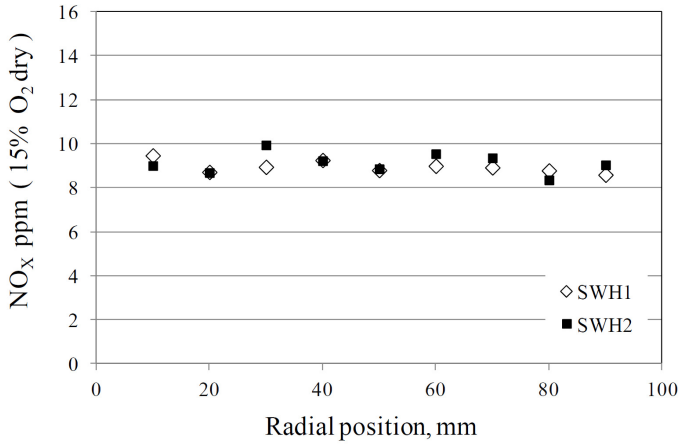

(a)

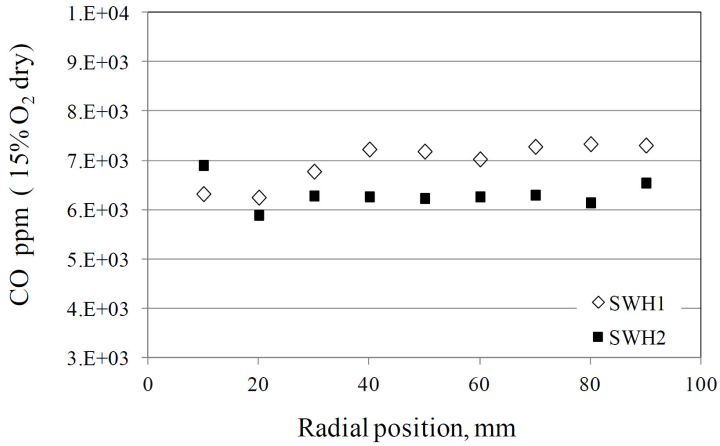

(b)

Figure 5.20: Dry NO_x mole fraction (a) and dry CO mole fraction (b) for SWH1 and SWH2 flow condition.

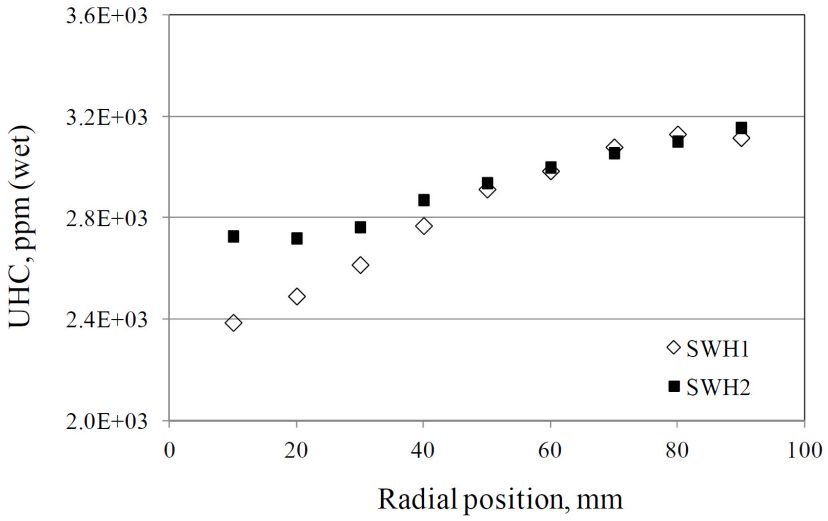

Figure 5.21: Wet UHC emissions for SWH1 and SWH2 flow condition.

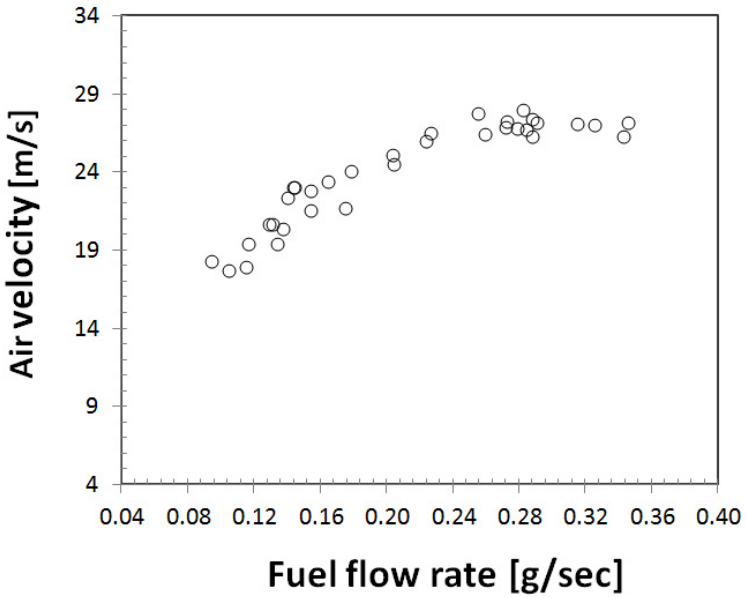

Figure 5.22: Air velocity at blow-off as a function of the fuel flow rate for the spray decane flame.

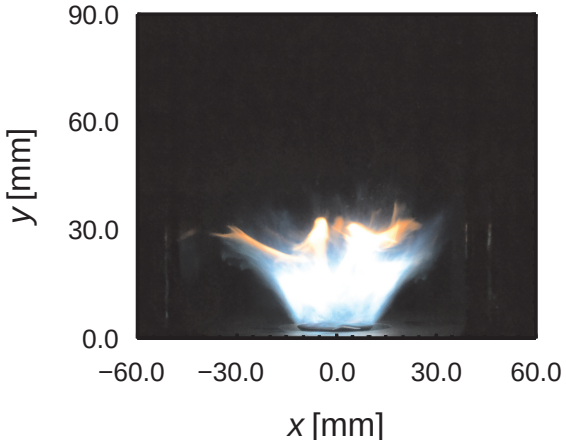

Figure 5.23: Photograph of the decane spray flames. Flow condition SWD1. Exposure time: 30 ms.

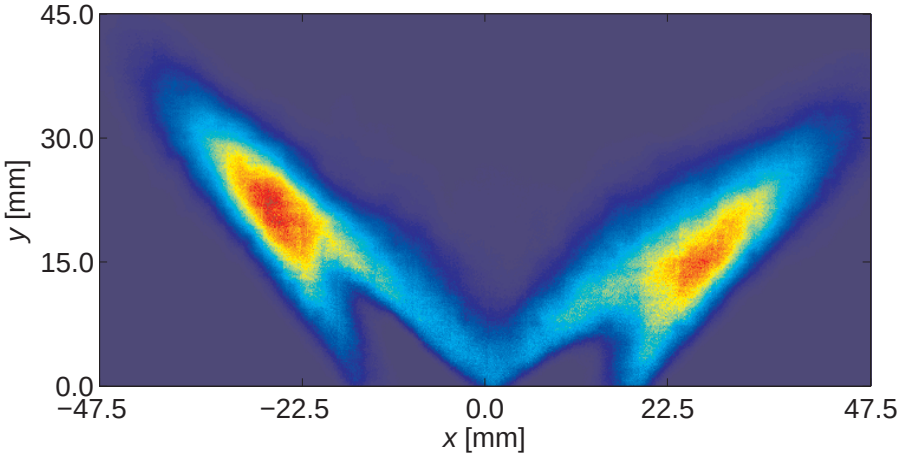

Figure 5.24: Time-averaged OH-PLIF images over 3000 frames for the spray decane flame. Flow condition SWD1. Side view, flow comes from below, axis of the burner at the centre of the x range.

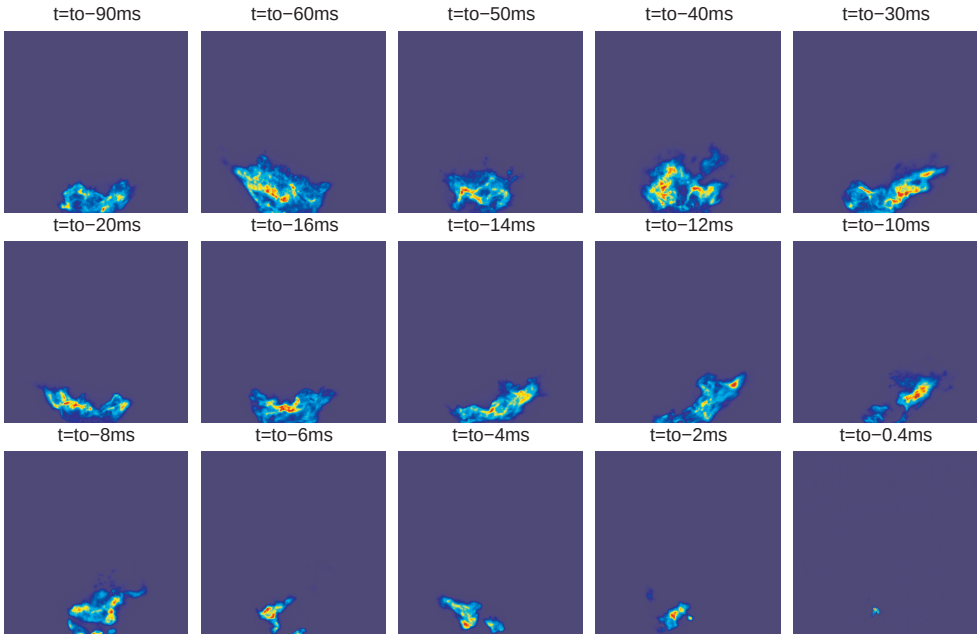

Figure 5.25: OH* chemiluminescence sequence of a blow-off event for a spray decane flame at SWD3 condition. Front view, burner axis at the centre of the image. Image size 90 mm × 90 mm.

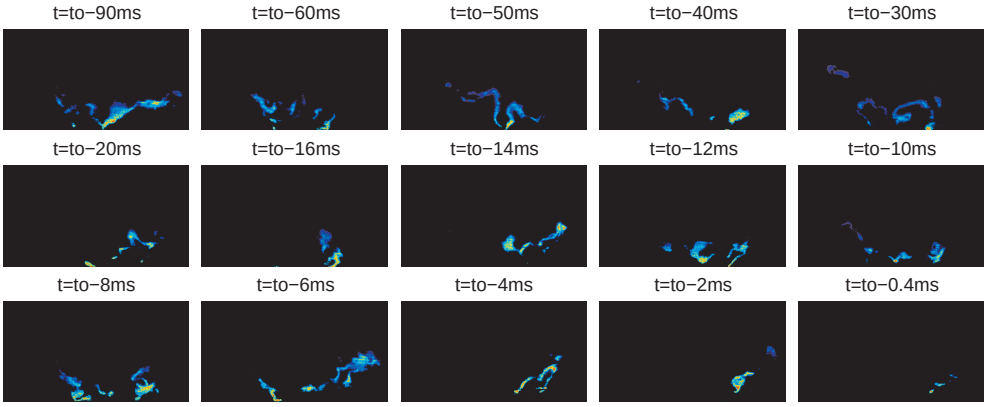

Figure 5.26: OH-PLIF sequence of a blow-off event for a spray decane flame at SWD3 condition. Burner axis at the centre of the image. Image size 50 mm × 95 mm.

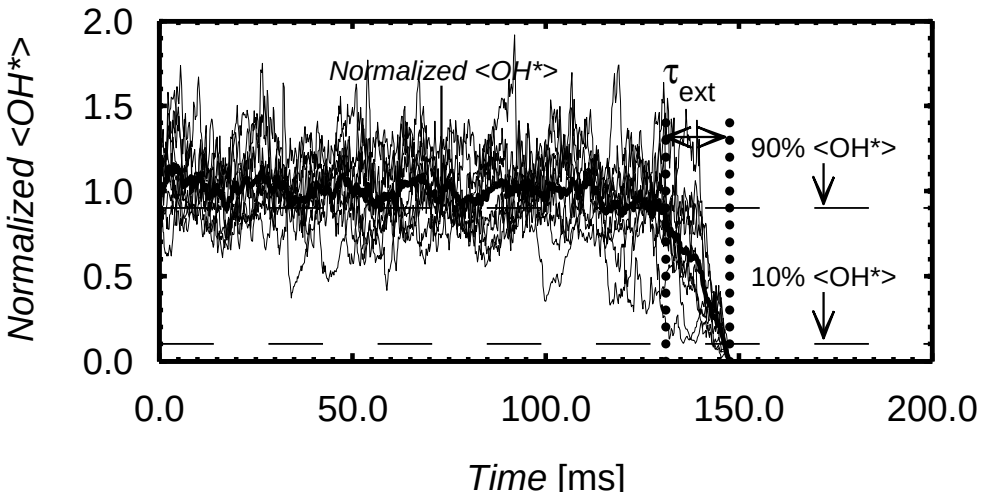

Figure 5.27: Average of area-integrated OH* time series (thick line), and area-integrated OH* from individual blow-off events (thin lines) for decane spray flames, each shifted to match the instant of extinction and normalized by its pre-extinction value. The definition of the duration of the blow-off event, τ_{ext}, is indicated.

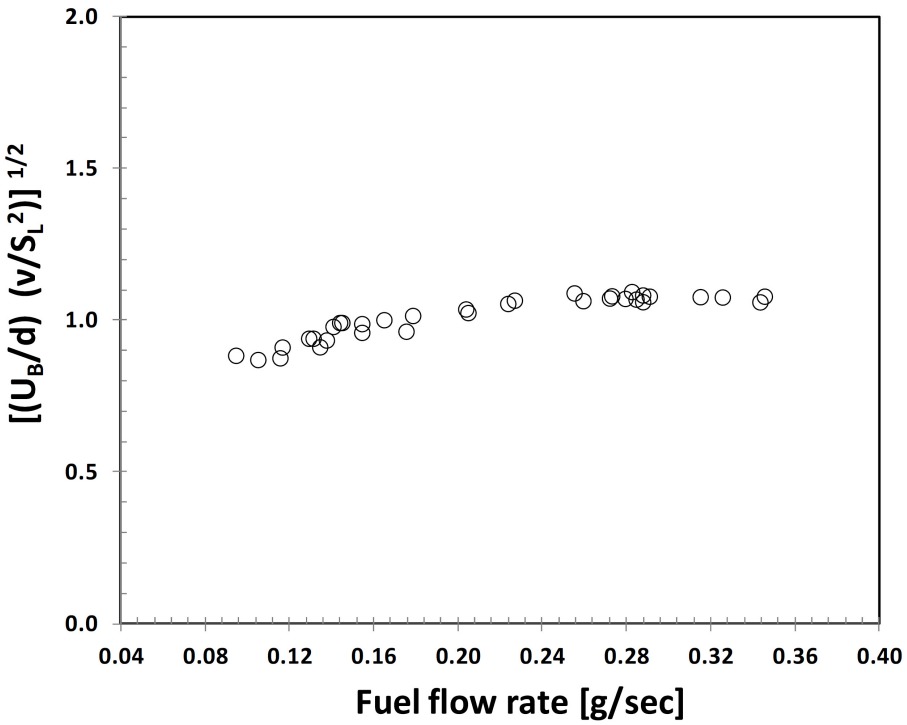

Figure 5.28: Evaluation of 1/Da $\left(\left[\left(\frac{U_b}{d}\right)\left(\frac{\nu}{S_L^2}\right)\right]^{1/2}\right)$ based on the extinction correlation proposed by Radhakrishnan et al. [89], as a function of the fuel flow rate for the decane spray flame.

Chapter 6

Conclusions and suggestions for further research

In the present work, experimental measurements were performed in order to increase our understanding of blow-off and flame stabilization in gaseous non-premixed and spray flames. In the literature review of Chapter 1, we identified several areas worth investigating. In this thesis, we focused on: flame shape changes approaching blow-off, duration of the blow-off event, and the dynamics of the blow-off event. Qualitative and quantitative meaurements have been obtained using high speed (5kHz) imaging apparatus and laser diagnostics to characterize the flame shape, reaction zone and velocity field for different flow conditions approaching the blow-off. An experimental data base has hence been developed from the findings, which is particularly useful for validation of CFD and advanced combustion models for non-premixed and spray flames close to the lean extinction limit. Furthermore, the thesis provides a validation of an extinction limit correlation, reported by Radhakrishnan [89], in different combustion regimes. The key conclusions from the work presented in the previous chapters are consolidated and summarised in the following sections. The chapter closes with some recommendations for further research.

6.1 Conclusions from this work

6.1.1 Velocity fields

Measurements of the axial, radial and tangential componets were obtained for the non-reacting case to understand the aerodynamic pattern within the combustion chamber and provide validation data for CFD models. These were obtained using Laser Doppler Anemometry for flow conditions similar to those to study flame stabilization and blow-off of the reacting cases. A central and a side reciculation zone have been observed.

Moreover, velocity field measurements in the reacting case with the same laser technique were performed for the two combustion regimes: non-premixed gaseous and the spray case. In the non-premixed gaseous case the velocity profiles showed a very good symmetry of the flow. The central area of the combustor is characterized by a high axial velocity due to the fuel penetrating into the central recirculation zone, while low and negative axial velocities are observed at an distance of 110 mm from the bluff body. The velocity profiles for this reacting case confirms the presence of a side recirculation zone and that the fuel jet stagnates, resulting in a short flame.

For the spray reacting case two different velocity measurements have been presented: (a) the droplet velocity measurements from regions where droplets exist (i.e. close to the bluff body), taken without TiO_2 seeding in the air; (b) the air velocity field from regions where droplets have evaporated and therefore the TiO_2 seeding particles are virtually the only scatterers giving signal to the LDA. The velocity droplet profiles indicate an excellent degree of symmetry of the flow. Two peaks of the axial droplet velocity are observed close to the centre of the fuel injection due to the hollow cone spray shape. The swirl droplet velocity profiles have a maximum value where the droplets meet the annular air injection. The clear identification of the droplet velocity field close to the bluff body is important since it affects the flame shape. For the second set of measurements (case b), the axial velocity peaks shift along the radius according to the expected swirl jet aperture. The air and the droplet measurements are different in the central part of the reacting flow close to the fuel spray injection. It is important to observe

that the central recirculation zone observed for the spray reacting case is quite wider than the corresponding non-reacting case.

The velocity and turbulence information obtained is particularly useful for providing data on the velocity flow field, which is crucial for validation of computational models.

6.1.2 Non-premixed flames

The behaviour of the flame approaching and during the blow-off event was studied using fast imaging (5 kHz) of OH chemiluminescence and OH-PLIF for non-premixed gaseous flame using methane as fuel. The key stages of the flame shape were shortening of the reaction zone and fragmentation of the flame just above the bluff body.

OH-PLIF images for flames far from and close to extinction showed that the non-premixed flame intermittently lifts-off the bluff body, with increasing probability as the fuel velocity increases. The flame sheet shows clear evidences of localised extinctions for the two flow conditions close to the blow-off. The average duration of the blow-off event was quantified, and found to be about 46 ms, which corresponds to about 40 d/U.

The extinction correlation proposed by Radhakrishnan et al. [89] was shown to give good collapse of the extinction data for the range of flow conditions studied, giving good credence to its use in the non-premixed case. The emissions of NO_x, CO, CO_2, O_2 and UHC have also been measured for the stable flames. Thus, a detailed database for this configuration has been generated, and is useful for validation of turbulent non-premixed flame models. The quantification of the extinction time can assist studies of extinction based on large-eddy simulation.

6.1.3 Spray flames

Spray flames with two liquid fuels (n-heptane and decane) at conditions approaching and during the blow-off condition were studied using fast imaging (5 kHz) of OH chemiluminescence and OH-PLIF. The flame shape was different from the

non-premixed gaseous case. It was shorter and more compact. The reaction zone was located along the spray cone and along the shear layer.

Good collapse of the extinction data of the spray flames was obtained using the extinction correlation proposed by Radhakrishnan et al. [89], previously applied to the non-premixed gaseous case. The average duration of the blow-off transient was the same order of magnitude of the non-premixed gaseous case, about 10-20 ms. The blow-off event is therefore a relatively slow process for the spray flames using n-heptane and decane fuels. This suggests that control measures, such as fast fuel injection, coupled with appropriate detection, such as with chemiluminescence monitoring, may have a reasonable chance of success in keeping the flame alight very close to the blow-off limit. The emissions of NO_x, CO, CO_2, O_2 and UHC have also been measured for the stable flames of the spray heptane case. The data obtained is useful to better understand blow-off in practical applications as gas turbines and can be used for validation of advanced combustion models.

6.2 Suggestions for further research

The results obtained from this work provide useful insights characterizing the changes in the structure of non-premixed gaseous flames and spray flames approaching the lean blow-off limit. The data can be used as validation data for non-premixed models as the conditional moment closure method.

Velocity measurement for the different combustion regimes were important to understand the presence of the different recirculation zones, the fuel penetration for the non-premixed gaseous case and the droplet velocites for the spray case within the combustion chamber. These data are crucial for CFD model validation. Detailed droplet size distribution (and related dimensions) for the spray case is required to have a more complete experimental database. Detailed fuel distribution of the non-premixed case is also required to better understanding the fuel injection and the mixing occurring in the combustion chamber.

The OH-PLIF results showed several local extinctions, that can be due to an out-of-plane motion, and for this reason these results have to be carefully

treated. To reduce the influence of out-of-plane motion on the analyzed extinction events is necessary to measure simultaneously the velocity field (PIV) and the OH distribution (PLIF).

The quantification of the extinction time can assist studies of the blow-off phenomenon based on large-eddy simulation. It also raises some questions on which mechanisms control the total extinction in particular during the last stages of flame fragmentation of the blow-off event. The understanding of the blow-off event in this relatively simple burner configuration could aid in the design of more complex combustion chambers, where control strategies to prevent extinction can be applied knowing the extinction time and the related technique, presented in this work, to measure it.

Large-eddy simulations with models that can include localized extinctions (for example, the Conditional Moment Closure [7; 37] or the transported PDF method [48]) have been shown to be able to reproduce statistics of localized extinctions. The present data could be used for further post-processing and validations of such modelling efforts for flames of greater technological relevance. However, further data are needed to make the present flames a more comprehensive database for model validation and for deeper understanding of the blow-off process.

References

[1] Product description. *Lechler Company, http://www.lechlerusa.com*, 2012. xiii, 35, 51

[2] S. F. Ahmed, R. Balachandran, T. Marchione, and E. Mastorakos. *Combust. Flame*, **151**:366–385, 2007. 33, 102

[3] S.A. Ahmed. *Proc. Inst. Mech. Eng., Part G: J. Aerosp. Eng.*, **211**[2]:113 – 122, 1997. 4

[4] Dantec Dynamics A/S. Bsa flow software guide, version 3. 2004. 38

[5] A. Ateshkadi, V.G. McDonell, and G.S. Samuelsen. *Proc. Combust. Inst*, **28**:1281–1288, 2000. 18, 19, 20

[6] S. Ayache, J.R. Dawson, A. Triantafyllidis, R. Balachandran, and E. Mastorakos. *Int. J. Heat Fluid Fl.*, **31**[5]:754–766, 2010. 39

[7] S. Ayache and E. Mastorakos. *Flow, Turbul. and Combust.*, **88**[1]:207–231, 2012. 104, 168

[8] R. Balachandran. PhD thesis, University of Cambridge, 2005. 43

[9] R. Balachandran, B. O. Ayoola, C. F. Kaminski, A. P. Dowling, and E. Mastorakos. *Combust. Flame*, **143**:37–55, 2005. 33, 40

[10] R. Balachandran, A. P. Dowling, and E. Mastorakos. *Flow, Turbulence and Combustion*, **80**:455–487, 2008. 42

[11] J. Baldwin. Independent Publishing Platform, 2012. 1

[12] D.R. Ballal and A.H. Lefebvre. *J. Eng. Power*, **102**:416–421, 1980. 8, 9, 18, 19, 21, 130, 131, 132

[13] R. S. Barlow and J. Frank. *Proc. Combust. Inst.*, **27**:1087–1095, 1998. 13

[14] J. M. Beer and N. A. Chigier. *Appl. Sci.*, pages 100 – 146, 1972. 4, 34

[15] R.W. Bilger. *Prog. Energ. Combust.*, **1**[2]:87–109, 1976. 11

[16] C.T. Bowman. *Symposium (Intern.) Combust.*, **24**[1]:859 – 878, 1992. 108

[17] R.D. Brum and G.S. Samuelsen. *Exp. Fluids*, **5**:95–102, 1987. 63

[18] J. Burguburu, G. Cabot, B. Renou, A.M. Boukhalfa, and M. Cazalens. *Proc. Combust Inst.*, **33**[2]:2927–2935, 2011. 18

[19] Soares C. *Gas Turbines: A Handbook of Air, Land, and Sea Applications*. Butterworth-Heinemann, 1st edition, 2008. xii, 3, 29

[20] R.S. Cant and E. Mastorakos. *An introduction to turbulent reacting flows*. Imperial college press, 1st edition, 2008. 10, 45

[21] A. Cavaliere, R. Ragucci, and C. Noviello. *Exp. Therm. Fluid Sci.*, **27**[4]:449–454, 2003. 15

[22] M. Cazalens, M. Rullaud, and J.P. Frenillot. *J. Propul. Power*, **24**[4]:779–787, 2008. 2

[23] S. Chaudhuri and B. M. Cetegen. *Combust. Flame*, **153**:616–633, 2008. 8

[24] R. Chen and R.L. Axelbaum. *Combust. Flame*, **142**[1–2]:62–71, 2005. 12

[25] N.A. Chigier and C.G. McCreath. *Acta Astronaut.*, **1**[5]:687–710, 1974. 16

[26] L. M. Cohen, J.M. Jassowski, and J.I. Ito. *AIAA journal*, pages 1926–1935, 2001. 42

[27] M. Cohen. *Combined Cycle J.*, pages 775–782, 2011. 3

[28] B.B. Dally, A.R. Masri, R.S. Barlow, G.J. Fiechtner, and D.F. Fletcher. *Combust. Flame*, **114**:119–148, 1998. 13, 64

[29] J. R. Dawson, R. L. Gordon, J. Kariuki, E. Mastorakos, A. R. Masri, and M. Juddoo. *Proc. Combust. Inst.*, **33**:1559–1566, 2011. 8, 41, 105

[30] S. R. N. De Zilwa, I. Emiris, J. H. Uhm, and J. H. Whitelaw. *Proc.of the R. Soci. of Lond.*, **457**:1915–1949, 2001. 4, 5

[31] E. A. De Zubay. *Aero Digest*, **61**:54–56, 1950. 7, 8

[32] J.F. Driscoll and C.C. Rasmussen. *J. Prop. Power*, **21**[6]:1035–1044, 2005. 5, 12, 14

[33] D. Dunn-Rankin. *Lean combustion: technology and control*. Academic Press, 1st edition, 2008. 2, 3, 6, 7, 35

[34] D. Feikema, R.-H. Chen, and J.F. Driscoll. *Combust. Flame*, **86**:347–358, 1991. 12, 14, 102

[35] T.F. Fric. *J. Propul. Power*, **9**[5]:708–713, 1993. 107

[36] Davis S. G. and Law C. K. *Combust. Sci. Technol.*, **140**:427–449, 1998. 133

[37] A. Garmory and E. Mastorakos. *Proc. Combust. Inst.*, **33**:1673–1680, 2011. 15, 104, 168

[38] I. Glassman and R.A. Yetter. *Combustion*. Academic Press; 4th edition, 2008. 4

[39] G.A.E. Godsave. *Symp. (Intern.) Combust.*, **4**[1]:818–830, 1953. 16

[40] A. Grudno and K. Seshadri. *Combust. Sci. Technol.*, **112**:199–210, 1996. 12

[41] A.K. Gupta and J.M. Beer. *Appl. Acoust.*, **11**:35–55, 1978. 4, 5, 14

[42] E. P. Hassel and S. Linow. *Measur. Sci. Tech.*, **11**:37–57, 2000. 43

[43] T.J. Held, A.J. Marchese, and F.L. Dryer. *Combust Sci. Technol.*, **123**[1-6]:107–146, 1997. 135

[44] J. Hult, U. Meier, W. Meier, A. Harvey, and C.F. Kaminski. *Proc. Combust. Inst.*, **30**:701 – 709, 2005. 14, 43

[45] H.G. Im, J.H. Chen, and J.-Y. Chen. *Combust. Flame*, **118**[1-2]:204–212, 1999. 12

[46] X. Jiang, K.H. Luo, L.P.H. de Goey, R.J.M. Bastiaans, and J.A. van Oijen. *Flow, Turbul. and Combust.*, **86**[1]:63–88, 2011. 12

[47] W.P. Jones, S. Lyra, and S. Navarro-Martinez. *Proc. Combust. Inst*, **33**:2153–2160, 2011. 18

[48] W.P. Jones and V.N. Prasad. *Combust. Flame*, **157**:1621–1636, 2010. 15, 104, 168

[49] W.P. Jones and J. Wilhelmi. *Combust. Sci. Technol.*, **63**[1-3]:13–31, 1989. 61, 63, 72

[50] M. Juddoo and A. R. Masri. *Combust. Flame*, **158**:902–914, 2011. 14, 44, 103, 134

[51] A.M. Kanury. *Introduction to combustion phenomena.* Gordon and Breach Science, 1st edition, 1975. 7

[52] J. Kariuki, Letty C. Cavaliere, D.E., and E. Mastorakos. *AIAA paper*, **0505**, 2012. xix, 102, 127, 134, 156

[53] J. Kariuki, J. R. Dawson, and E. Mastorakos. *Combust. Flame*, **159**:2589–2607, 2012. 8, 41, 102, 106, 127

[54] V.R. Katta, T.R. Meyer, M.S. Brown, J.R. Gord, and W.M. Roquemore. *Combust. Flame*, **137**[1-2]:198–221, 2004. 12

[55] C.R. King. *NACA RM E57F26,*, 1957. 8

[56] D.A. Knaus, P.J. Magari, R.W. Hill, S.D. Phillips, and B.V. Kiel. *AIAA paper*, 2007. 26

[57] E. Korusoy and JH Whitelaw. *Combust. Sci. Technol.*, **176**[8]:1217–1241, 2004. 6

[58] K. M. Kundu, D. Bhaduri, and D. Banerjee. *ASME*, **102**:209–214, 1980. 7

[59] D.C. Kyritsis, V.S. Santoro, and A. Gomez. *Proc. Combust. Inst.*, **29**[2]:1679–1685, 2002. 12

[60] A. H. Lefebvre. *Atomization and Sprays*. Taylor and Francis, 1989. xii, 16, 17, 23, 24, 30, 35, 133, 140

[61] A. H. Lefebvre. *Gas Turbine Combustion*. Taylor and Francis, 1998. 21, 37, 47, 108, 109, 124

[62] P.A. Leonard and A.M. Mellor. *Combust. Flame*, **42**:93–100, 1981. 18

[63] C. Letty, E. Mastorakos, A.R. Masri, M. Judoo, and W. OLoughlin. *Exp. Therm. and Fluid Sci.*, **43**:47–54, 2012. 34, 40

[64] J. P. Longwell, E. E. Frost, and M. A. Weiss. *J. Ind. Eng. Chem.*, **45**:1629–1633, 1953. 7

[65] O. Lucca-Negro and T. O'doherty. *Prog. Energy Combust. Sci.*, **27**[4]:431–481, 2001. 4

[66] V.J. Lyons. *AIAA paper*, **20**:660–665, 1982. 107

[67] M.S. Mansour. *Combust. Flame*, **133**[3]:263–274, 2003. 6

[68] T. Marchione, S. F. Ahmed, and E. Mastorakos. *Combust. Flame*, **156**:166–180, 2009. 33, 36, 99, 125, 132

[69] S. Marinov, M. Kern, P. Zarzalis, N.and Habisreuther, A. Peschiulli, F. Turrini, and O. Sara. *Flow, Turbul. and Combust.*, **89**:73–95, 2012. 18

[70] A. R. Masri and J. D. Gounder. *Combust. Sci. Technol.*, **182**:702–715, 2010. 18, 124, 128

[71] A.R. Masri, B.B. Dally, R.S. Barlow, and C.D. Carter. *Proc. Combust. Inst.*, **25**:1301–1308, 1994. 13

[72] A.R. Masri, R.W. Dibbl, and R.S. Barlow. The structure of turbulent nonpremixed flames revealed by raman-rayleigh-lif measurements. *Prog. Energ. Combust.*, **22**[4]:307–362, 1996. 13, 14

[73] A. Massias, D. Diamantis, E. Mastorakos, and D. Goussis. *Combust. Theory Model.*, **3**:233–257, 1999. 106

[74] E. Mastorakos, A.M.K.P. Taylor, and J.H. Whitelaw. *Combust. Flame*, **91**[1]:55–64, 1992. 12, 14, 134

[75] A. M. Mellor. *Prog. Energy Combust. Sci.*, **6**:347–358, 1980. 106, 107, 124, 134, 139

[76] A.M. Mellor. *Prog. Energy Combust. Sci.*, **1**[2]:111–133, 1976. 22

[77] T.M. Muruganandam and J. Seitzman. *AIAA Paper*, **4331**, 2005. 7

[78] S. Nair and Lieuwen T. *J. Prop. Power*, **21**:32–39, 2005. 8

[79] S. Nair and Lieuwen T. *J. Prop. Power*, **23**:421–427, 2007. 8

[80] A. Neophytou and E. Mastorakos. *Combust. and Flame*, **156**:1627–1640, 2009. 139

[81] C.S. Panoutsos, Y. Hardalupas, and A.M.K.P. Taylor. *Combust. Flame*, **156**[2]:273–291, 2009. 40

[82] N. Peters. *Turbulent Combustion*. Cambridge University Press, 2000. 135

[83] N. Peters and F.A. Williams. *AIAA paper*, **21**:423–429, 1983. 14, 134, 135

[84] H. Pitsch. *Annu. Rev. Fluid Mech.*, **38**:453–482, 2006. 11

[85] H. Pitsch and S. Fedotov. *Combust. Theor. Model.*, **5**[1]:41–57, 2001. 12

[86] S.L. Plee and A.M. Mellor. *Combust. Flame*, **35**:2153–2160, 1979. xii, xix, 18, 22, 24, 25, 26, 31, 32, 132, 133, 154

[87] T. Poinsot and Veynante D. *Theoretical and numerical combustion*. Edwards, 1st edition, 2001. 10

[88] W. Pun, S.L. Palm, and F.E.C. Culick. *AIAA conference*, 2000. 40

[89] K. Radhakrishnan, J.B. Heywood, and R.J. Tabaczynski. *Combust. Flame*, **42**:19–33, 1981. xvii, xix, xx, 7, 9, 10, 99, 106, 107, 120, 133, 134, 135, 139, 155, 156, 163, 164, 166, 167

[90] M.J. Russi, I. Cornet, and R. Cornog. *Flow, Turbul. and Combust.*, **4**:743 – 748, 1953. 7

[91] K. Sardi, A. Taylor, and JH Whitelaw. *Combust. Flame*, **120**[3]:265–284, 2000. 12

[92] K. Sardi and JH Whitelaw. *Exp. fluids*, **27**[3]:199–209, 1999. 12

[93] R.W. Schefer, M. Namazian, and J. Kelly. *Combust. Sci. Technol.*, **56**[4-6]:101–138, 1987. 61

[94] P. Schmittel, B. Günther, B. Lenze, W. Leuckel, and H. Bockhorn. *Proc. Combust. Inst.*, **28**[1]:303–309, 2000. 109

[95] R. Seiser, H. Pitsch, K. Seshadri, W.J. Pitz, and H.J. Gurran. *Proc. Combust. Inst.*, **28**:2029 – 2037, 2000. 36

[96] S. J. Shanbhogue, S. Husain, and T. Lieuwen. *Prog. Energy Combust. Sci.*, **35**:98–120, 2009. 7, 22, 107, 134, 139

[97] I. Silverman, JB Greenberg, and Y. Tambour. *Combust. Flame*, **93**[1]:97–118, 1993. xii, 17, 30

[98] S.N. Soid and Z.A. Zainal. *Energy*, **36**[2]:724–741, 2011. 16

[99] D.B. Spalding. *Aircr. Eng. Aerosp.Tec.*, **25**:264 – 276, 1953. 7

[100] P. Sripakagorn, S. Mitarai, G. Kosly, and H. Pitsch. *J. Fluid Mech.*, **518**:231–259, 2004. 12, 14

[101] A.M. Steinberg, I. Boxx, C.M. Arndt, J.H. Frank, and W. Meier. *Proc. Combust. Inst.*, **33**:1663–1672, 2011. 14, 103, 134

[102] J.A. Sutton and J.F. Driscoll. *Proc. Combust. Inst.*, **31**:1487 – 1495, 2007. 14, 135

[103] N. Syred. *Progr. Energ. Combust.*, **32**[2]:93–161, 2006. xii, 4, 29

[104] S. R. Turns. *An Introduction to Combustion: Concepts and Applications*. McGraw-Hill, New York, 2nd edition, 2000. 3, 36, 47, 107, 108

[105] J.H. Tuttle, M.B. Colket, R.W. Bilger, and A.M. Mellor. *Symp. (Intern.) Combust.*, **16**[1]:209–219, 1977. 22

[106] A. Tyliszczak and E. Mastorakos. *Flow, Turbul. Combust., Submitted*, pages 1–31, 2013. 135

[107] K.P. Vanoverberghe, E.V. Van Den Bulck, and M.J. Tummers. *Combust. Sci. Technol.*, **175**[3]:545–578, 2003. 9

[108] X.F. Wang and A.H. Lefebvre. *J. Propul. Power*, **3**[1]:11–18, 1987. 16

[109] F. A. Williams. *Flame Stabilization of Premixed Turbulent Gases*. Spartan Books, 1966. 7

[110] F.A. Williams. *Combustion Theory*. Westview Press, 1994. 7, 17

[111] G.C. Williams, H.C. Hottel, and A.C. Scurlock. *Symp. Combust. Flame,and Expl. Phen.*, **3**:21 – 40, 1949. 7

[112] N.A. Worth and J. R. Dawson. *Combust. Flame*, **159**:1109 – 1126, 2012. 41

[113] F. Xie, Y. Huang, B. Hu, and F. Wang. *IEEE*, **2**:2049–2053, 2011. 18

[114] S. Yamaguchi, N. Ohiwa, and T. Hasegawa. *Combust. Flame*, **62**:31 – 41, 1985. 7

[115] E.E Zukoski and F.E. Marble. *Proc. Gas Dynamics Sym. on Aerothermo-chemistry*, pages 205 – 210, 1955. 7

[116] E.E. Zukoski and F.E. Marble. *AGARD Combust. Researches and Reviews*, pages 167–180, 1955. 23